Dynamic Nuclear Polarisation Surface Enhanced NMR Spectroscopy

Alexandre Zagdoun

Dynamic Nuclear Polarization Surface Enhanced NMR Spectroscopy

Alexandre Zagdoun
Centre de RMN à très hauts champs,
École Normale Supérieure de Lyon,
École Doctorale de Chimie de l'Université de Lyon

Thèse soumise en vue de l'obtention du grade de
Docteur en chimie de l'Université de Lyon, délivré par l'École Normale Supérieure de Lyon
soutenue publiquement le 12 Juin 2014

Travaux dirigés par le Pr. Lyndon Emsley

Devant la commission d'examen formée des:

Pr. Lyndon Emsley

Dr. Anne Lesage

Pr. Daniella Goldfarb

Pr. Christian Bonhomme

Pr. Malcolm Levitt

"Because we are living in a material world, and I am a material girl."
Madonna

Remerciments

Comme à l'accoutumée, cette thèse s'ouvre sur les remerciements. Cette partie (peut être la plus intéressante du manuscrit) est l'occasion pour moi de remercier toutes les personnes qui comptent pour moi et qui m'ont supporté pendant ces trois années (ce qui demande parfois beaucoup de patience).

Bien sûr je tiens à remercier tout d'abord les Pr. Daniella Goldfarb et Christian Bonhomme d'avoir accepté d'évaluer ce travail, ainsi que le Pr. Malcolm Levitt pour avoir accepté de participer à la soutenance.

Je tiens aussi à remercier le Pr. Lyndon Emsley et le Dr. Anne Lesage tout d'abord pour avoir accepté que je travaille sur ce sujet dans leur laboratoire, et surtout pour leur encadrement tout au long de ces trois années. Merci de m'avoir confié des projets excitants et passionnants, et d'avoir sû me faire confiance. Les idées évoquées dans ce manuscrit sont le fruit d'une équipe et non d'un travail solitaire, et Anne et Lyndon ont su mener la barque avec brio. Je tiens à remercier le Pr. Lyndon Emsley pour avoir toujours su trouver du temps pour écouter mes idées ou commentaires sur le travail; et pour la liberté qu'il m'a laissé pour les enseignements de RMN, qui m'ont beaucoup apporté. Anne, merci pour ta constante bonne humeur, et ton infinie patience! Le travail présenté dans ce manuscrit ne serait rien sans le Dr. Aaron Rossini dont les idées et le travail ont profondément impacté chacun des projets. C'est aussi lui qui m'a appris à manipuler, merci donc de m'avoir appris tous les trucs et astuces pour ne pas devenir fou en essayent de piloter un spectro réticent. Le Dr. Moreno Lelli, ainsi que le Dr. David Gajan ont aussi grandement contribué aux projets développés cette année et je tiens à les remercier pour leurs précieux apports. Enfin nous ne pourrions pas manipuler sans Lénnaïc Lerroux, et le soin constant qu'il apporte à l'entretien et au bon fonctionnement du spectro.

Ce travail n'aurait pas pu voir le jour sans deux précieuses collaborations, l'une avec le laboratoire du Pr. Christophe Copéret à l'ETH Zürich, où ont

été synthétisé les matériaux étudiés dans cette thèse; l'autre avec l'équipe du Pr. Paul Tordo à Marseille qui s'est chargé de la synthèse des biradicaux utilisés durant ces 3 ans. Cette collaboration dynamique entre trois équipes aux compétences différentes mais complémentaires a permis le développement rapide de la méthode. Merci donc au Pr. Christophe Copéret, aux Drs. Matthew Conley, Arthur Roussay Matthieu Baffert, Laurent Veyre, Chloé Thieuleux ainsi qu'à Martin Schwarzwälder, Wolfram Grüning, Guiseppe Lappadula et Adrien Bourdolle pour le design et la synthèse des matériaux que nous avons utilisé. Merci d'avoir su nous écouter et parfois céder à nos caprices en synthétisant des matériaux qui n'auront pas d'autres applications que de démontrer un point sur la DNP. L'équipe Marseillaise constituée du Pr. Paul Tordo, des Drs. Olivier Ouari, Gilles Casano, et de Claire Sauvée a été d'une aide précieuse dans le design des nouveaux radicaux présentés ic. Elle a aussi réalisé des tours de force en synthèse organique pour produire ces molécules, loin d'être simples. Merci aussi à l'équipe du Pr. Gunnar Jeschke pour la réalisation des mesures RPE. Le CRMN n'est équipé que depuis peu de spectromètres DNP, et la quasi-totalité des expériences décrites dans ce manuscrit ont été réalisées dans des laboratoires d'accueil. Merci donc à l'équipe du professeur Bodenhausen à Lausanne, l'équipe du Pr Oschkinat à Berlin, ainsi qu'à Mélanie Rosay et Marc Caporini de Bruker USA,; et à Fabien Aussenac de Bruker France.

Évidemment je tiens à remercier ma famille pour toujours avoir été là pour moi. Merci à mes parents, mes frères et ma tante. Je sais que je n'ai pas souvent été très expansif sur mon sujet de thèse j'espère que la soutenance vous éclairera un peu sur ce qu'a été mon quotidien pendant trois ans. Merci aussi de m'avoir toujours soutenu quelque soit mes projets et de m'avoir donné une telle liberté!

Au cours de ces six ans passés à Lyon il m'a été donné de rencontrer et me lier d'amitié avec des gens extraordinaires. Il est donc normal qu'une grande partie de ces remerciements soient dédiés à mes amis pour tous ces moments passés ensemble, en vacances, en soirée, à bruncher devant qvemf ou pour manifester. Cette partie est donc pour, dans le désordre: Germain, Richard, Sara, Yann, Lucy, Etienne, Guillaume, Eric, Marc, Baptiste, Guilhem, Léa, Pif, Chloé, Blaise, Florent, Pierre, Pierre, Audrey, Noémie, Catherine, Fosca, Charlotte. Sans vous mon quotidien lyonnais aurait été bien morose... Une mention spéciale va au gens de la Branche Bâtarde: le théâtre a été pour moi extrêmement important durant ces 6 ans. Merci en particulier à Nadine Douriaud: Nadine, travailler avec toi a été une expérience géniale! Ces remerciements ne seraient pas complets sans une mention

spéciale pour les soeurs Odieuses de Beauregard: Chasteté, Modestie, Marie-Mo, qui ont toujours su me divertir en gardant cette classe qui leur est propre.

Enfin un petit mot pour trois personnes qui ont été spéciales pour moi pendant cette thèse, et ont chacun su me supporter et me soutenir à leur manière: Yann, Paul et Romain.

Maintenant se finit la partie joyeuse, légère (et un peu nostalgique) de ce manuscrit, et il est temps de rentrer dans le vif du sujet. J'espère que la lecture de cette thèse vous plaira, ou tout du moins que vous y trouverez un élément de réponse aux questions qui vous ont amené à l'ouvrir.

Abstract

Since its discovery in the 1950's, DNP has been a topic of significant interest in magnetic resonance. DNP is the transfer of polarization between single electrons and nuclei, driven by micro-wave irradiation. Since its *renaissance* at high field in the 90's, due to the introduction of gyrotrons as high-power, high-frequency microwave sources most application of this technique have been samples of biological interest in frozen solution. The long standing interest of our group in the characterization of surface species such as supported catalysts on silica lead us to apply this technique to the study of surfaces. The goal of this thesis is the development of this method, dubbed DNP Surface Enhanced NMR Spectroscopy. To that end, we first introduce new polarizing agents, soluble in organic solvents. The influence of the electron relaxation times on the DNP enhancements is demonstrated and efficient tailored polarizing agents are introduced. The optimization of the sample preparation to obtain optimal sensitivity is also discussed, as well as the interaction between the radical and the surface. These developments made it possible to apply the technique to many functionalized materials, with some examples developed in this manuscript. Finally, the issue of DNP on polarization conductors is discussed, and we show how microcrystals can be efficiently polarized using DNP.

Keywords: Dynamic Nuclear Polarization, solid-state NMR spectroscopy, EPR, magnetic resonance, spin diffusion.

Depuis sa découverte dans les années 50, la DNP suscite un intérêt croissant en résonance magnétique. La DNP peut être définie comme le transfert d'aimantation entre des électrons célibataires et les noyaux de l'échantillon induit par irradiation micro-onde. Depuis sa renaissance à hauts champs dans les années 90, grâce à l'introduction des gyrotrons comme source micro-onde haute fréquence haute puissance, la plupart des développements et applications de la méthode concernent des échantillons d'intérêt biologique en solution solide. L'intérêt de notre groupe pour la caractérisation d'espèces de surface, tels que les catalyseurs supportés sur silice nous a conduit à appliquer la DNP à des espèces de surface. Le but de cette thèse est le développement de cette méthode nommée DNP SENS. Pour cela de nouveaux agents de polarisations sont tout d'abord introduits, avec une discussion sur l'influence des temps de relaxation électroniques sur l'efficacité DNP. L'optimisation de la préparation des échantillons pour maximiser la sensibilité RMN est discutée, ainsi que l'interaction entre les radicaux et la surface. Ces développements ont permis la caractérisation de nombreux matériaux et quelques exemples sont donnés ici. Enfin, une dernière partie se concentre sur l'application de la DNP à des conducteurs de polarisation, et montre la possibilité d'hyperpolarisés des objets de taille micrométrique.

Mots clefs: Polarisation Nucléaire Dynamique, spectroscopie RMN de l'état solide, RPE, résonance magnétique, diffusion de spin.

Résumé de la thèse

La Polarisation Nucléaire Dynamique

La Polarisation Nucléaire Dynamique (Dynamic Nuclear Polarization, DNP) est une méthode d'hyperpolarisation d'échantillon qui repose sur un transfert d'aimantation entre des électrons célibataires et des noyaux. Les électrons étant naturellement 660 plus polarisés que les protons, un transfert d'aimantation peut théoriquement conduire à une augmentation du signal de plusieurs ordres de grandeur. Cet effet fut prédit par Albert Overhauser en 1953 et vérifié expérimentalement sur des échantillons de lithium métallique par Slichter et Carver la même année. Dans ce cas, l'aimantation est transférée des électrons de conduction du métal vers les noyaux et le mécanisme de transfert repose sur l'effet Overhauser. Dans les années qui suivirent cette découverte, le même effet fut observé sur d'autres métaux ainsi que pour des électrons en solution dans l'ammoniac.

Cependant, l'effet Overhauser présente peu d'application pour la polarisation de système intrinsèquement dépourvu d'électron célibataire/de conduction. En 1958 le Solid Effect fut découvert, puis le Cross-Effect en 1963, ouvrant la voie à la polarisation des noyaux par des électrons célibataires exogènes. Au même moment, le développement rapide de la technologie des supraconducteurs a conduit à l'utilisation de hauts champs en RMN (> 5 T), conduisant à de grands gains en sensibilité et en résolution. Le manque de source micro-onde à haute puissance et haute fréquence, capable de saturer les résonances électroniques à haut champ a rendu la DNP incompatible avec leur utilisation.

L'introduction dans les années 90 par l'équipe de Robert Griffin au MIT des gyrotrons comme sources micro-ondes pour la DNP a marqué la renaissance de cette technique. Depuis elle a connu de fulgurants développements, avec notamment de nombreuses applications à des échantillons d'intérêt biologique. Le but de cette thèse est de montrer le travail réalisé pendant trois

ans au CRMN Lyon sur l'application de la DNP à l'étude de surfaces de matériaux.

Développement d'agents de polarisation pour CE DNP

Le gain (ε) obtenu lors d'une expérience DNP dépend grandement du type d'agent polarisant utilisé. Le développement de radicaux pour la DNP est un domaine de recherche récent mais en pleine expansion. Le CE est un mécanisme qui nécessite deux spins électroniques dont les fréquences de résonances sont séparées par de la fréquence de Larmor du noyau à polariser. Il est dur de trouver deux radicaux isotropes remplissant cette condition. Les radicaux utilisés pour la CE DNP sont en général basés sur des nitroxides, dont l'anisotropie est adaptée à la polarisation des protons. Il a été montré que les agents de polarisation les plus efficaces sont des bi-radicaux dont les deux nitroxides sont orthogonaux. Un critère qui n'a pas été utilisé jusqu'à présent dans le design rationnel de radicaux pour la DNP sont les temps de relaxation électronique. En effet la première étape du mécanisme étant la saturation d'un des deux électrons, on peut s'attendre à ce que plus les temps de relaxation électroniques sont courts, moins cette première étape sera facile. Une série de dérivés du radical bTbK (présentant une conformation optimale pour la DNP) avec différents temps de relaxations électroniques ont été développés et synthétisés. Un lien est établi entre ε et le facteur de saturation s. L'impact du nombre du groupement méthyle en α du nitroxide est aussi souligné, ainsi que leur rôle dans la dépendance en température d'ε.

Optimisation de la sensibilité lors d'expériences DNP SENS

L'étude de matériaux fonctionnalisé, souvent sensibles à l'air et l'eau et/où hydrophobe empêche l'utilisation des radicaux hydrosolubles développés pour les bioapplications de la DNP. Une première partie de ce chapitre est dédié à la recherche de solvants organiques compatibles avec les expériences DNP.

L'introduction d'agents paramagnétiques dans l'échantillon impacte ses propriétés RMN, et en général nuit à la sensibilité des expériences RMN, l'intensité du signal diminuant avec la concentration en agents de polarisation. La dépendance de ε avec la concentration en radical quant à elle est une

courbe en cloche avec un maximum habituellement situé vers les 16 mM. Il n'est donc pas évident que la concentration en radical donnant une sensibilité maximale corresponde à celle donnant la meilleure sensibilité.

La nature même de l'échantillon affecte sa compatibilité avec les expériences DNP. En particulier, la présence de nombreux groupements possédants des temps de relaxation longitudinaux courts (comme c'est le cas pour les échantillons passivés par des groupements -OTMS) réduit grandement l'efficacité DNP. La deutération de ces groupements permet de restaurer de hautes valeurs d'ε. De plus, la nature du groupement passivant change les interactions des radicaux avec la surface.

L'interaction avec la surface peut aussi être modifiée si les radicaux deviennent trop volumineux, comme c'est le cas pour certains développés au cours de ce travail.

Exemples d'applications de la méthode DNP SENS

La DNP SENS a permis de caractériser de nombreux matériaux au cours de ces 3 ans et ce chapitre donne quelques exemple d'applications de la méthode.

Par exemple, des Metal-Organic Frameworks (MOF) peuvent être caractérisés au niveau moléculaire par DNP SENS. Il est en particulier possible de caractériser des MOFS partiellement fonctionnalisées par de la proline, ce qui les rend incompatible avec des méthodes de diffraction par rayons X. L'optimisation des conditions expérimentales est développée ainsi que l'influence de la taille des pores sur l'efficacité DNP.

L'intérêt de notre groupe pour les catalyseurs supportés sur silice a poussé l'application de la DNP SENS à l'étude de ce genre de matériaux. Il est par exemple possible, en utilisant la RMN 1 et 2 D ^{1}H, ^{13}C, ^{29}Si et ^{15}N (en abondance isotopique naturelle), de suivre les réactions de surface utilisée pour synthétiser le ligand du catalyseur. La caractérisation moléculaire complète d'un catalyseur au palladium a notamment aussi été réalisée.

L'étape suivante dans la caractérisation de ces matériaux est la détermination de la conformation vis à vis de la surface. Pour cela, des expériences REDOR ^{15}N- ^{13}C ainsi que des expériences LGCP ^{1}H-^{13}C et ^{1}H-^{29}Si. ont été réalisées, permettant d'extraire des distances inter-atomique, donnant ainsi accès à la conformation.

Applications de la DNP à des conducteurs de polarisation

Dans les exemples des chapitres précédents, le coeur des matériaux était dépourvu de protons. Cependant, si des protons sont présents dans le coeur du matériau (comme c'est le cas pour les cristaux organiques par exemple), l'hyperpolarisation de la surface va diffuser vers le centre du matériaux, permettant ainsi d'hyperpolariser des distances de l'ordre du micro-mètre.

Un modèle numérique pour simuler de tels systèmes a été développé. En particulier l'influence des différents temps de relaxation et de la taille des particules est explicité. Ces prédictions sont vérifiées par des expériences sur des micro cristaux de glucose, paracétamol et sulfathiazole. Les gains de sensibilité permettent d'acquérir des expériences de corrélation ^{13}C-^{13}C en abondance naturelle en quelques dizaine d'heure, ce qui est remarquable, en particulier pour des cristaux ayant des T_1 de l'ordre de la centaine de secondes.

Cette technique peut être utilisée pour sonder la composition de composés pharmaceutiques, en particulier la taille des domaines de l'ingrédient principal actif, ou encore les interactions entre excipient en API.

La constante de diffusion de spin est importante dans ces modèles, et détermine entre autre la distance de pénétration de l'hyperpolarisation dans le cristal et la vitesse de propagation de l'hyperpolarisation. Si il existe des expériences pour mesurer cette constante, il n'est pas évident de faire le lien avec la structure cristalline du composé. Un modèle pour déterminer la constante de diffusion de spin a partir de la géométrie d'un cristal et de calculs LCL a été développé ici, avec des résultats encourageants ne nécessitant que 125 spins dans la simulation.

List of Figures

Contents

Chapter 1

Introduction

The ability to determine three-dimensional molecular structures from single crystals by diffraction methods has transformed molecular and materials science over the past 100 years, leading to the structure-based understanding of chemistry we have today. However, when the species of interest is at a surface, the problem of structure elucidation becomes much more challenging. The rational development of new materials for applications as diverse as conversion/capture of atmospheric CO_2, solar energy, gas storage/separation, hydrogen production, or advanced sensors requires structure-property relationships to be established.[1] Today, EXAFS, vibrational (IR and Raman), and electronic (UV-Visible) spectroscopies, together with surface science techniques (XPS, Auger, atomic force and electron microscopy) and mass spectrometry (SIMS) are used to characterize surfaces. However, methods for complete atomic level characterization have remained elusive unless high-vacuum techniques and well-defined crystalline phases are considered.

Solid-state nuclear magnetic resonance (NMR) would be the technique of choice for atomic characterization of surface species if it were not for its intrinsically low sensitivity (compared to higher energy spectroscopies); which is further exacerbated for surface characterization by the small fraction of surface sites. For example, typical high surface area (A=800 $m^2.g^{-1}$) mesoporous silicas have a concentration of only 0.011 $mmol.g^{-1}$ (0.002 $mmol.mL^{-1}$) of surface functionalities, 1 or 2 orders of magnitude less than in a bulk molecular organic solid. The problem becomes worse as the surface area of the material or the density of surface sites is reduced (Figure 1.1).

Despite the challenge of low sensitivity, there is great interest in developing NMR for the characterization of surfaces. Following the development of modern cross-polarization magic angle spinning solid-state NMR experiments

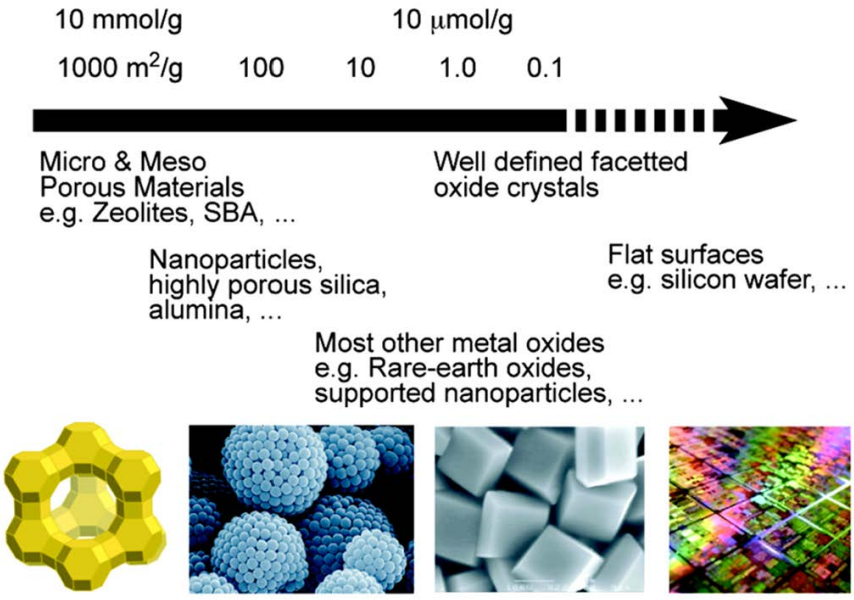

Figure 1.1: Some functional materials and their typical surface areas (taken from ref [2].

(CP MAS), it was soon realized that solid-state NMR could be a powerful probe selectively of surface structure. In the early 1980s, Maciel and coworkers demonstrated that cross-polarization (CP) could be used to selectively observe NMR signals associated with the surface of silica, by transferring polarization from nuclei residing only at the surface of the material.[3, 4] CP MAS experiments were used for the acquisition of ^{13}C and ^{31}P spectra of molecules immobilized on polymer and silica surfaces.[4, 5]These experiments allow for the determination of the distribution of atomic environments, or to follow chemical transformations, probe dynamics, and propose structural models.

The characterization of single-site heterogeneous catalysts with solid-state NMR is a large focus of our research groups.[6, 7, 8, 9, 10, 11] For highly receptive NMR nuclei (for instance ^{1}H, ^{19}F, and ^{31}P), the chemical structure, connectivity, and spatial proximity of surface species can be probed with multidimensional correlation experiments.[11, 12] Pulse sequences which directly detect signals from dilute nuclei with nuclear spin I = 1/2 (like ^{13}C, ^{15}N, ^{29}Si) or quadrupolar nuclei (I > 1/2) are well established.[12, 13] However, they

are difficult to apply to surfaces since days of signal averaging are typically required for basic 1D spectra, unless the sample is isotopically labelled or fast MAS rates ($\nu_{rot} > 30$ kHz) and indirect detection are applied.[14] Indirect detection provides sensitivity enhancements of up to an order of magnitude; however, this is still insufficient to enable rapid characterization of many surface species.

Over the years, many methods have been developed to enhance the sensitivity of NMR, whether by transferring polarization from an abundant higher γ nucleus (e.g. CP or insensitive nuclei enhanced by polarization transfer (INEPT)), or by introducing exogenous polarizing agents (para-hydrogen) or unpaired electrons for dynamic nuclear polarization (DNP)). Recently, the latter has attracted much interest, and is the basis of the research presented in this thesis.

DNP takes advantage of the naturally high polarization of single electrons - 660 times more polarized than protons. Their polarization can be transferred upon microwave (MW) irradiation to surrounding nuclei via the electron-nucleus dipolar coupling. Unfortunately, the lack of high-power high-frequency MW sources prevented DNP from being applied at high magnetic field. It was not until the introduction of gyrotrons as MW sources in the 90's that DNP became compatible with high-field NMR. Since then, many efforts have been devoted to the development of this technique, and particularly to its application to systems of biological interest.

This manuscript presents the work realized at the Centre de résonance mangnétique à très haut champ (CRMN) between January 2011 and January 2014. The work presented here started just after the first demonstration by Anne Lesage and coworkers that high-field DNP could be applied to the study of material surfaces. In order to set the stage a short history of DNP and a description of the main mechanisms responsible for the polarization transfer are given in the next chapter. Chapter 3 will focus on the development of polarizing agents for cross-effect (CE) DNP, and particularly on the importance of electron relaxation times on the DNP enhancement.

Chapter 4 is about the optimization of the sample preparation in order to maximize the sensitivity, rather than the enhancement. The effect of high radical concentration in the material will be discussed, as well as the presence of abundant fast relaxing protons. The interaction between the radicals and different types of surfaces is also treated.

Using theses results, Chapter 5 shows some applications of DNP to the study of materials; and in particular to metal organic frameworks and to functionalized mesostructured silica.

Finally Chapter 6 deals with polarization conductors, i.e materials containing protons in their core. We will see how micro sized object can be efficiently polarized using DNP, and a theoretical model is developed to explain these results. Prediction of spin diffusion coefficients from *ab initio* simulations will also be discussed in this chapter.

The work was done over a 3 year period, but the results were not obtained in a "linear" fashion, which explains that some results in a chapter refer to work which will be explained in another chapter. Some parts are quite technical and maybe not fascinating to read, but were necessary steps to more exciting results and are therefore related here. I really hope that you will enjoy reading this thesis.

Chapter 2

Dynamic Nuclear Polarization

2.1 A very brief history of DNP.

DNP is not the kind of scientific breakthrough that found success and applications immediately after its discovery, for many reasons. To start, its theoretical prediction by Albert Overhauser in 1953, who predicted that a polarization transfer could occur between the conduction electron spins and the nuclei in a metal by irradiating the electron spins at their EPR frequency, left at that time the NMR community quite skeptical.[1]However, this phenomenon was shortly after demonstrated by Slichter and Carver on powdered Li samples, with an estimated enhancement of the ^{7}Li signal of $\sim$ 100 (see Figure 2.1).[15] Later that year, Overhauser finally published his theoretical work on dynamic nuclear polarization.[17] This technique was subsequently applied to other powdered metals (Rb, Na) and to protons (using free electrons in ammonia solution).[18] It was soon realized that this effect was not limited to polarization transfer between electrons and nuclei but that a nuclear equivalent to the Overhauser effect existed, as proven by experiments on HF by Solomon and coworkers.[19] The Nuclear Overhauser Effect (NOE) is now widely used in solution state NMR to measure distances between nuclei.

However, Overhauser Effect (OE) DNP requires that the motion of the electrons (translational and rotational diffusion for solutions, mobile electrons such as the electrons in the conduction band of a metal for solids) occurs on a timescale shorter than that of the NMR (which means that $\tau_c\omega_0 << 1$ with τ_c the correlation time of the electrons spins and ω_0 the Larmor frequency); which is the case at low magnetic fields for conduction electrons

[1]For a personal and vivid description of the history of DNP by Slichter see ref [16]

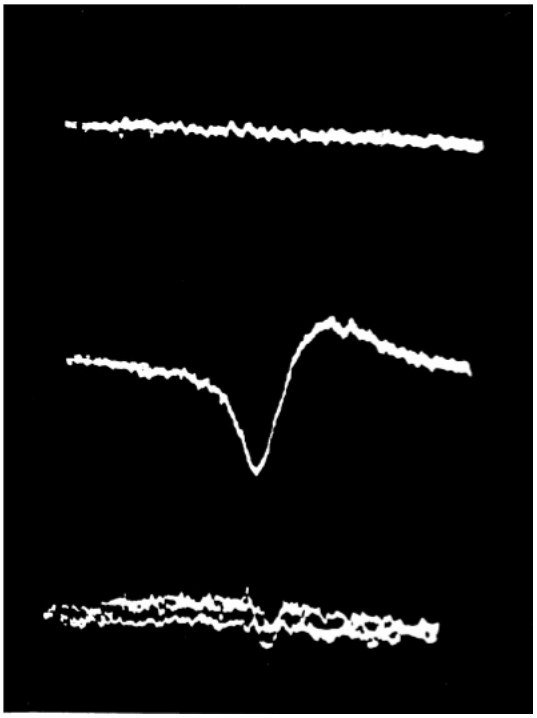

Figure 2.1: Very first demonstration of the Overhauser effect on a powdered lithium sample in a 50kHz static field. Top Line: ^{7}Li resonance (lost in noise), Middle line: ^{7}Li resonance enhanced by electron saturation. Bottom line: proton resonance of a glycerine sample 8 times larger than the Li sample, used to estimate the enhancement. Taken from reference [15], © the American Physical Society.

and solvated electrons, but *a priori* limits its application to a wider range of systems. In 1958, the solid effect (SE) was discovered,[20, 21] leading to DNP experiments at higher field using narrow-line radicals. Later on, the Cross-Effect (CE) mechanism was discovered with DNP experiments using radicals presenting inhomogeneously broadened EPR lines.[22, 23, 24, 25] Unfortunately, these effects suffer from unfavorable field dependance, the enhancement diminishing dramatically as the field increases. At the same time, technological breakthroughs in supraconducting materials made it possible for NMR to move to higher fields, yielding dramatic improvements in both resolution and sensitivity. Nowadays, static fields up to 1 GHz (23.4 T static field) are available, and the race to higher fields is far from being over with rumors of 1.2 GHz spectrometers being developed over the next few years. The lack of high-power, high-frequency MW generators able to saturate the

electron resonances at higher field forced DNP to remain a scientific curiosity with applications mainly in the production of polarized targets for particle physics.[26]

The *renaissance* of DNP at high field we are witnessing today is due to many factors: the rapid development of magic-angle spinning (MAS) technologies in the 80's, and of cryogenic technologies; the development of MW technology at high-frequency with the development of gyrotrons for DNP as high-power sources; progress made in the synthesis of stable radicals and the abnegation of the Griffin group at MIT, who kept pushing this field forward to the dynamic and rapidly changing area of research it is today. In the following, we will focus on high-field DNP in solids. Nevertheless, (high field) OE DNP is still an important and active area of research[27, 28, 29, 30] but is unfortunately out of the scope of this PhD work. In the following, we will focus on the SE and CE which are used in modern high-field DNP experiments. In order to obtain the highest enhancement (ε, defined as the ratio of signal intensities of spectra acquired with and without microwave irradiation) possible and design efficient sources of polarization (so called polarizing agents), it is necessary to understand the physics behind the DNP processes. The next section will be a short overview of important mechanisms involved in high-field solid-state DNP.

2.2 Mechanisms involved in high-field solid-state DNP.

2.2.1 The Solid Effect.

The SE is dominant for radicals presenting relatively narrow EPR lines compared to the nuclear Larmor frequency, i.e. the electron anisotropy (inhomogeneous spectral width) and homogeneous line width are smaller than to the nuclear Larmor frequency. The polarizing agent is often a radical with high molecular symmetry (small **g** anisotropy) like carbon-centered radicals like BDPA or trityl and their derivatives (see Figure 2.4). This effect can be modeled by a two-spin (one electron one nucleus) system. In this approach, the dipolar coupling between the spins can be seen as a perturbation of the Zeeman Hamiltonian, leading to a mixing of the Zeeman states, therefore allowing otherwise "forbidden" flip-flop transitions to occur and yielding enhanced proton polarization. The approximated Hamiltonian applicable to

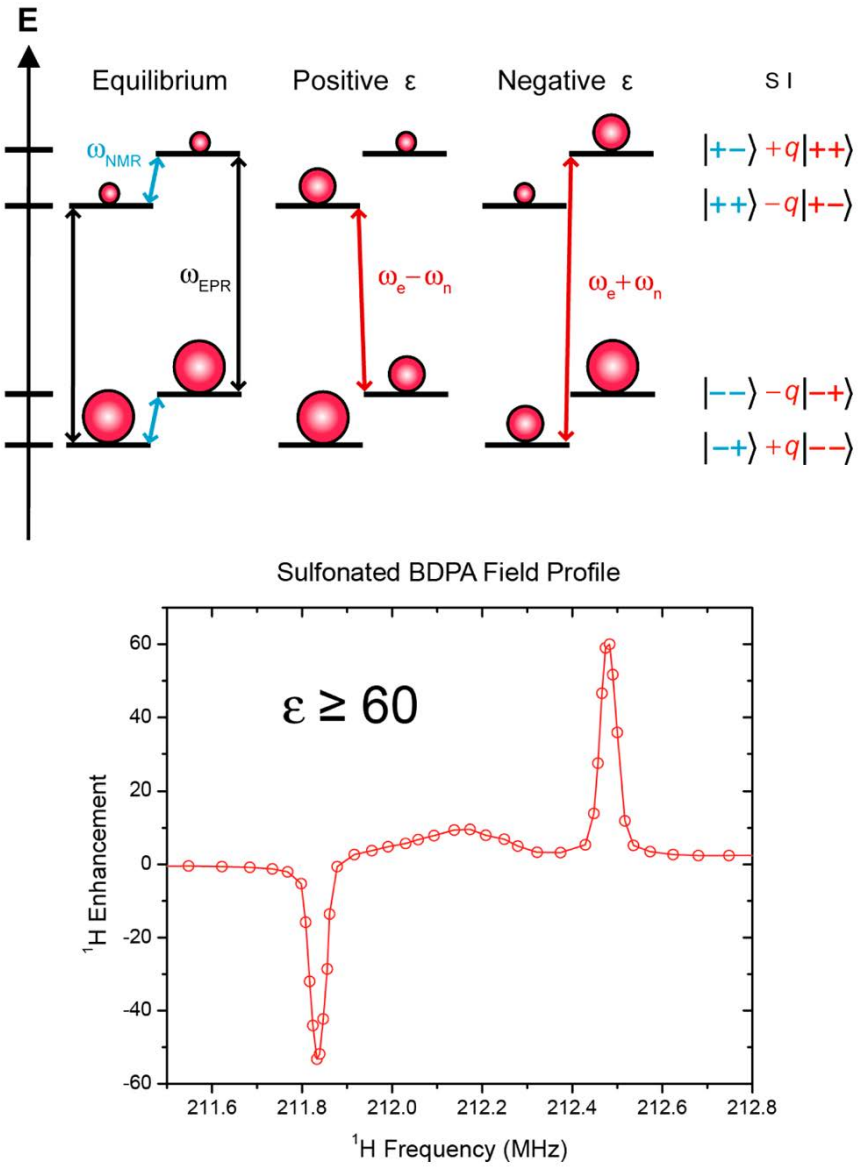

Figure 2.2: (A) Energy level diagram of a one electron spin one nuclear spin system. At thermal equilibrium (left), populations are governed by the Boltzmann distribution. Mixing of states in the electron spin subspaces (right) leads to partially allowed double quantum (DQ) and zero quantum (ZQ) transitions, yielding positive and negative enhancements respectively. (B) Plot of the enhancement from SA-BDPA as a function of magnetic field (^{1}H frequency) showing the positive and negative enhancements.Taken from reference [31] © the American Chemical Society.

the electron-nucleus system is:

$$H = \omega_{0e}S_z - \omega_{0n}I_z + CS_zI_+ + C^*S_zI_- \tag{2.1}$$

where I and S are the operators for the nuclear and electronic spin operators respectively, ω_{0n} is the nuclear Larmor frequency, ω_{0e} the electron Larmor frequency, and C the electron-nuclear dipolar term:

$$C = \frac{-3\gamma_S\gamma_I}{4r_{IS}^3} sin\theta cos\theta e^{-i\phi}$$

where r_{IS}, θ and ϕ are the polar coordinates of the electron-nuclear vector. Perturbation theory yields four new mixed eigenstates (see Figure 2.2). Microwave irradiation can now drive double quanta (irradiation at ω_{0e}-ω_{0n}) and zero quantum (irradiation at ω_{0e}+ω_{0n}) transitions, with an intensity proportional to q^2=|C/2$\omega_{0n}|^2$. Figure 2.2 (B) shows the field sweep profile (signal enhancement ε as a function of the ^{1}H Larmor frequency) obtained on a frozen solution of SA-BDPA. As expected, the zero-quantum transition (ω_{0e}-ω_{0n}) yields a negative enhancement while the double-quantum (ω_{0e}-ω_{0n}) yields a positive ε. Unfortunately, the mixing coefficient and therefore the enhancement are proportional to B_0^{-2}, making this effect less efficient as the field increases.

These radicals are often used for dissolution DNP where the polarization step is done at low field and very low temperature (1 to 4 K) before dissolving the hyper polarized mixture with hot solvent.[32] For a more complete and thorough description of the SE see in references [33, 34, 35, 36]. In the case of high field MAS DNP, another type of radical is often used, polarizing the nuclei through a different process.

2.2.2 The Cross Effect

Unlike the SE, this effect is based on *allowed* transitions and involves interaction of electron spin packets in an inhomogeneously broadened EPR line. It can modeled by a two electrons one nucleus system. The CE Hamiltonian is:

$$H = H_Z + H_{E-N} + H_{E-E} \tag{2.2}$$

with

$$H_Z = \omega_{0e1}S_{1z} + \omega_{0e2}S_{2z} - \omega_{0n}I_z \tag{2.3}$$

the Zeeman Hamiltonian

$$H_{E-N} = (A_1S_{1z} + A_2S_{2z})I_z + (B_1S_{1z} + B_2S_{2z})I_x \tag{2.4}$$

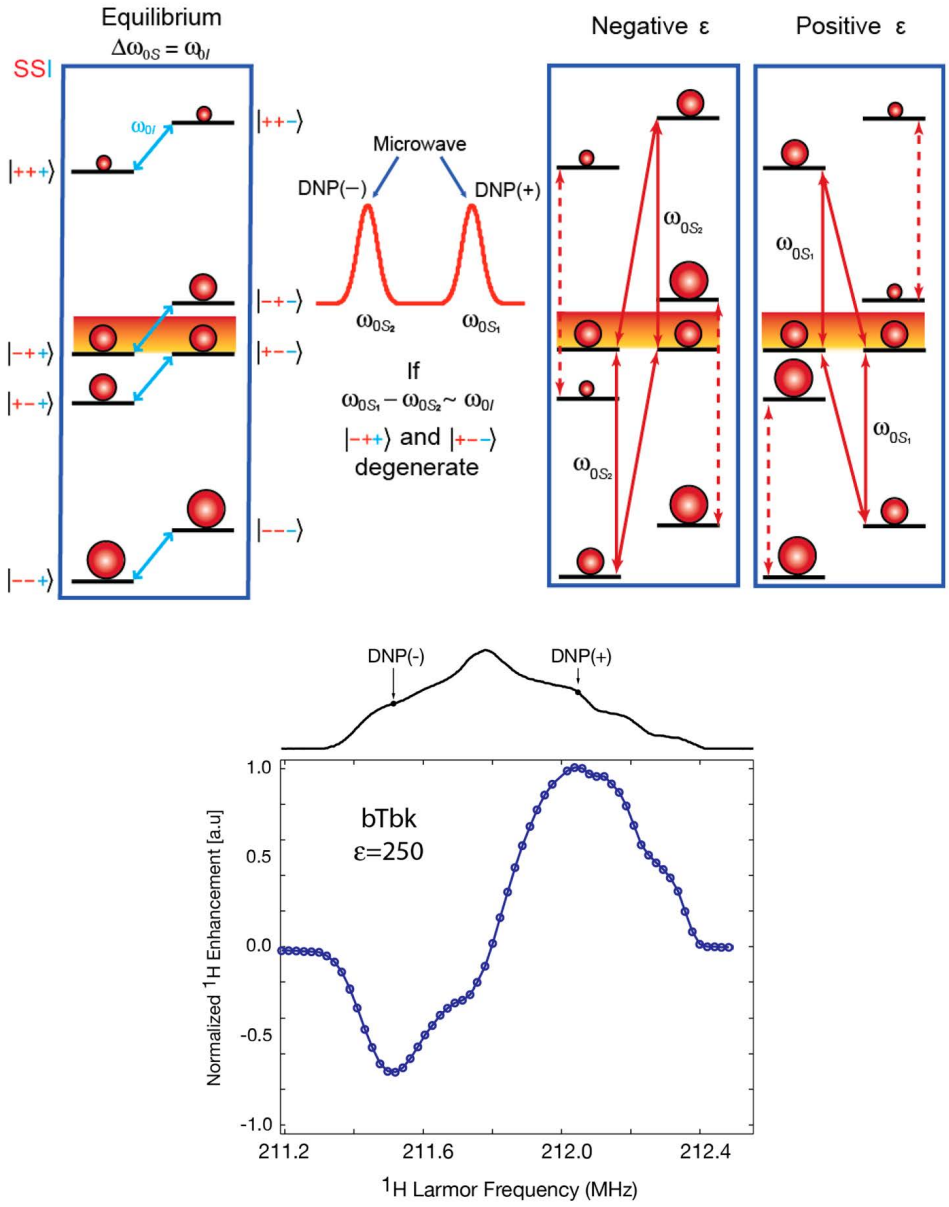

Figure 2.3: (A) Energy diagram illustrating the three spin (two electrons one nucleus) system. At thermal equilibrium (left), under the matching condition, there is degeneracy and equal population of the two shaded levels. The EPR spectrum of an ideal biradical for CE (B) has two narrow lines separated by the nuclear Larmor frequency. Saturation of transitions near the first (second) EPR line gives rise to a positive (negative) DNP enhancement (right). (C) Field profile for bTbk. Taken from reference [31], © the American Chemical Society.

the electron-nuclear coupling Hamiltonian and finally

$$H = d(3S_{1z}S_{2z} - \overrightarrow{S_1} \cdot \overrightarrow{S_2}) + 2J\overrightarrow{S_1} \cdot \overrightarrow{S_2} \tag{2.5}$$

the electron-electron interaction Hamiltonian describing the dipolar coupling (first term) and the exchange coupling (second term). The treatment of this Hamiltonian leads to the eight level energy diagram shown in Figure 2.3. If the central levels are degenerate, then electron-nucleus polarization transfer is possible via saturation of one of the electron transition. The degeneracy will occur if $|\omega_{0e1}\text{-}\omega_{0e2}|=\omega_{0n}$ (so called *matching condition*)

For this effect to be efficient, an ideal system would be two narrow-line radicals whose Larmor frequencies are separated by the nuclear Larmor frequency, unfortunately not easy to find. Another solution would be to use a radical with an inhomogeneous line width larger than the nuclear Larmor frequency. Therefore, at some points of the electron powder pattern, electron spin packets can be found ω_{0n} Hz away, therefore leading to CE. Nitroxide radicals such as TEMPO (Figure 2.4) present anisotropies on the order of the proton Larmor frequency, and therefore can be used as efficient polarizing agents for high-field DNP. As the anisotropy scales with the field, the higher the field, the lesser the spin packets at the right frequency, and therefore ε will be proportional to B_0^{-1}. A more thorough description of this effect can be found in references [33, 37, 38, 39].

Finally, a third effect similar to the CE, called Thermal Mixing (TM) has been reported to be efficient for polarizing nuclei, and is due to the coupling of multiple, rather than two, electrons. However, due to its similarity to the CE, it will not be treated here. For more about this effect see references[33, 40].

The effect through which the sample is polarized depends on the type of radical used[41, 42] but also on the type of nucleus to polarize,[43, 44] on the concentration of the polarizing agent[24, 45] or on the temperature of the sample.[45, 46] The next section of this chapter will focus on polarizing agents designed to polarize protons at temperatures around 100K through the CE. Note that the effects described here concern only continuous-wave (CW) DNP. Other effects have been shown to be efficient polarization mechanism using pulsed DNP.[33]

2.3 Polarizing agents for high-field CE DNP

In this section, we will focus on nitroxide based radicals. Their use as polarizing agents is motivated by several reasons. First they are stable and inert towards many materials. Second the size of their **g** anisotropy makes them ideal candidates to polarize protons. Polarizing protons offers many advantages: protons are one of the most common nuclei, they have relatively short longitudinal relaxation times in the presence of paramagnets compared to lower gamma nuclei, and, in the solid state, proton polarization is homogenized throughout the sample by proton spin diffusion, leading to efficient hyperpolarization of the whole proton spin bath.

The first examples of CE DNP were observed using TEMPO (Figure 2.4).[47] In this molecule, the **g** tensor is strongly anisotropic (g_{xx} = 2.0090, g_{yy} = 2.0061, g_{zz} = 2.0021).[48] The difference between g_x and g_y or between g_y and g_z gives a good CE matching condition. Polarization can therefore be transferred to nuclei if two TEMPO molecules are close enough, with the right orientation (g_{xx} and g_{zz} or g_{yy} and g_{zz} orthogonal), which, in the end, only concerns a small portion of the sample. In order to improve the CE efficiency, Griffin and coworkers introduced in 2004 biradicals where two TEMPO moieties are tethered together by an organic linker with the introduction of the BT*n*E series (see Figure 2.4).[49] This pioneer work proved the importance of increased electron-electron dipole coupling for CE DNP, BT2E being 500% more efficient than TEMPO in the same conditions (ε_H of 250 *vs* 50 at 90K, ω_H=212 MHz and 3.5 kHz spinning frequency).

Another step forward in radical design was taken in 2006 with the introduction of the TOTAPOL biradical[50] (Figure 2.4), a water soluble biradicals yielding high enhancements at low radical concentration. This radical remains nowadays the gold standard for the study of water soluble samples.

For nitroxide biradicals the CE matching condition is, as said before, obtained for a given orientation through the **g** tensor anisotropy and can be fulfilled for the largest number of orientations when the two **g** tensors are nearly orthogonal. For flexible radicals, such as TOTAPOL,[51] only a minority of conformation is expected to yield high DNP enhancements. In 2009, Tordo, Griffin and coworkers introduced the bTbK radical[52] (Figure 2.4), a biradical where the two TEMPO moieties are held orthogonal by a rigid bisketal tether. This radical yields 125% bigger enhancements than TOTAPOL in the same conditions, but unfortunately its solubility in water is quite limited, making it incompatible with most proteins studies.

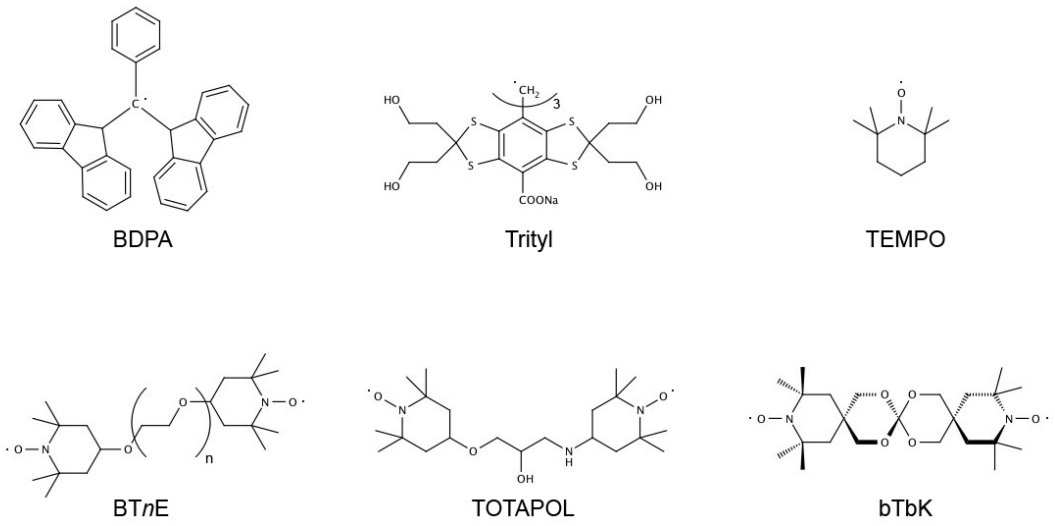

Figure 2.4: Chemical structures of mono and bi radicals used as polarizing agents for DNP experiments.

The field of radical design is rapidly evolving and tremendous progress has been made in the last few years the introduction of rigid radicals soluble in water,[53, 54] in particular AMUPOL,[55] yielding impressive enhancements of 235 at 9.4 T and 100K in d8-glycerol:D_2O:H_2O (60:30:10) (as compared to $\sim$ 70 for TOTAPOL in the same conditions). Although chapter 3 of this thesis focuses on the design of TEMPO based biradicals as polarizing agents for CE DNP, it is noteworthy that promessing alternative have also been introduced over the past few years as polarizing agents such as the use of defects in diamond,[56] triradicals[57] or paramagnetic metal ions.[58, 59] To induce DNP, these radicals have to be irradiated with MW, an issue more complicated than it sounds.

2.4 MAS DNP Hardware

Two different conditions are required to perform a high field DNP experiment: first, the experiment has to be carried out at low temperature ($\sim$ 100K): at higher temperature, the relaxation times of the electron spins are too short to saturate the electron resonances. Low-temperature MAS probes were not commercially available until in the late 90's, because of the complexity of

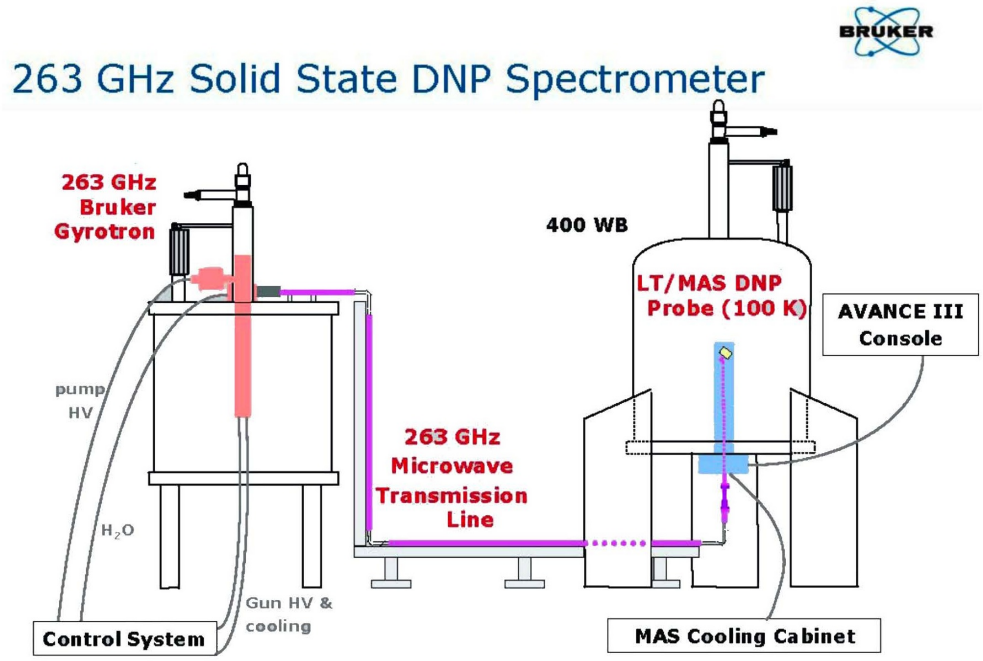

Figure 2.5: Schematic of a Bruker 400 MHz DNP spectrometer

their technology. State-of-the-art low-temperature probes use three independent channel (bearing, drive and variable temperature VT) of N_2 cooled gas to spin the sample and to cool down the probe.[60] Temperatures as low as 80K can be reached, and probes using helium as a cooling gas are currently being developed,[61] potentially yielding to higher ε.

Second, the use of high field use for NMR experiments imposes the use of high-frequency microwaves to match the Larmor frequency of the electrons. The microwave source also has to produce high-power microwaves in order to saturate the electron spin transition. Delivering high-frequency microwaves with reasonable power in the sample causes also several problems. In an usual EPR probe, the B_1 field is created using a microwave cavity resonator.[33] The large quality factor of such probes (Q $\sim 10^3$) makes it possible to create a strong B_1 field in the sample, using low-power microwaves (milliwatts). However, due to the presence of the coil and the MAS apparatus, NMR probes are usually poor resonant cavity for microwaves, with Q close to unity. Using an external high-power microwave source rather than a resonant cavity is a way to circumvent this problem. However, the aim being to carry DNP experiments at high-fields, the external source has to produce high-power and high-frequency microwaves. Until the development of gyrotrons for DNP in

the 90's,[62, 47] most microwave sources failed to fill (at least) one of the criteria. Gyrotrons are able to produce high-power high-frequency microwaves by injecting free electron beams in high vacuum into a metal cavity aligned in a strong magnetic field ($\sim$ 10 T). The electrons then gyrate around the field lines at their cyclotron frequency. The field is designed to compress the electrons as they move through the vacuum tube to a resonant cavity, thus converting some of their transverse kinetic energy into microwaves. The use gyrotrons still introduces a few technical drawbacks : due to the presence of a strong magnet in the gyrotron oscillator, the latter has to be quite far from the NMR magnet to avoid any distorting of the B_0 field.

Transmitting the microwaves over a long distance (several meters) to the sample has to be done with minimal loss of power, and the design of waveguides compatible with the optical mode of the microwaves is far from being trivial. This challenge was addressed by Woskov *et al.* with the introduction of corrugated waveguides,[63] now currently used, yielding with a minimal 0.8 dB power loss from the gyrotron to the sample. A last issue is the design of the rotor. Indeed, it has to absorb very little radio-frequencies and microwaves. Furthermore, it has to be deprived of the nucleus studied. Currently, 3.2 mm sapphire rotors are being used. Finally, the LT MAS technology is still limited to moderately high sample spinning frequencies (typically, ν_r up to 16 kHz are currently used).

Nowadays gyrotrons delivering tens of watts of Continuous Wave (CW) power at 140, 250 and 460 GHz have been built for integration into DNP spectrometers;[62, 64, 65] and 400, 600 and 800 MHz-DNP spectrometers equipped with gyrotrons are now commercially available,[60] which allow the routine application of DNP to many systems. In the following, we will focus on the application of DNP to material science.

2.5 DNP and material science

Since its discovery, DNP was used on materials such as coal, silicon, and diamond thin films until the 90's. In these examples, defects in the lattice served as polarizing agents, making this approach incompatible with high-field DNP. Since its development at high field and until recently, the main focus of DNP has been the study of biomolecular systems, with applications diverse systems such as the investigation of fibrils,[66, 67, 68, 44, 69] membrane proteins,[70, 71, 72, 73, 74, 75] DNA,[76] cellular preparations,[77, 78] or peptidic nanocrystals[79] to quote only but a few examples. In such ex-

periments, the biomolecule is usually dissolved or suspended in a radical containing water-glycerol solution. This solution is then transferred to a rotor and cooled to around 100 K. Glycerol is used as a cryo-protectant to prevent aggregation of the radical and/or crystallization upon freezing. In 2010, the longstanding interest of Anne Lesage, Lyndon Emsley, Christophe Copéret and coworkers for the study of surface organometallic catalysts by NMR led them to apply DNP to probe the surface first of mesoporous silica, but later on to other materials, using an approach dubbed DNP Surface Enhanced NMR Spectroscopy (DNP SENS).

2.5.1 DNP SENS: the first experiment

One of the main challenges in applying DNP to materials is the sample formulation. The materials are, for the most part, intrinsically radical-free and the exogenous polarizing agent needs to be brought close enough to the surface in order to polarize it. The equivalent to the approach used to study biomolecules would be to suspend the materials in the solvent, which may dilute the sample to the extent that any enhancement would not be enough to compensated the decrease in signal due to dilution. In 2010, Lesage *et al.* came up with the idea of using the incipient wetness impregnation technique, to impregnate porous or particulate materials with just enough radical containing solution to fill the porous volume or uniformly wet the surface of particulate materials.[80] For mesoporous SBA type silica materials, typically only 10 μL of radical solution is required to impregnate (and fill the porous volume) of around 12 mg of material. The volume of the sample does not increase significantly during the process, and a slightly tacky powder is obtained, which can then easily be transferred and packed into the rotor. The sample is then inserted in the spectrometer and frozen at around 100K. Upon CW MW irradiation, protons around the radicals are polarized and the hyperpolarization is spread throughout the impregnating solvent via spin diffusion or spin-diffusion like processes. Heteronuclei at the surface can be in turn polarized using CP from the hyperpolarized protons. Initial DNP SENS experiments focused on a phenol functionalized mesoporous silica (**Mat-PhOH**, Figure 2.6) having ca. 0.5 μmol phenol moieties/mg; using TOTAPOL in 90:10 D_2O:H_2O mixture as polarization source. Note that no cryo-protectant is required in such experiments, the narrow pores or space between particles preventing crystallization of the solvent. DNP SENS yielded proton enhancements (ε_H) around 25 and which was then transferred to the surface carbon nuclei by CP. This enabled the acquisition of natural abundance ^{13}C CP MAS spectra of **Mat-PhOH** in only 0.5 h, whereas with conventional NMR, acquisition such spectra at natural isotopic abundance

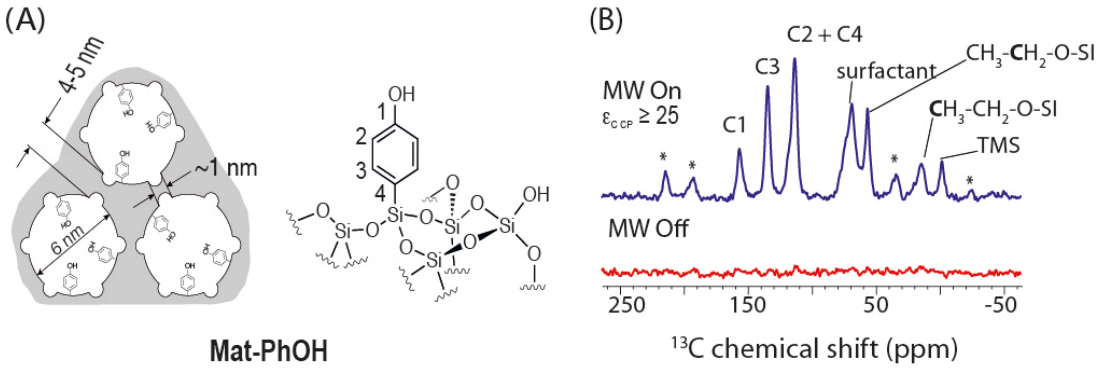

Figure 2.6: (A) Schematic structures of the hybrid mesoporous silica material (**Mat-PhOH**) and a chemical structure of the surface (right) (B) ^{13}C and CP MAS spectra of **Mat-PhOH** impregnated with a TOTAPOL in D_2O/H_2O 90:10 solution acquired with (upper spectra) and without (lower spectra) MW irradiation. Adapted from ref [80].

typically requires more than a half day. This allowed for the observation of all the aromatic resonances of the phenol groups as well as byproducts and remaining templating surfactant. The signal enhancement from DNP SENS also enabled the rapid acquisition (4 h) of 2D dipolar heteronuclear correlation (HETCOR) spectra.

2.5.2 Probing the surface

Quickly after this first demonstration of DNP SENS on **Mat-PhOH**, the technique was applied to probe the binding modes and interactions of the organic moieties to/with the silica surface, by acquisition of DNP enhanced ^{29}Si spectra.[81] The question of conformation of the organic moieties to the surface is highly important since it will impact the activity of the material, and its knowledge is therefore an essential step towards the design of smart functional substrates. A surface silicon atom bearing an organic moiety is called a T site. T sites can be differentiated according to the number n of Si-O-Si bonds it has, leading to the so-called T_1, T_2, or T_3 substructures (Figure 2.7 (B)). Silicon sites only connected to O atoms are called Q sites, with the same differentiation on the number of Si-O-Si bonds. Different T sites have different steric hindering, leading to different geometries of the active site (Figure 2.7 (B)). ^{29}Si NMR is a useful tool to probe the distribution of sites on the surface since different T_n sites have significantly different chemical shifts but suffers from low sensitivity both form the NMR side (4%

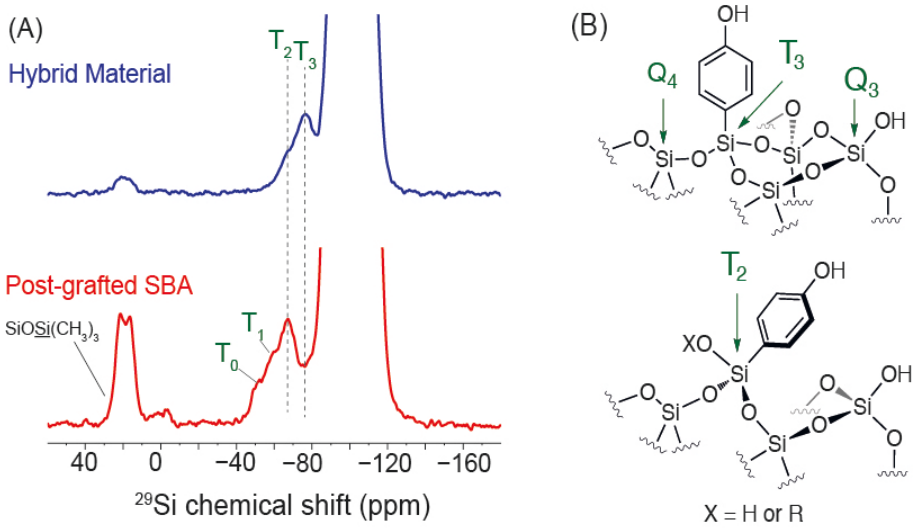

Figure 2.7: ^{29} Si DNP spectra of **Mat-PhOH** obtained by (A) incorporating the organic phenol moiety directly by a sol-gel process, and (B) postgrafting the phenolic units onto a SBA-15 matrix. The signals around 20 ppm correspond to surface $SiMe_3$ groups. (C) Structures of the T_2, T_3, Q_3 and Q_4 species present on the surfaces. Adapted from refs [81, 2]

abundant, γ lower than that of ^{13}C) and the fact that the surface only represents a small fraction of the sample.

In 2011, Lelli *et al.* showed that DNP SENS could be used to probe the distribution of T sites in mesoporous materials, showing in particular that two different synthetic approaches to **Mat-PhOH** (sol-gel VS post-grafting) lead to different distribution of T sites; the later having more T_2 sites which is detrimental for the activity of the material (Figure 2.7 (A)).

The significant gain in experimental time provided by DNP SENS made it possible for Copéret, Lesage, Emsley and coworkers to probe the conformation of the organic moieties in materials similar to **Mat-PhOH** with the surface using ^{1}H-^{29}Si dipolar HETCOR correlation spectra, determining the orientation of the organic linker towards the surface by probing protons proximities to the surface, which could ultimately be linked to the catalyst's activity.[82]

During the past 3 years DNP on materials is a field that developed rapidly,

with various applications by several groups on systems such as other silica nanoparticules, [83] mesoporous silica,[84] polymers,[85, 86] self-assembled materials, [87] or metal-organic frameworks (MOF).[88, 84] DNP was also applied to probe quadrupolar nuclei on the surface of materials such as ^{17}O on MgO oxides,[89] or ^{27}Al NMR on alumina.[90, 91] In order to gain detailed insight on the structure of materials, challenging NMR experiments are required, and therefore higher ε are necessary. The next chapter is devoted to the work done on the development of efficient polarizing agent for CE DNP SENS.

Chapter 3

Design of Polarizing Agents for Cross Effect DNP

The enhancements of ~ 25 obtained during the first DNP SENS experiments allowed for the acquisition of simple 1D spectra and 2D ^{1}H-X dipolar correlation spectra, but remain insufficient for more challenging NMR experiments. As stated in the previous chapter, tremendous progress have been made in radical design, moving from molecular TEMPO to tailored biradicals such as bTbK, for which the orientation of the two nitroxide moieties is optimal, but even so the enhancements are still far from the theoretical limit (660 for protons).

Beyond the geometry, the electronic relaxation properties of radical species are another key factor affecting the DNP process. In the case of the CE, the initial polarization transfer depends on the saturation of an EPR transition, which is facilitated by longer electron spin relaxation times (T_{1e}, T_m). For instance, it was shown in 2011 by Casabianca *et al.* that the efficiency of paramagnetic defects to polarize the bulk in nanoparticulate diamonds increased with increasing T_{1e}.[56] However, this factor has not been so far considered directly in the design of biradicals for DNP. The first part of this chapter will be a light theoretical background on electron spin relaxation (particularly for the case of frozen organic solvents around 100K); and the rest will be dedicated to the experimental results obtained on a series of bTbK derivatives designed to have different relaxation properties.

3.1 Electron Relaxation in Radicals

3.1.1 Longitudinal Relaxation Time

Five main longitudinal relaxation mechanisms have been identified for immobilized isolated radicals (such as a frozen solution of radical in the mM range of concentrations):[92, 93, 94, 95]

The direct process

This process involves a direct energy transfer from the spin systems to the lattice phonon bath, i.e. the electron spin transition occurs when a phonon energy matches exactly that of the spin transition. It is dominant when the temperature of the sample is much less than its Debye temperature (from 20 to 110K for glassy organic matrices), and is not relevant in the range of temperature at which DNP experiments are currently carried out (100K). Its contribution to the relaxation rate is:

$$R_{dir} \propto T \tag{3.1}$$

with T the temperature of the sample.[1]

The local process

This process is due to localized lattice modes and is dominant for molecular solids or covalent lattices (spin labels grafted to a polymer for instance), or at higher temperature ($\sim$ 180 K). It can therefore be neglected in our case. Its contribution to the relaxation rate is:

$$R_{loc} \propto \frac{e^{\Delta_{loc}/T}}{(e^{\Delta_{loc}/T}-1)^2} \tag{3.2}$$

with Δ_{loc} the energy of the local mode in K.

The Orbach process

The Orbach process involves a low energy excited spin state (frequent for transition metal ions) and is not considered here. Its contribution to the relaxation is:

$$R_{orb} \propto \frac{\Delta_{orb}^3}{e^{\Delta_{orb}/T}-1} \tag{3.3}$$

with Δ_{orb} the difference in energy between the excited and the ground state in K.

[1] For a derivation of the direct and Raman process, as well as explanations about the Debye temperature see appendix I.

Solvent	T_{1e}^{a} (ms)	$R_{1e^{b}}$ (Hz)	$R_{ram^{c}}$ (Hz)	R_{th}^{c} (Hz)
H_2O:glycerol	226	$4.41\ 10^{3}$	$4.41\ 10^{3}$	$4.79\ 10^{-1}$
Sucrose octaacetate	81	$1.24\ 10^{4}$	$1.24\ 10^{4}$	$5.03\ 10^{-2}$

a: Electron longitudinal relaxation time calculated as $T_{1e} = 1/R_{1e}$
b: Electron longitudinal relaxation rate calculated as the sum of the Raman and thermal contributions
c: See above for the definition of these terms.

Table 3.1: Electron longitudinal relaxation time and rate for TEMPONE in water:glycerol and sucrose octaacetate at 9.7 T. Results run at 19.4 T yielded the same relaxation rates. The constant used for the simulation were taken from ref [93]

The Raman process

The Raman process is a two-phonon process in which the energy transferred to the lattice is the difference between the energies absorbed and emitted for a virtual excited phonon state. Its contribution to the relaxation rate is:

$$R_{ram} \propto (\frac{T}{\theta_D})^9 J_8(\frac{\theta_D}{T}) \tag{3.4}$$

where θ_D is the Debye temperature of the medium and J_8 is the transport integral given by:

$$J_8(t) = \int_0^t x^8 \frac{e^x}{(e^x - 1)^2} dx \tag{3.5}$$

The thermal process

In this case, the relevant mechanism is a random local motion (libration for instance). The contribution of this mechanism to the relaxation rate is:

$$R_{therm} \propto \frac{\tau_c}{1 + (\omega_0 \tau_c)^2} \tag{3.6}$$

where ω_0 is the electron Larmor frequency τ_c is the decay time of the autocorrelation function and can be estimated as a function of temperature by:

$$\tau_c = \tau^0 e^{E_a/kT} \tag{3.7}$$

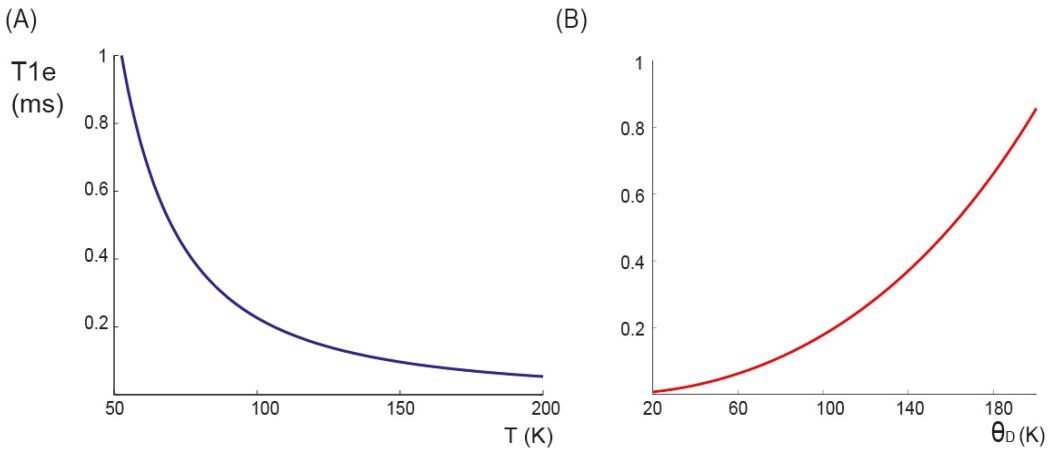

Figure 3.1: Dependance of $T_{1e,Ram}$ on (A) the temperature of a sample with θ_D=120 K and (B)on the Debye temperature of the sample at T=100 K for TEMPONE. The constant used for the simulation are taken from ref [93].

The relaxation rate of nitroxides at 100K in organic glassy matrices can therefore be approximated by the sum the Raman and thermal process relaxation rates. Simulations run on TEMPONE (a derivative of TEMPO) at 100K in different solvents (using values published by Eaton and coworkers)[93] showed that both in water/glycerol and in sucrose octaacetate, the contribution of the Raman process to the relaxation rate appears to be 4 to 6 order of magnitudes larger than that of the thermal process, which can therefore be neglected (see Table 3.1).

Figure 3.1 shows the calculated dependance of electron longitudinal relaxation time induced by a Raman process $T_{1e,Ram}$ for TEMPONE on (A) the temperature of a sample with θ_D=120 K (B) the Debye temperature of the sample at T=100 K. As expected, $T_{1e,Ram}$ diminishes with the temperature. More interestingly, $T_{1e,Ram}$ increases with θ_D. The Debye temperature is a parameter that quantifies the rigidity of the system: the higher θ_D the more rigid the system. Based on these results, it has been shown that the efficiency of this two phonon process decreases with the increasing molecular weight/rigid volume of the radicals.[94] This is an experimental parameter that can be taken into account in the design of biradicals, leading to new principles for radical design.

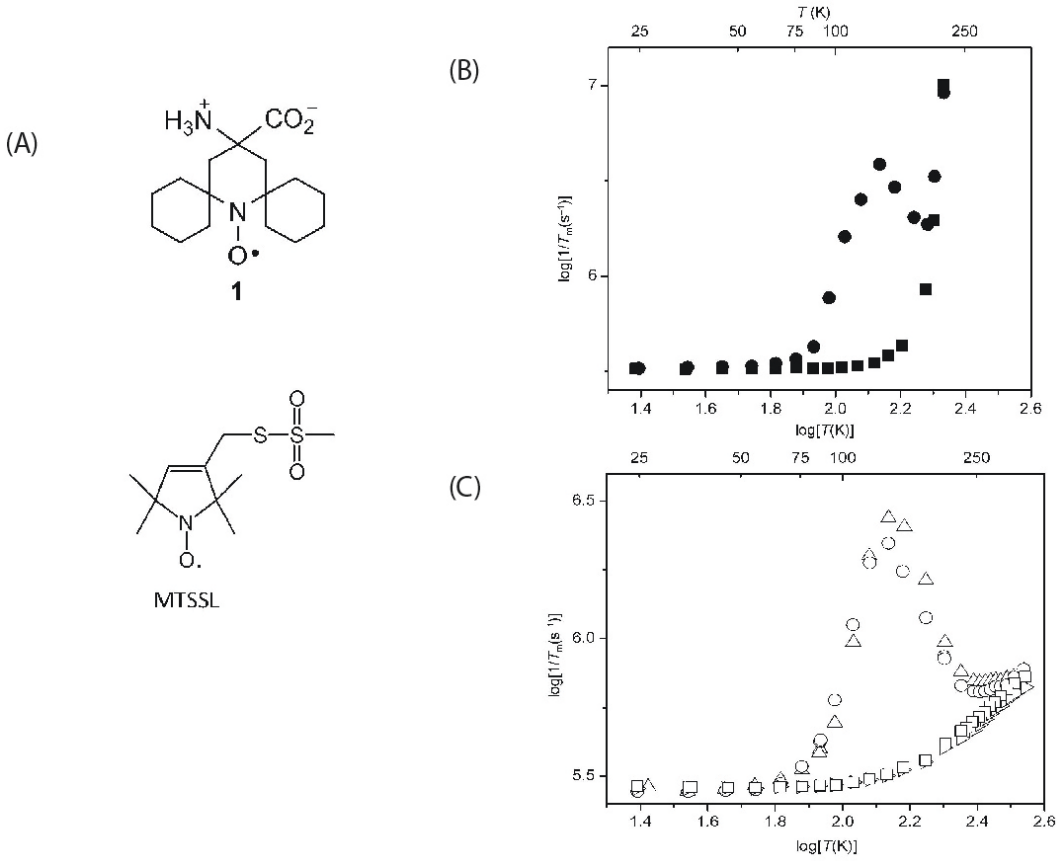

Figure 3.2: (A) Molecular structure of compound 1 and MSSTL. Temperature dependance of $1/T_m$ for 1 (squares) and MSSTL (circles) in (B) 1:1 water:glycerol and (C) 1:1 PVA/borate. Adapted from ref [96].

3.1.2 Transverse Relaxation times

The electron phase memory time, T_m, is the time constant that governs the decay in a spin-echo experiment. The processes responsible for the dephasing of the electron spins is different from those involved in longitudinal relaxation. The main processes impacting the dephasing rate ($1/T_m$) are molecular motions (that averages inequivalent electron-nuclei couplings), electron-electron spin-spin interactions and, at low temperature, spin diffusion.[94] The development of radicals with long T_m is of longstanding interest for the scientific community as they find applications in distance measurements in the nanometer range in biomacromolecules (using site-directed spin labeling (SDSL) in combination with pulsed EPR). In the range of temperature used in CE DNP (between 70 and 250K), rotation of a nitroxyl ring methyl

groups have been reported to be very efficient at enhancing the electron spin echo dephasing. In 2009, Kathirvelu *et al.* introduced two spirocyclohexyl derivatives of TEMPO, where the gemdimethyl groups in α position of the nitroxide center had been replaced by a spirocyclohexyl group (see Figure 3.2).[97] These radicals have been designed to retain longer T_m and therefore allow to perform double electron-electron resonance (DEER) experiments at higher temperatures. Subsequently, a amino acid spin label version of these radicals was developed in order to be grafted to biomacromolecules.[96] Figure 3.2 shows the temperature dependence of $1/\mathrm{T}_m$ for 1 and MTSSL in (B) 1:1 water glycerol and (C) 1:1 PVA/borate. In both solvents, methyl-rotation enhanced relaxation can be seen for MTSSL. Relaxation rates at higher temperatures are governed by increasing molecular motion due to the softening of the glass (different for both solvents). The advantage of synthesizing biradicals equivalent of these spirocyclohexyl radicals would be double: the lack of methyl groups would increase T_m and the increased bulkiness would at the same time make T_{1e} longer.

With this in mind we designed, in collaboration with the group of Paul Tordo in Marseille, a series of bTbK derivatives expected to differ from one another only by their relaxation times.

3.2 Large Molecular Weight Nitroxide Biradicals for Efficient CE DNP.

As stated before, CE DNP requires saturation of one of the electron transition in order to enhance nuclear polarization. The efficiency of the CW saturation of the electron spins depends on the saturation factor s ($s = {T_{1e}}^{*} T_m$). The higher s, the more efficient the saturation will be. We expect therefore that, if all the other parameters (**g** and **A** tensors, structure of the radicals, $e-e$ dipolar couplings) are constant, then the DNP efficiency of the radicals will increase with their saturation factors. In order to benefit from the optimal configuration of bTbK (where the orientation of the two **g** tensors is thought to be optimal for polarizing proton through CE DNP); and to access a range of radicals with the same EPR tensor parameters and relative orientations, but with different electron spin relaxation properties, derivatives of this biradical have been synthesized. A synthetically feasible way to obtain such radicals is to modify the derivatives at α position (Cα) to the nitroxyl groups (N-O) while maintaining the rest of the skeleton (see ref [98] for details of the synthesis).

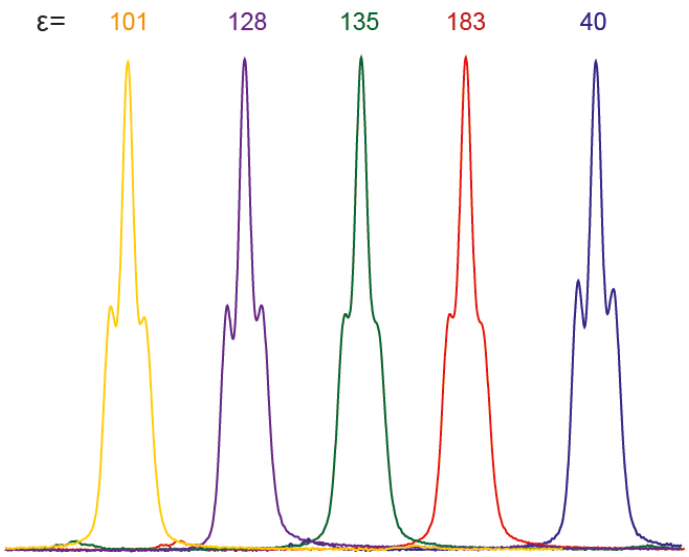

Figure 3.3: ^{1}H-^{13}C CP MAS spectra of 16 mM solution of TEKPol in TCE obtained during the reproducibility tests. The enhancement is displayed on top.

3.2.1 Sample preparation and glass formation.

NMR

DNP experiments were conducted on a commercial Bruker Avance III 400 MHz NMR spectrometer equipped with a 263 GHz gyrotron microwave source, using a 3.2 mm triple resonance MAS probe at sample temperatures around 100 K (unless noted otherwise). The microwave power was set to maximize the DNP enhancement (∼4 W power at the sample). The magnet sweep coil was used to set the magnetic field to coincide with the maximum enhancement for TEKPol (which was found to be the same as for TOTAPOL).[98] Proton DNP enhancements were measured on spectra acquired after a short (1 rotor cycle) spin echo to remove probe background, and the enhancements of heteronuclei were measured after cross-polarization (CP) from protons. The samples were either bulk solutions or mesoporous silica materials impregnated with biradical solution. All solutions where made using 1,1,2,2-tetrachloroethane (TCE) as a solvent. The choice of this solvent is explained in details in the next chapter. Samples were topped with a Teflon insert to minimize solvent leakage from the sapphire rotors. A spatula tip of KBr was added at the bottom of the rotor to enable measurement of ^{79}Br chemical shifts for temperature calibration.

EPR

EPR experiments were conducted at W Band (94 GHz) on a Bruker Elexsys E680 EPR spectrometer at a temperature of 100 K in TCE, unless noted otherwise. Fitting of the experimental curves is discussed in the next section. To match the DNP conditions, samples were recorded at a high radical concentration (16 mM). For comparison, bTbK, bCTbK, and TEKPol were measured at low concentration (0.2, 0.1, and 0.1 mM, respectively). The results are discussed below.

Glass Formation

Experimentally, we observed variations (up to 80%) of the DNP enhancement in TCE solutions for some radicals upon freezing of the sample in the magnet. Several freezing and thawing cycles were performed by inserting and ejecting the sample from the probe. We report here the highest ε. "Flash" freezing the rotor in liquid nitrogen did not yield consistently better ε. The quality of the glass formed by freezing the sample is well-known to be an important factor for both DNP and EPR. Poor glasses or crystalline domains formed in the sample will lead to shortening of the relaxation times by creating zones of high local radical concentration, therefore attenuating the DNP process. This is why cryoprotectants, such as glycerol, are used in DNP experiments in water,[99] which crystallizes when frozen, or why alternative sample preparation schemes are being developed.[80, 100] For samples yielding poor DNP enhancements, the ^{13}C NMR spectra display two shoulders due to residual coupling to chlorine. They might indicate formation of crystalline domains in the sample (see Figure 3.3). In contrast reproducible enhancements were obtained when impregnating mesoporous materials. Since then, we have found that adding a small amount (e.g. 5 %) of deuterated methanol to TCE yields more robust and reproducible glass formation.
EPR samples in small (0.5 mm) capillaries were frozen in liquid nitrogen prior measurement. Results were reproducible, and the samples were visually transparent and homogeneous, indicating glass formation.

3.2.2 Molecular Geometry and EPR Characterization of the Biradicals.

Figure 3.4 shows the radicals used in this study. 4 (bCTbK) was the first radical to be synthesized and tested in 2012.[101] This radical performed better than bTbK in the same conditions, which could be correlated to slower electron relaxation. A more thorough study was then realized in 2013 on

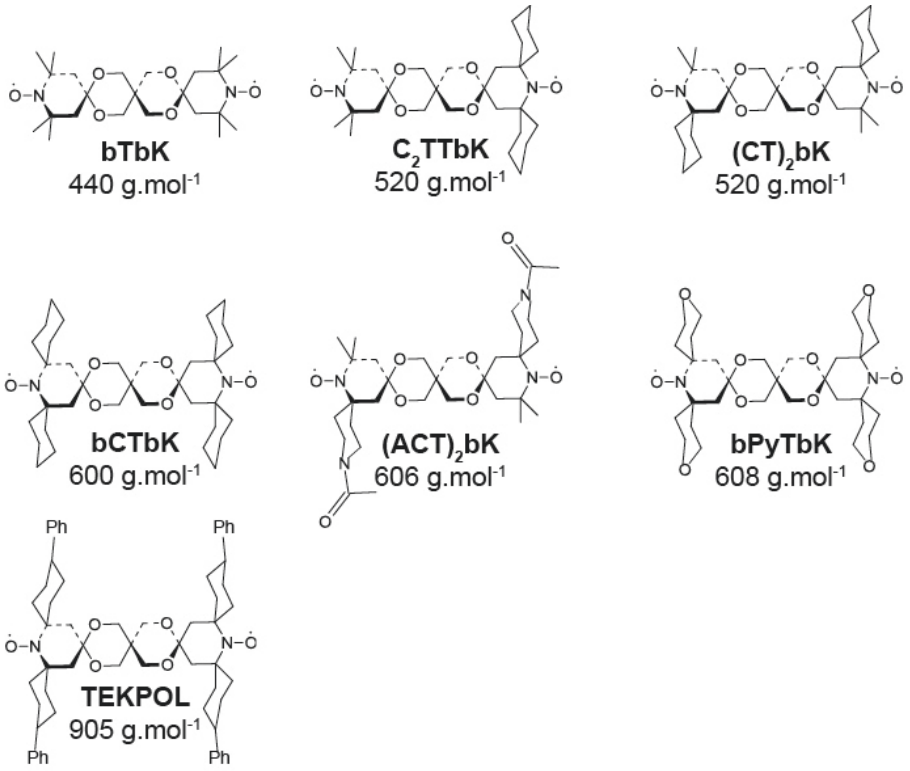

Figure 3.4: Structure, name, and molecular weight of the radicals investigated in this study.

compounds 1-7.[98] Comparison of single crystal XRD (where available) or DFT calculations for 1, 4, 6, and 7 (see Table 3.2) shows that as expected, the average distance between the two unpaired electrons (and thus the $e-e$ dipolar coupling) as well as the orientation of the two CαN(Oλ)Cα average planes are very similar throughout the series. In addition EPR spectra recorded at low temperature indicate that their **g** tensors are almost identical.[98] Figure 3.5 A,B shows the inversion recovery (T_{ir}) and phase memory (T_m) times measured for the radicals as a function of molecular weight. The experiment was performed near the ^{14}N m_I = -1 hyperfine component along g_{zz} of the EPR spectrum, corresponding to the optimum DNP irradiation frequency (as the relaxation times vary along the EPR powder pattern). The biradical concentration in the solution for EPR was determined by CW EPR spin counting experiments and was found to vary between 11.0 and 14.7 mM. At these relatively high concentrations, the measured inversion recovery and phase memory times do not correspond to the electron longitudinal

Coumpound	R_{o-o}(Å)[a]	R_{N-N}(Å)[a]	<R>[d]	D[f](MHz)	q[e] (°)
bTbK,(1)	13.030[b] *13.342*[c]	10.777 *11.034*	1.599 *1.724*	32.62 *30.36*	79.57 *80.36*
bCTbK,(4)	- *13.249*	- *10.990*	- *1.695*	- *30.77*	- *77.56*
bPyTbK,(6)	13.148 *12.789*	10.890 *10.672*	1.639 *1.538*	31.82 *33.91*	89.69 *73.39*
TEKPOL,(7)	13.457 *13.192*	11.092 *10.953*	1.754 *1.667*	29.73 *31.29*	64.72 *77.34*

a: Distance between the oxygen or the nitrogen atoms of the nitroxide moieties
b: From X-ray data
c:Calculated DFT [B3LYP 6-31 G (d,p)] value.
d:$1/<R>=(1/R_{o-o}+1/R_{N-N})/2$
e:Angle between the average CαN(O•)Cα planes
f:Calculated from the dipole point approximation D = 52 160/<R>

Table 3.2: Structural characteristics and e-e dipole coupling for: bTbK (1), bCTbK (4), bPyTbK (6) and TEKPol (7)

and transverse relaxation times as intermolecular relaxation, such as spin exchange or dipolar coupling plays a role in the process. We note however that these data are recorded under experimental conditions that are close to those used during the DNP experiments, and are thus the most relevant to our results. The most significant difference in conditions is the EPR frequency, which here is 94 GHz. However, the electron relaxation times of nitroxides in glassy organic solvents around 100 K are not expected to vary significantly between 94 and 263 GHz. Thus the values reported here will not be exactly the same as those at the DNP frequencies (spectral diffusion will increase at higher fields), but they are expected to follow the same trends. The inversion recovery curves were fitted using a stretched exponential function to take into account a distribution of inversion recovery time constants due to the orientation dependence of vibrations, molecular motion, spin-orbit coupling.[102] The mean relaxation times are given here. T_m was fitted using a monoexponential function.

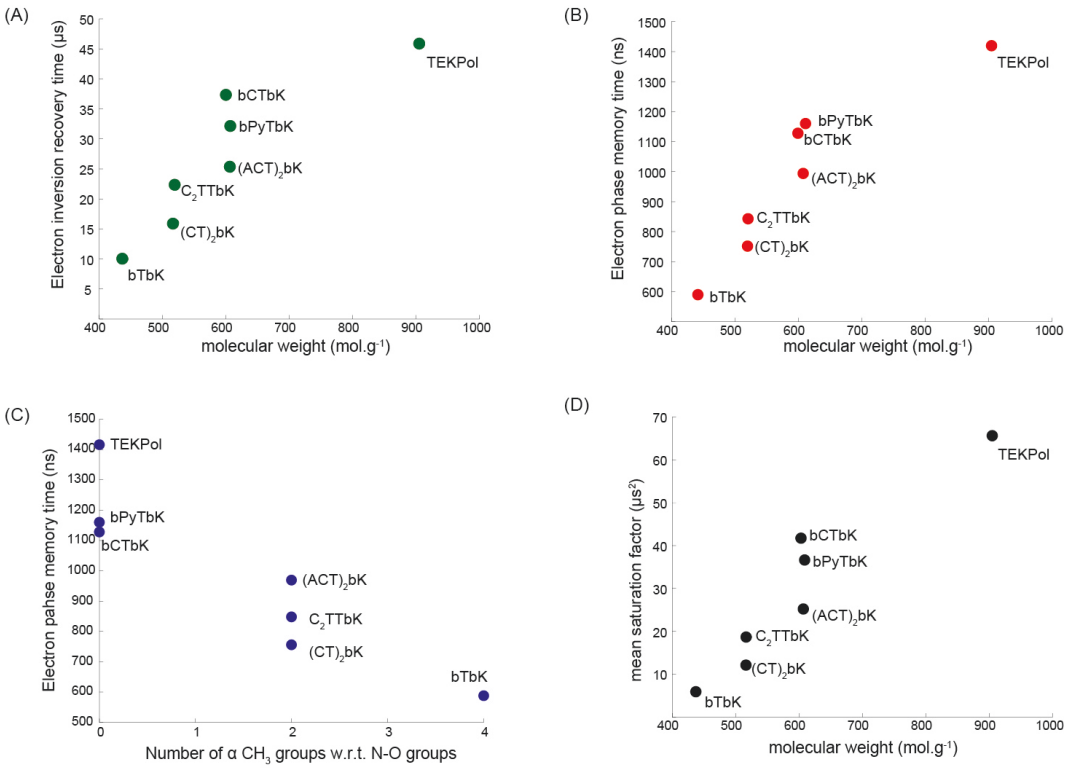

Figure 3.5: (A) Electron inversion recovery times (T_{ir}), (B) electron phase memory time (T_m) as a function of molecular weight for the different radicals, and (C) electron phase memory time (T_m) as a function of the number of methyl groups groups at the Cα carbons. (D) Saturation factor s as a function of molecular weight for the different radicals. (All measurements were done with 16 mM solutions in TCE at 100 K. The EPR experiments are done at W band (94 GHz). Taken from ref [98].

The electron inversion recovery times (Figure 3.5 (A)) measured for biradicals 1-7 show a roughly linear dependence on the molecular weight of the biradicals, as discussed in detail below, coherent with relaxation driven by a Raman process. Since molecular weight is not the only factor in determining relaxation times, some differences are observed in relaxation rates for radicals with similar molecular weight in Figure 3.5, as is demonstrated by 4 bCTbK, 5 $(ACT)_2$bK, and 6 bPyTbK. Sato *et al.* described electron spin relaxation for nitroxide radicals in glassy solvents at temperatures between 100 and 300 K using models that involved the corrected temperature T' = $TV^{-\gamma}$, where T is the temperature, V the molecular volume of the radical, and γ a parameter that characterizes the medium and is dependent on lo-

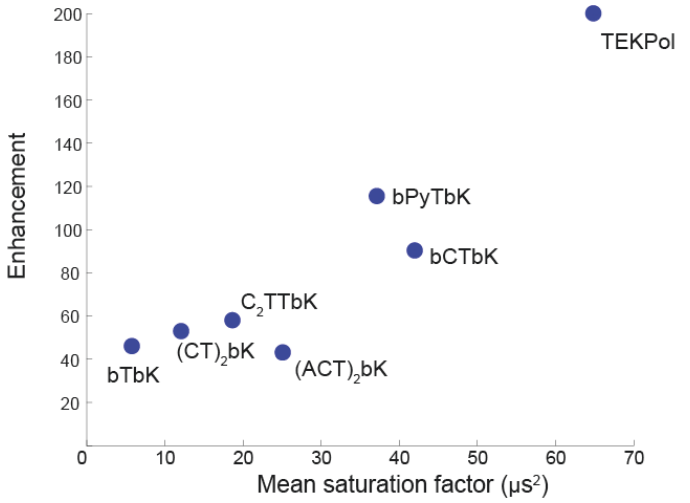

Figure 3.6: ^{13}C enhancement after CP from protons for 16 mM bulk solutions in TCE as a function of the mean saturation factor.Taken from ref [98].

cal molecular motion[94]. Their model predicts that bulkier radicals lead to slower relaxation and also that local motion affects relaxation. Furthermore for a biradical with interspin distance about 9 Å these authors showed[102] that nitroxide-nitroxide interactions have little impact on electron spin relaxation. Biradicals 4-6 have roughly the same molecular mass, but 5 has four methyl groups at the Cα carbons and two additional N-acetyl methyl groups. This is in line with the observation in Figure 3.5 that 4 has a shorter relaxation time than 6 which is in turn shorter than that for bCTbK.

Figure 3.5 (B),(C) show, respectively, the impact of the molecular weight and of the number of methyl groups at Cα carbons on T_m . As expected, heavier radicals or radicals without methyl groups exhibit longer T_m. As expected the mean saturation factor s ($s = T_{ir}\ {}^{*}T_m$), which reflects the ability to saturate the EPR transitions, increases with molecular weight as shown in Figure 3.5 (D).

3.2.3 DNP enhancements

Figure 3.6 shows the measured proton DNP enhancement of the solvent (measured on the ^{13}C resonance of the solvent in a standard CP MAS experiment) obtained as a function of the mean saturation factor. As predicted, the DNP enhancement is seen to increase with the mean saturation factor and therefore with the molecular mass of the polarizing agent. In particular, TEKPol,

with a molecular weight of 905 g·mol^{-1}, a 94 GHz mean saturation factor of 65.0 μs^2, and an enhancement of 200, far outperforms the other biradicals and notably the previous best bCTbK which gives an enhancement of 80. We note that it is expected that the DNP enhancement will go through a maximum at some point for higher saturation factors. An optimum saturation factor is predicted since the degree of saturation of the EPR transition is improved at a given microwave power for larger saturation factors, whereas for repeated polarization transfer from the same electron spin to nuclei, the electron spin polarization must recover, so that shorter T_{ir} will increase turn over. However, we only expect to see this effect for significantly longer electron relaxation times than studied here; or at significantly lower temperatures. For dinitroxides at the temperatures and fields used here we expect DNP enhancements to continue to increase with increasing saturation factors.

This work shows the impact of higher saturation factors on the DNP enhancements. Other types of radicals, such as mixed biradicals having radical moieties with one long T_{ir} and one short T_{ir} have been predicted to have high DNP enhancement;[41] and very recently experimentally verified by Michaelis *et. al* who used a mixture of BDPA and trityl to polarize ^{13}C through the CE.[103] They proved that the asymetric field sweep profile observed could be correlated to the radical's T_{1e}s: saturation of the BDPA centre (T_{1e} of 3.6 ms) is more efficient and the shorter T_{1e} of the trityl (1.4 ms) allows for quick recycling of the CE mechanism.[103]

3.2.4 Temperature Dependence of DNP Enhancements

A key objective in the development of solid-state DNP experiments is to be able to use higher sample temperatures. This is particularly relevant to proteins samples where resolution is often (but not always) degraded at temperatures below 200 K.[104] ε is known to be strongly dependent on the temperature of the sample, with a steep decrease as temperature increases. Figure 3.7 (A) shows the temperature dependence of ε for bTbK, bCTbK, and TEKPol. In these experiments, a spatula tip of crystalline KBr (which is insoluble in TCE) was added to the rotors, and the sample temperature was calibrated by using the ^{79}Br chemical shift as an internal standard.[105] As expected, ε decreases as the temperature increases for all three radicals. However, whereas bTbK exhibits the typical rapid decrease already observed for TOTAPOL in glycerol/water, both bCTbK and TEKPol show a slower decrease with temperature over the range covered here. As a consequence, at around 140 K, ε is reduced by 60% from the value at 106 K for bTbK but only by 40% for both bCTbK and TEKPol. At around 176 K bTbK yields

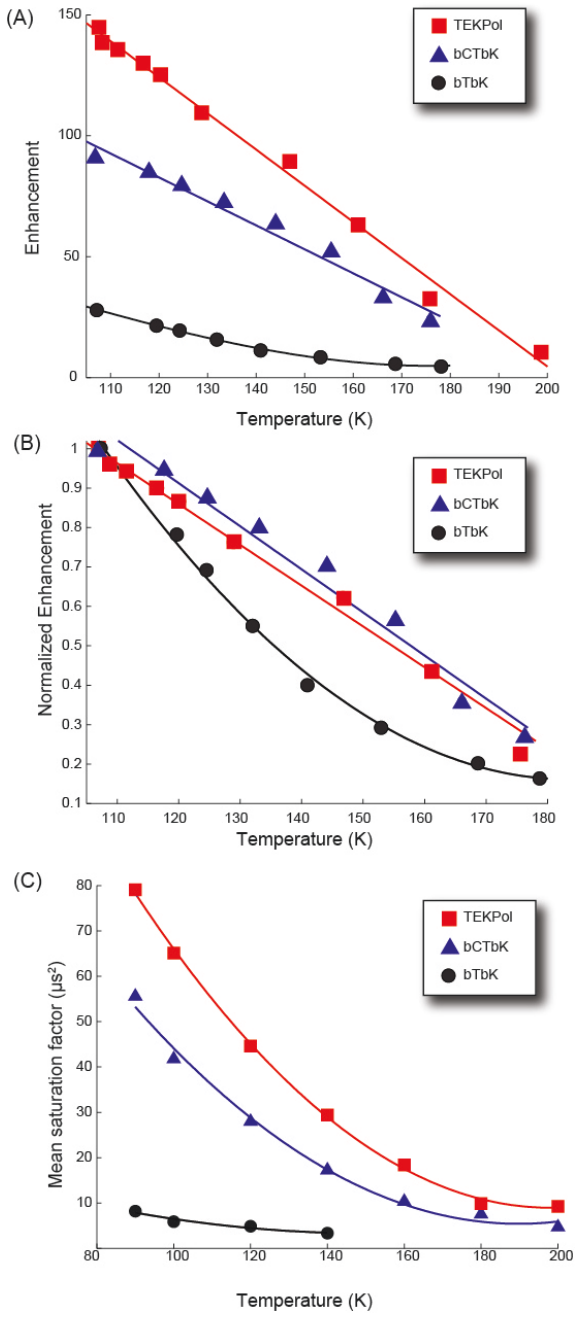

Figure 3.7: (A) Enhancement, (B) normalized enhancement, and (C) the mean saturation factor as a function of temperature for TEKPol (red squares), bCTbK (blue triangles), and bTbK (black circles). The lines are guides for the eye. Note that T_m becomes too short to detect an EPR echo at temperatures higher than 140 K. Taken from ref [98].

enhancements of only 4.5 (ε / $\varepsilon_{100K} = 0.16$), and bCTbK and TEKPol have ε of 24 (ε / $\varepsilon_{100K} = 0.25$) and 33 ($\varepsilon$ / $\varepsilon_{100K} = 0.23$), respectively. Variation of the proton nuclear longitudinal relaxation time with temperature has been shown to affect the DNP enhancements. However, for radical solutions in TCE, proton T_1 only varies slightly (from 2.0 to 2.6 s) in the range of temperature investigated. The temperature dependence of the enhancement can more credibly be linked to the temperature dependence of the electron relaxation times. As seen in Figure 3.7 (C), the saturation factors indeed decrease significantly with increasing temperature.

A key structural difference between bTbK and bCTbK or TEKPol is the presence of methyl groups at the Cα carbons of the former. Motion, and in particular the rotation of the methyl groups, is the dominant process for transverse relaxation, and the impact of temperature is therefore expected to be larger on T_m for bTbK than for the other radicals, which could explain the observed difference. Unfortunately, due to short T_m, measure of relaxation parameters could not be conducted at temperatures higher than 140 K for bTbK. As said before, this difference of behavior in T_m was previously observed for monoradicals with methyl groups at the Cα carbons vs radicals with cyclohexyls in the same position.[97, 96] It is also interesting to note that the widely used radical TOTAPOL, which also has methyl groups at the Cα carbons has been reported to present a similar temperature dependence to that of bTbK.[60] Most interestingly, TEKPol maintains enhancements of 12 at 198 K. Recently, Sauvée *et al.* introduced two very efficient water soluble biradical, PyPol and AMUPOL, where the gemdimethyls groups in α of the nitroxide are also replaced by six membered rings.[55] As in our case, they showed a clear correlation between the enhanced efficiency of these polarizing agents and their longer relaxation times compared to TOTAPOL. Furthermore, the same linear temperature dependence profile for ε could be observed for AMUPOL both at 400 and 600 MHz.

To investigate the effect of the presence of methyl groups on the temperature dependance of ε, a deuterated version of bTbK (where the 24 protons on the methyl groups in α o the nitroxides have been replace with deuterons) was synthesized. Preliminary data show a slight improvement in ε, and the temperature profile of ε still remains to be done before any conclusion is drawn (unpublished data).

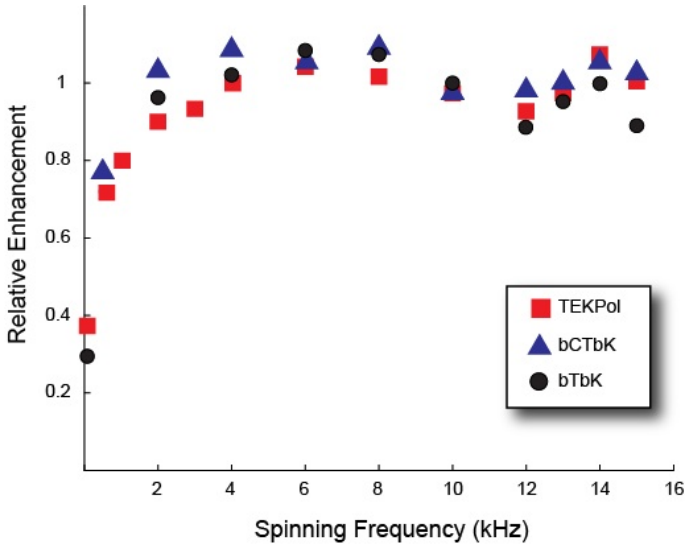

Figure 3.8: Relative enhancement dependence on the spinning frequency of the sample for TEKPol (red square), bCTbK (blue triangles), and bTbK (black circles). Taken from ref [98].

3.2.5 MAS Frequency Dependence of ε

Another important parameter is the spinning frequency dependence of the enhancements. Fast spinning is necessary for the study of many materials and biomolecules. The typical behavior for ε observed and reported with spinning frequency is first to increase and then go through a maximum (usually around 4 kHz spinning frequency) and then decrease as the spinning frequency increases to 12 kHz. Rosay *et al.* attributed this behavior primarily to an increase in sample temperature due to frictional heating with the spinning frequency.[60] More recently, Mentink-Vigier *et al.* and Thurber and Tycko developed a theoretical two-electron one-nucleus model for MAS CE DNP where the spinning frequency dependence is explained by energy level crossings and anticrossings.[39, 38]

We performed a temperature-controlled experiment for a 16 mM solution of TEKPol in TCE using the ^{79}Br chemical shift from KBr as an internal thermometer, as above. The ^{79}Br chemical shift was recorded at the highest spinning frequency (14 kHz), and for lower spinning frequencies the temperature control setting was increased so that the ^{79}Br chemical shift matches the one at 14 kHz. In this way, the experiments are carried out at the same

temperature at all spinning frequencies. It turns out that the difference with respect to the spinning frequency dependence measured without correction for frictional heating is minor for the radical/solvent mixtures studied here.[98] Figure 3.8 shows the spinning frequency dependence measured for the three radicals investigated. For clarity, to compare the behavior, only the normalized enhancements are displayed. Interestingly, the curves show a decrease in efficiency from about 6 to 12 kHz, as expected, but they all then show an increase to a second maximum at around 14 kHz. We do not have an explanation for this interesting behavior. The three radicals show largely the same MAS dependence despite their different T_{ir}. The differences in T_{ir} may not be large enough to produce an observably different functional form.[39] Note that enhancements of over 160 are obtained at high spinning frequencies (15 kHz) for TEKPol. Similar flat profiles for ε up to 14kHz spinning rate have been reported by Sauvé *et al.* on the AMUPOL biradical.[55]

Electron relaxation times are now a criteria taken into account to explain the efficiency (or lack thereof) of new polarizing agents as shown with the subsequent work by of Michealis *et al.* and Sauvée *et al.*.[55] Still in 2013, Mao *et al.* showed that macrocyclic hosts could be used to enhance the solubility of bTbK in water, resulting in very efficient polarization of the sample;[106] and could correlate the high ε to higher saturation factors.

3.2.6 Bigger is still better

Very recently, we managed to develop heavier derivatives of TEKPOL called in a poetic manner TEKPOL2 and TEKPOL3 (Figure 3.9). TEKPOL2 and 3 outperformTEKPOL with ε of 235 and 229 respectively, which can be correlated with their molecular weight as expected. Furthermore, the reproducibility of ε was not an issue in this case, and the crystallization issues observed for TEKPOL solutions in TCE were not present for these two radicals; thereby strengthening the hypothesis that glass formation of the TCE is radical-dependent. In the case of TEKPOL, we also observed that adding 5% deuterated methanol helped with the glass formation. EPR measurements still remain to be performed on these 2 new derivatives in the bTbK series.

Interestingly, during the multiple insert-eject cycles to test the reproducibility of ε, it was realized that both ε and $T_1(^1H)$ increased at each cycle. We attribute this effect to de-oxygenation of the solvent, due to the contact with a pure N_2 atmosphere during the freezing/thawing cycles. O_2 concentration in solvents can be quite high (up to ~ 10 mM), and this paramagnetic molecule will be an efficient relaxation source for both the electrons and pro-

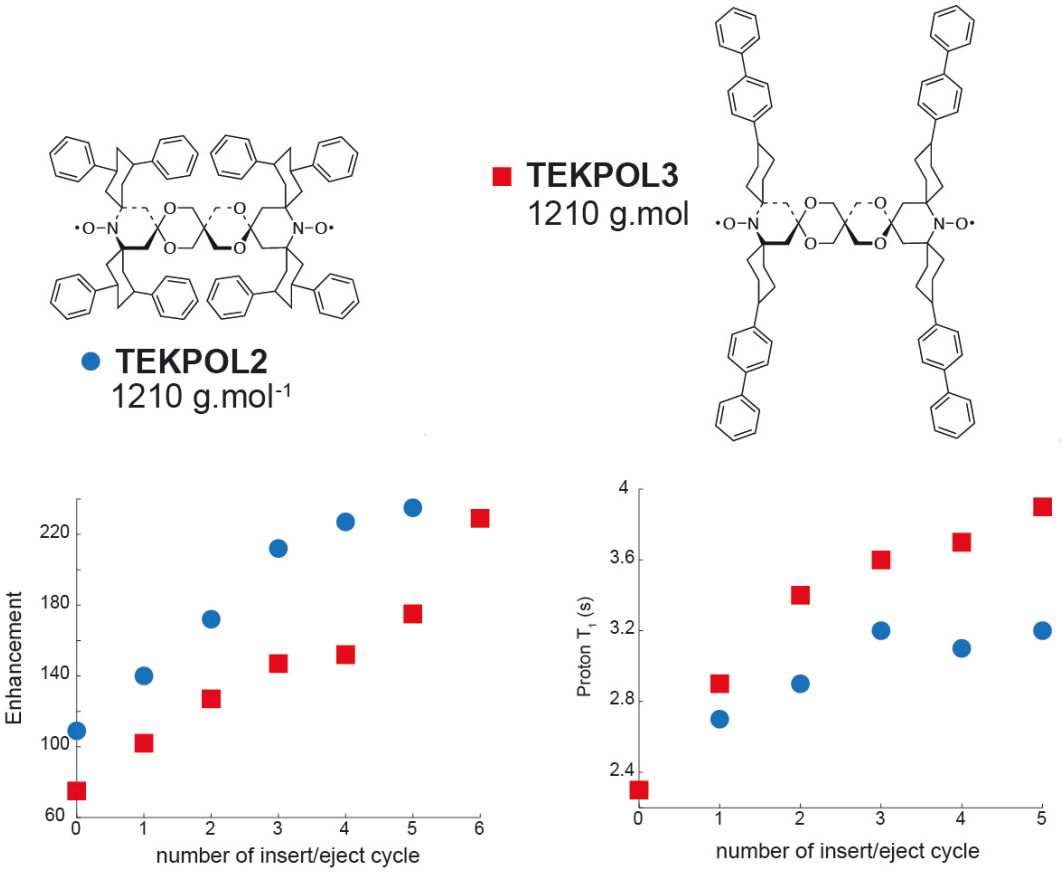

Figure 3.9: Molecular structure and molecular weight of TEKPOL2 and 3, and the dependance of $T_1(^1H)$ and ε on the number of insert/eject cycles

tons in the systems, thereby diminishing ε. The effect of de-oxygenation of the solvents on ε was already observed by Rosay and coworkers in the case of aqueous solutions.[99] The increase in T_1 leads to longer acquisition time but the overall gain in sensitivity gained by oxygen removal remains more important in our systems. More experiments are required to confirm this effect, in particular the use of de-oxygenated solvents to prepare the solutions.

The development of bTbK derivatives has lead to a slightly deeper understanding of the DNP processes with the illustration of the importance of electron relaxation times on the DNP enhancements. However, biradical polarizing agents are not limited to the bTbK framework, as illustrated, for instance, with the introduction of the very efficient AMUPOL.[55] Recently, we also introduced functionalized materials with nitroxides grafted on the surface to be used as polarizing agent.[107] Although their development is

aimed at dissolution DNP, they were proven to be efficient in polarizing bulk solution and could be used as distant polarizing source for sensitive materials.

Performance of radicals in frozen solution is very important and often a good indicator of their efficiency for studying materials. However, the efficiency of radicals in impregnated materials can be quite different due to interaction with the surface. In the following chapter, we try and see how this interaction impacts the DNP enhancement as well as the NMR properties of the material studied.

Chapter 4

SENS and Sensitivity

Getting the highest ε is the ultimate goal when designing polarizing agents, but the situation is quite different when DNP is applied to actual systems, where only *sensitivity* matters. In this chapter, the focus is put on the quantification of the sensitivity enhancement, a more complex matter than just comparing MW On and Off intensities. More generally, the optimization of the sample formulation for a few systems such as organometallic complexes grafted on the surface of mesoporous silica will be discussed. A first step will be to see how non-aqueous solvents can be used to perform DNP experiments, enabling the application of DNP to air and moisture sensitive compounds; then we will discuss the quantification of the sensitivity enhancement provided by DNP SENS, before focusing on optimal sample preparation and interaction between the radicals and the different types of surfaces.

4.1 From model to functionalized materials: Non-aqueous solvents for DNP SENS

As previously mentioned, many modern materials such as heterogeneous catalysts are air and moisture sensitive or display hydrophobic surfaces, and are therefore incompatible with impregnation with a radical solution in water. The feasibility of using non-aqueous solvents for DNP was investigated, using the bTbK biradical as a polarizing agent. This biradical is more soluble in organic solvents than TOTAPOL and has been reported to yield better enhancements in a mixture of DMSO and water than TOTAPOL does at the same concentration;[52] and at the time of the investigation, the bulkier and more efficient bTbK derivatives seen in the previous chapter were not available. All the solvents were tested for DNP efficiency on **Mat-PhOH** (remember chapter 2), as it was shown that the presence of the material

helped with the glass formation. A total of 20 solvents were tested under DNP conditions.

Identification of organic solvents suitable for DNP SENS experiments.

The solvents used for this study were chosen according to three main criteria:

1. The solvent must be chemically inert at room temperature on a short time scale towards both the radical and the material (so the polarizing agent or the material will not decompose/react).

2. The vapor pressure of the solvent at room temperature has to be relatively low to allow the material to be wetted and then transferred to the rotor before it dries out.

3. The solvent must be frozen at the temperature at which the DNP experiment is performed. This eliminates large-scale molecular motion, and guarantees in large inter-molecular ^{1}H-^{1}H dipolar couplings, enabling spin diffusion to uniformly distribute enhanced polarization throughout the sample; and also increases the proton T_1. As it is a well known fact that solvents confined in meso/micro-pores have depressed freezing points in comparison to free bulk solvents, most of the solvents have been chosen to have a relatively high freezing point (i.e. above 150 K).[108, 109]

Table 4.1 displays the observed proton and silicon DNP enhancements (ε_H and $\varepsilon_{Si\ CP}$, respectively) obtained for **Mat-PhOH** wetted with bTbK solutions made with the 20 different solvents. Large differences in ε_H and $\varepsilon_{Si\ CP}$ are observed amongst this set of solvents, with $\varepsilon_{\mathrm{Si}}$ ranging from 1 for THF and MTBE to 17 for 1,1,2,2-tetrachloroethane (TCE) and 1,2-dichloroethane. It appears that the best DNP enhancements are obtained with halogenated solvents (with the exception of 1,1,1 trichloroethane). For halogenated solvents, ε_H and $\varepsilon_{Si\ CP}$ range from 11 to 22 and from 11 to 17, respectively. The success of the halogenated solvents can probably be attributed to several factors:

1. The halogen atoms increase the molecular mass and the dipole moment of the solvent, which will generally lead to higher freezing points and lower vapor pressures.

2. The halogen atoms reduce the ^{1}H densities of the organic solvents. This allows the polarization to be concentrated over a smaller bath

Solvent	ε_H	$\varepsilon_{Si\ CP}$
dichloromethane	9	3
chloroform	15	10
1,1,2,2-tetrachloroethane	21	18
1,1,1-trichloroethane	3	3
Trans-dichloroethene	9	8
1,2-dichlorobenzene	19	16
1,2-dichloroethane	23	18
1,2-dibromoethane	11	11
1,3-dibromobutane	19	12
1,1,2,2 tetrabromoethane	12	13
hexafluoro-2-propanol	6	9
2,2,2-trifluoroethanol	5	7
para-xylene	8	13
mesitylene	6	5
isopropanol	6	7
tetrahydrofuran	4	1
methyl *ter*-butylether	3	1
dimethylformamide	3	3
dimethylsufloxide	4	4
acetonitrile	5	7

Table 4.1: Proton and silicon enhancement for **Mat-PhOH** wetted with a 10 mM solution of bTbK in different solvents

of ^{1}H nuclei. Note that this is believed to be the reason why high deuteration levels produce large ^{1}H enhancements. For example, the ^{1}H density of fully protonated tetrachloroethane is similar to that of 90/10 D_2O/H_2O.

3. The halogen atoms may play the role of a conformational anchor which will reduce or eliminate molecular motions/re-orientations (*vide infra*)

In addition to the halogenated solvents, reasonably high ε values are obtained with para-xylene. The other solvents display poor or no enhancement under the experimental conditions used in this study.

The most likely cause for the poor ε values observed for some of the solvents is the presence of residual molecular motion at 100K. Molecular motions will reduce both ^{1}H-^{1}H dipolar couplings and proton T_1, thereby diminishing the DNP enhancements. The comparison of the performance of

solvents with and without methyl groups supports this hypothesis. Rotation of methyl groups around their C_3 axis possesses a low energy of activation and methyl groups will therefore still present dynamics at temperatures under 100 K. In Table 4.1 it is clear that solvents containing only protons in methyl groups (DMSO, acetonitrile, MTBE, 1,1,1-trichloroethane) have very low proton DNP enhancements (from 2 to 4). The hypothesis that methyl protons play a negligible role in the polarization transfer is further supported by the observation that the replacement of the methyl groups in propan-2-ol by trifluoromethyl groups in 1,1,1,3,3,3-hexafluoropropan-2-ol does not affect the proton DNP enhancement. (Table 4.1). Additional evidence supporting this hypothesis is the fact that the ε_H of para-xylene (7) is higher than the one of mesitylene (5). Replacing one proton by a methyl group seems to harm DNP enhancements, probably due to shortened $T_1(^1H)$.

In addition, the low performance of some of the solvents may potentially be related to large scale residual molecular motion. At 110 K, the ^{1}H NMR spectrum of **Mat-PhOH** impregnated by tetrahydrofuran still displays the two resolved proton resonances of the solvent, which indicates the presence of molecular motion that partially averages out the dipolar coupling. At the time of this study, TCE in combination with bTbK appeared to be one of the most promising non-aqueous mixture for DNP SENS as it performed equally well as the aqueous solutions of water/TOTAPOL previously used in the litterature for DNP SENS. TCE is still used today for DNP SENS experiments for its performance in DNP and good solvation properties of many radicals. This solvent can also be used for bulk solution enhancements, even if it was observed that in combination with some radicals (such as TEKPOL), glass formation can be an issue as previously discussed.[101, 98]

Investigation of properties of solvent affecting their DNP efficiencies is still underway. Besides the proton T_1 and proton densities, many parameters have to be considered such as the Debye temperature of the radical/solvent mixture, the electronic relaxation properties or the MW penetration properties of the glass. This study[110] was however an improvement in the field, opening the field of application of DNP SENS approaches and of radicals that can be used for DNP applications.

4.2 Quantifying the sensitivity enhancement

In the previous chapter, only the enhancement (ε: defined as the ratio of the intensity (or integral) of the signal obtained while irradiating the sam-

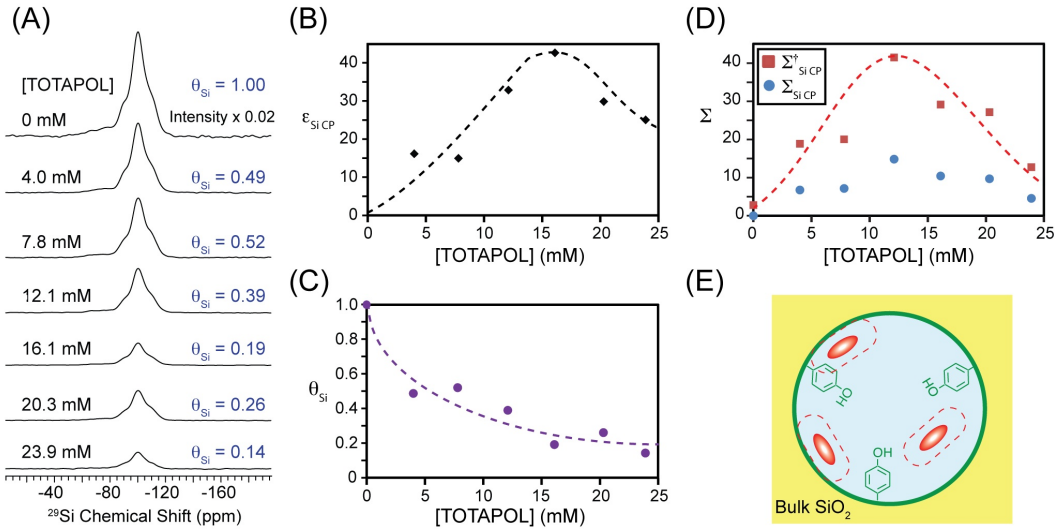

Figure 4.1: ((A) ^{29}Si CP MAS spectra of **Mat-PhOH** impregnated with TOTAPOL solutions of varying concentration. The quenching factor (θ_{Si}) is listed next to each spectrum. (B) $\varepsilon_{Si,CP}$ and (C) θ_{Si} plotted as a function of TOTAPOL concentration. (D) The overall ^{29}Si sensitivity enhancement with ($\Sigma^{\dagger}_{Si,CP}$) and without ($\Sigma_{Si,CP}$) Boltzmann enhancement. Dashed lines are added to guide the eye. (E) A schematic showing the distribution of radicals within MatPhOH. Radicals near to the surface induce quenching, reducing the magnitude of the ^{29}Si (and ^{13}C) NMR signal. Adapted from ref [2].

ple with microwaves over that without microwave irradiation, *for the same sample*) was taken into account to quantify the signal enhancement. This number quantifies the efficiency of the polarizing agent in enhancing the nuclear polarization, and was, until recently the only gauge used to evaluate the DNP efficiency. However the sample is modified by the introduction of a radical containing solution. Even if paramagnetic species can be a tremendous source of structural information, their detrimental effects on the NMR signal have been known for a long time. The introduction of exogenous radicals to polarize the sample will therefore affect the sensitivity; meaning that ε is not necessarily relevant to assess the sensitivity enhancement provided with respect to a conventional NMR experiment. In 2010, Thurber and Tycko have investigated in a qualitative study the sensitivity gains provided by DNP in frozen water/glycerol solutions at various temperatures (from 7 to 80 K) and radical concentrations. They observed that at higher radical

concentrations generally increased, while the magnitude of the absolute signal generally decreased.[57] Our main focus here is to quantify the gain in sensitivity in the application of DNP to the study of surfaces.

The quantification of the gain in sensitivity provided by 100 K DNP SENS experiments as compared to room temperature (rt) experiments was initially done by measuring the ^{29}Si CP MAS signal per unit mass of **Mat-PhOH** impregnated with TOTAPOL solutions of varying concentration.[111] The ^{29}Si CP DNP enhancement ($\varepsilon_{Si\ CP}$) was found to peak at a value of 40 for a TOTAPOL concentration of 16 mM. However, as shown in Figure 4.1 the largest absolute signal per unit mass was obtained for 12 mM TOTAPOL, for which $\varepsilon_{Si\ CP}$ was only 32.

This signal loss at increased radical concentration can be attributed to two different paramagnetic effects: (i) ^{29}Si nuclei which reside inside the diffusion barrier or near to radicals will not contribute to the observed NMR signals due to large dipolar shifts and anisotropies and fast relaxation. This will directly reduce the intensity of ^{29}Si solid-state NMR spectra. (ii) ^{1}H resonances will also be broadened/relaxed by the same paramagnetic effects, and this is expected to reduce the efficiency of ^{1}H-^{1}H spin diffusion, heteronuclear decoupling and the transfer of polarization to ^{29}Si via CP. This will indirectly lead to reduced intensity of the ^{29}Si CP MAS spectra. To quantify the detrimental effects of the paramagnets to the NMR signal, we introduced the quenching factor θ defined as follow:

$$\theta = \frac{I_{m,ON}}{\varepsilon * I_{m,REF}} \tag{4.1}$$

where $I_{m,ON}$ is the signal per unit of mass of the sample impregnated with the radical containing solution, ε the enhancement obtained for this sample and $I_{m,OFF}$ is the signal per unit of mass of the pristine material acquired in the same conditions. This factor represents the equivalent percentage of NMR active nuclei contributing to the signal. Note that all measurements of θ_{Si} were performed with a 30 s recycle delays in order to allow full longitudinal relaxation of the ^{1}H magnetization at all biradical concentrations. As expected θ decreases with the radical concentration (Figure 4.1). Note that for a 16 mM solution θ=0.2, meaning that an impressive equivalent of 80% of the sample does not participate to the NMR signal!

The presence of the paramagnetic species also affects both the longitudinal (T_1) and transverse (T_2') relaxation times of the nuclei. The effect of impregnating and freezing the material with a radical containing solution

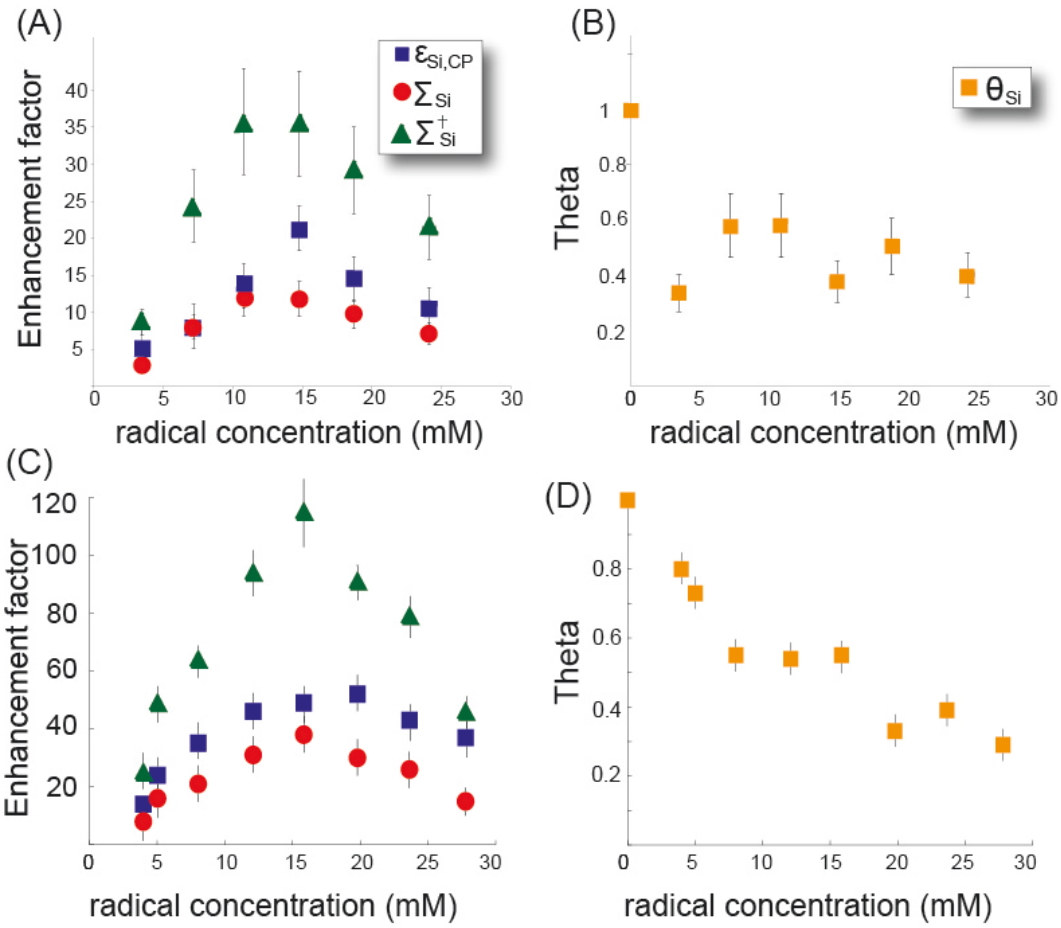

Figure 4.2: (A) (C) $\varepsilon_{Si,CP}$, $\Sigma_{Si,CP}$ and $\Sigma^{\dagger}_{Si,CP}$ and (B) (D) θ_{Si} plotted as a function of radical concentration for materials impregnated with bTbK ((A) and (B)) and bCTbK ((C) and (D)) solutions in TCE.

and freezing on the T_1 is not straightforward. On the one hand, radicals will reduce the relaxation times, and short T_1s are beneficial because the interscan delay can be reduced, therefore making in possible to accumulate more scans during a given amount of time; on the other, freezing with solvent will likely quench the motions/displace the O_2 present in the pores responsible relaxation at room temperature. For instance, at room temperature **Mat-PhOH** has a $T_1(^1H)$ of 0.8 s, which is increased to 3.9 s when the material is degassed. $T_1(^1H)$ further increases to 12.6 s when the material is impregnated with pure water and frozen at 100K.

Based on these observations, in 2011 we introduced the overall sensitivity

factor Σ given by:

$$\Sigma = \varepsilon * \theta * \sqrt{\kappa} \tag{4.2}$$

with $\kappa = \frac{T_{1,d}}{T_{DNP}}$ the ratio between $T_{1,d}$ the degazed material longitudinal relaxation time and T_{DNP} the build-up time constant in the DNP conditions (proton T_1 in the case of the CE).

Finally, to gain into account the gain in sensitivity due to the lower temperature of the experiment, we introduced $\Sigma^{\dagger}$ given by:

$$\Sigma^{\dagger} = \frac{\Theta_{rt}}{\Theta_{exp}}\Sigma_{Si} \simeq 3\Sigma \tag{4.3}$$

A maximum $\Sigma^{\dagger}$ CP of 42 was found for **Mat-PhOH** impregnated with 12 mM TOTAPOL (Figure 4.1) proving that the optimal concentration of radical yielding optimal sensitivity is not always matching that yielding the highest ε. A factor of 42 means a reduction of experimental time by a factor around 1750. Figure 4.2 shows the dependance of ε, Σ and θ for materials impregnated with solutions of bTbK and bCTbK in TCE. As expected, the same trends as TOTAPOL/water solutions can be seen here. Note that the change in line width was not taken into account here due to the negligible broadening due to the presence of the radical and to the low temperature (the samples are intrinsically disordered). For different systems, such as metal-organic frameworks (MOF)[88] this factor is detrimental to the sensitivity and has to be taken into account. Over the past three years other groups have taken up an approach similar to ours to quantify the sensitivity enhancements for various systems such as labeled polymers[85], frozen solutions (of biomolecules for instance) [112, 113, 114], recrystallized micro crystals[115] or materials [84]. It is important to realize that the optimal DNP conditions are system-dependent and that when investigating a new type of materials, reoptimization of the parameters is always wise. In particular, the type of surface (area, polarity...) affects greatly the interaction with the radical as shown in the next section.

4.3 Modification of the surface for optimal DNP SENS

The synthesis of typical surface organometallic catalysts we want to study by DNP is done in several steps summarized in Figure 4.3.[116] The material is first synthesized using a sol-gel approach. The organic linker is incorporated on the surface at this step. The surfactant is then removed an a series of

chemical reactions are performed at the surface of the material to transform the organic linker into a suitable ligand for the metal. One more step is necessary before the grafting of the metal: the so-called passivation of the surface. Indeed, after the synthesis of the material, many silanol (Si-OH) groups remain on the surface and these labile and relatively acid protons are likely to react with the metal center. A classical way to remove these reactive groups is to perform a chemical reaction and replace them with inert organic groups, typically trimethylsiliyl groups (TMS/ -Si$(CH_3)_3$).[117] As stated before, in a DNP experiment, the polarization follows a complex trajectory from the electron to the target NMR nucleus. In this process, the proton longitudinal relaxation time ($T_1(^1H)$) plays a key role. In particular, it was recognized early on that for the CE $T_1(^1H)$ usually defines the polarization build-up rate, and that in cases where $T_1(^1H)$ is short, the enhanced polarization is rapidly dissipated through relaxation before it can be accumulated and distributed throughout the sample.[118] The DNP efficiency is thus expected to diminish with short $T_1(^1H)$. It was shown for instance that, when using nanodiamonds as the polarization source, DNP efficiency decreases with the $T_1(^1H)$.[56] On the other hand, as $T_1(^1H)$ governs the polarization build-up rates, and thus the interscan delays, it has been shown that a gain in sensitivity per unit time can be attained with short T_1.[111, 112] The aim of this study is to investigated the effect of a addition of numerous fast relaxing protons on the surface (mandatory during the synthesis of materials); and to find a way to retain high enhancements while studying a passivated material.

4.3.1 Experimental procedure

The effect of the passivation on the DNP was done using a series of mesostructured hybrid organosilica materials that contain surface propylazide fragments. These samples were obtained by condensing tetraethoxyorthosilicate and 3-azidopropyltri-methoxy silane in the presence of a structure-directing agent (P123). The resulting material (**Mat-PrN$_3$**, Figure 4.4 A) contains roughly five terminating surface silanols per propyazide unit. As said before, coating the silica surface with unreactive TMS fragments allows for the subsequent selective grafting of active metal complexes; but TMS are not the only passivating agent that can be used (Figure 4.4), thus making this material an ideal scaffold for relating the properties of the surface groups to the DNP efficiency. A 16 mM solution of bCTbK in TCE was used as a polarizing mixture. DNP experiments were conducted on a commercial Bruker Avance III 400 MHz NMR spectrometer equipped with a 263 GHz gyrotron microwave source, using a 3.2 mm triple resonance MAS probe at

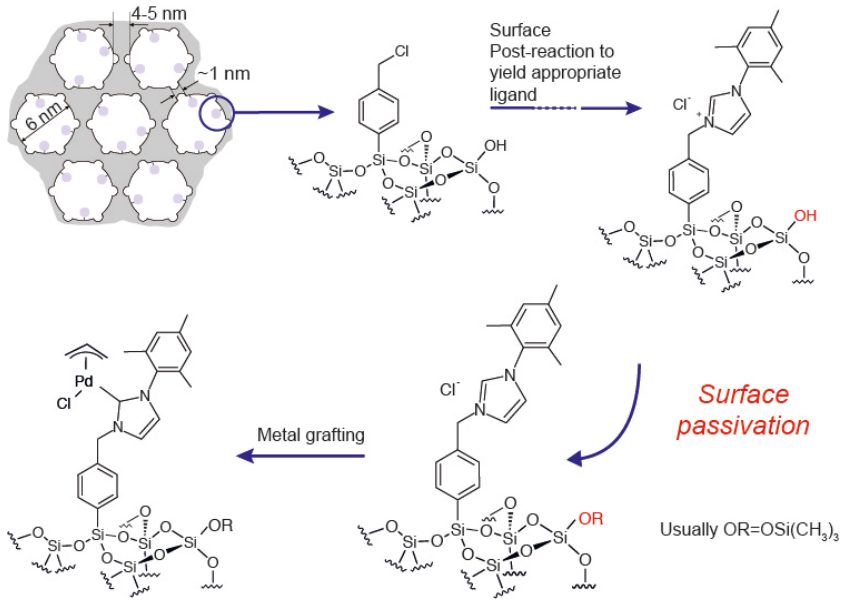

Figure 4.3: Illustration of the different synthetic steps leading to the obtention of a surface organometallic catalyst (here a palladium NHC complex). The surface passivation step is highlighted in red.

sample temperatures around 100 K.

4.3.2 Influence of the passivating group on DNP efficiency

Figure 4.4 shows the proton (ε_H: solvent) and silicon ($\varepsilon_{Si\ CP}$: surface) signal enhancement factors for the different samples. The overall sensitivity enhancement (Σ) is also shown. Table 4.2 gives the $T_1(^1H)$ of the solvent and the surface protons involved in CP. In most cases ε_H and $\varepsilon_{Si\ CP}$ match within error, as do the $T_1(^1H)$ for the bulk solvent and the surface ^{1}H nuclei. Carbon enhancements ($\varepsilon_{C\ CP}$) of the surface functional groups have also been measured and match ε_H and $\varepsilon_{Si\ CP}$. These observations are consistent with the solvent and surface protons existing within a single dipolar coupled proton spin bath where polarization is evenly distributed throughout the samples by proton–proton spin- diffusion mechanisms.

An ε_H of 116 was obtained for the unpassivated **Mat-PrN$_3$** material; this result is consistent with the values obtained in previous studies on similar materials.[101] Upon replacement of the hydroxy group with TMS groups, ε_H is decreased to 17, which correlates with a sharp decrease of the proton

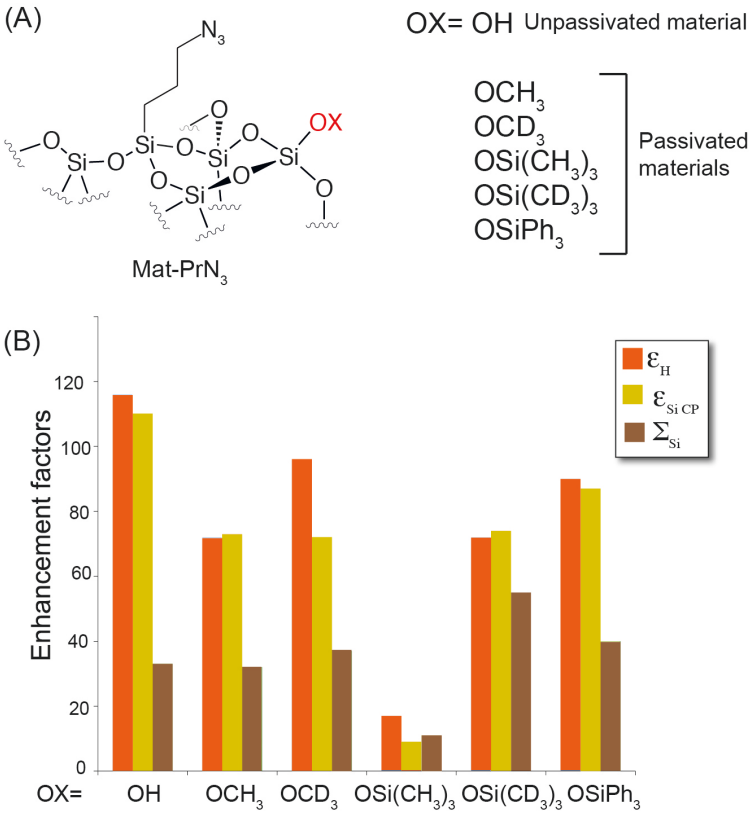

Figure 4.4: (A) Molecular structure of the materials investigated during this study. (B) Proton enhancement (ε_H), silicon enhancement ($\varepsilon_{Si\ CP}$) and overall sensitivity enhancement (Σ) as a function of the passivating groups. Taken from ref [119].

T_1 from 3 s (in the presence of hydroxy groups) to 1 s. Such short $T_1(^1H)$ values are expected in the presence of a high concentration of fast-rotating methyl groups at the temperature of the experiment here, that is, around 100 K. At significantly lower temperatures, tunneling mechanisms are expected to impact T_1.[120] Next we investigated the effect of the selective deuteration of these surface methyl groups on $T_1(^1H)$ and the DNP enhancements. Deuteration has long been used to optimize DNP enhancements. Deuteration of the solvent is widely employed, and was proposed to lead to larger DNP enhancements owing to a decrease in the size of the proton bath and an increase in $T_1(^1H)$.[99] Partial deuteration of exchangeable sites in an otherwise fully deuterated protein was also shown to improve enhancements by the same mechanism.[43, 121] In both cases, the $T_1(^1H)$ was only seen to

	OH	OCH_3	OCD_3	TMS	$[D_9]$-TMS	$OSiPh_3$
$T_1(^1H)$ [s][a]	3.03(3)	3.03(4)	3.59(4)	1.0(1)	2.81(2)	3.06(4)
$T_1(^1H)_{^{29}Si}$ [s][b]	2.40(2)	2.23(1)	2.67(2)	0.89(2)	3.15(3)	2.70(1)
$\varepsilon_{Si\ CP}$ [c]	110(3)	71(3)	72(3)	9(3)	74(3)	87(3)
$\Sigma_{Si\ CP}$ [d]	33	31	38	11	55	40

a: Proton longitudinal relaxation times measured by direct acquisition and
b: by ^{29}Si CP
c:^{29}Si enhancement measured by ^{1}H CP
d:overall ^{29}Si sensitivity enhancement.

Table 4.2: Proton longitudinal relaxation times, silicon-29 enhancements, and overall sensitivity enhancements of **Mat-PrN$_3$** with various passivating surface groups.

significantly change at high deuteration levels.

When protonated TMS is replaced by [D9]-TMS, $T_1(^1H)$ increases to 3 s and consequently $\varepsilon_{Si\ CP}$ rises from 9 to 73. Less- pronounced effects were observed when the surface was passivated with methoxy and [D3]-methoxy groups (Figure 4.4). $T_1(^1H)$ did not substantially increase when the methoxy groups were deuterated. Consistent with this observation no major difference in $\varepsilon_{Si\ CP}$ was observed. Methoxy groups likely have a smaller influence on $T_1(^1H)$ and $\varepsilon_{Si\ CP}$ than TMS groups owing to their lower proton densities.

The drastic increase of ε upon deuteration of TMS groups is clearly attributable to changes in the relaxation properties of the sample, rather than changes in the size of the proton spin bath, as is the case when using partially deuterated solvent. Indeed, when the TMS groups were replaced by protonated TPS the enhancement was restored (Figure 4.4 (C)). Materials passivated with TMS and TPS both have a similar overall proton density, with the primary difference being the longer $T_1(^1H)$ for the TPS passivated material (proton density is only affected very locally by the use of different passivating groups).

The detrimental impact of surface methyl groups on ε at 100 K was also confirmed by DNP NMR experiments conducted on a material containing

imidazolium mesityl moieties (**Mat-Im**) in place of the propylazide groups. **Mat-Im** materials contain three methyl groups on a mesityl ring in the organic fragment. For unpassivated **Mat-Im**, the ε_H and surface $T_1(^1H)$ were 40 and 1.7 s, respectively, as compared to 116 and 2.5 s for the unpassivated **Mat-PrN$_3$** material. As subtly implied in the previous chapter, the electron relaxation times might have an effect on the DNP enhancements. They were measured for all the passivated samples and no significant change was observed between samples suggesting that the difference of performance is indeed correlated to the proton T_1 of the passivating group.[119]

4.3.3 Interaction between the radical and surfaces

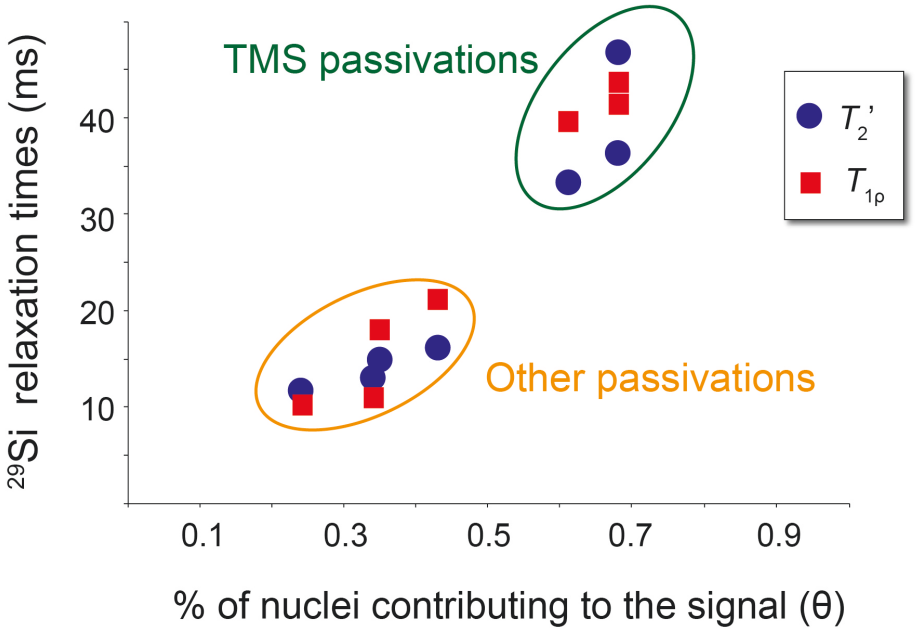

Figure 4.5: ^{29}Si rotating-frame relaxation times ($T_{1\rho}(^{29}Si)$) and effective transverse dephasing times ($T_2'(^{29}Si)$) plotted as a function of the quenching factor (θ_{Si}) for the various materials in a 16 mM solution of bCTbK in TCE solution. $T_{1\rho}(^{29}Si)$ was measured with a 26 kHz spin-lock radio-frequency field. Taken from ref [119].

If we now turn our attention to the overall NMR sensitivity enhancement Σ introduced in the previous section, we note that the ratio Σ/ε is significantly higher for both TMS and [D9]-TMS than for the other passivating groups.

This finding is related to the fact that the decrease in the NMR signals as a result of paramagnetic effects is less pronounced in the presence of these passivating groups. This in turn suggests that these bulky groups prevent the close approach of the paramagnetic polarizing agents and the surface. Figure 4.5 shows the ^{29}Si rotating-frame relaxation times $T_{1\rho}(^{29}Si)$ and the effective transverse dephasing times $T_2'(^{29}Si)$ as a function of the measured ^{29}Si quenching factor θ_{Si} (the apparent fraction of nuclei contributing to the signal). Both the relaxation times and θ_{Si} are expected to diminish when the surface and the radical are in close proximity. For materials passivated with TMS and [D9]-TMS groups, θ_{Si} is high (> 0.6) and both $T_{1\rho}(^{29}Si)$ and $T_2'(^{29}Si)$ are relatively long (> 30 ms). Conversely, all other passivating groups lead to strong quenching effects (with θ_{Si} values between 0.2 and 0.4, that is, similar to values previously observed for mesoporous materials) and short silicon relaxation times (between 11 and 20 ms). A strong correlation is observed between θ_{Si} and the two relaxation times, thus indicating that the short $T_{1\rho}(^{29}Si)$ and $T_2'(^{29}Si)$ values observed for passivating groups other than TMS are due to proximity between the surface and the radical. We note that a doubling in θ_{Si} leads to a factor 2 gain in overall sensitivity. Finally, $T_2'(^{29}Si)$ was measured for the differently passivated **Mat- PrN$_3$** samples wetted with pure solvent (i.e., no biradical). In all cases, $T_2'(^{29}Si)$ was longer than 200 ms, thus confirming that the differences observed in the silicon relaxation times are indeed due to paramagnetic effects rather than to the nature of the individual passivating groups. The shortening of these relaxation times is detrimental to many NMR experiments; with a short $T_{1\rho}$ CP will be less efficient, and a short T_2' will reduce the efficiency of any experiment containing a spin-echo block. A simple solution to increase $T_2'(^{29}Si)$ would be to lower the radical concentration. However, as ε and Σ are highly dependent on the radical concentration, reducing the radical concentration would also diminish sensitivity enhancements. For challenging NMR experiments, in which sensitivity is an issue, both high enhancements and long transverse relaxation times are required. In many cases, lowering the radical concentration to obtain a $T_2'(^{29}Si)$ that is long enough for these NMR experiments would lower the enhancements to the extent that sensitivity would be too low to perform such experiments. Passivation of the surface with bulky apolar groups, such as TMS, is a way to obtain high enhancements, lessen signal quenching by the radical, and maintain long T_2' values.

4.3.4 Interaction between the radicals and the surface

DNP performance of the new radicals introduced in chapter 3 on materials was investigated by impregnating non passivated **Mat-PrN$_3$** with 16 mM

compound	$\varepsilon_{C\ CP}$ (bulk)	$\varepsilon_{Si\ CP}$ (material)	θ_{Si}	Σ_{Si}	$T_2'(^{29}Si)$ (ms)
bTbK, 1	47	60	0.2	16	13
$(CT)_2$bK, 3	53	80	0.2	25	5
bCTbK, 4	80	103	0.2	35	14
$(ACT)_2$bK, 5	42	32	0.6	13	29
bPyTbK, 6	115	10	0.4	10	20
TEKPOL, 7	200	214	0.2	53	7

a: ^{13}C enhancement measured on a bulk 16 mM TCE solution.
b: ^{29}Si enhancement measured on **Mat-PrNH$_3$** impregnated with a 16 mM TCE solution.
c: ^{29}Si quenching factor.
d: ^{29}Si overall sensitivity enhancement.
e: ^{29}Si transverse dephasing time.

Table 4.3: Bulk Solvent and Silicon Surface Enhancements, Quenching Factors, Overall Sensitivity Enhancements and Silicon Transverse Dephasing Times for 1 and 3-7

radical solution in TCE. The results are summarized in Table 4.3. Along with ε, the quenching factor θ and the overall silicon enhancements Σ are reported. For most of the radicals, ε increases in the materials as compared to the bulk solution, consistent with previous observations and with the cryoprotecting role of the material.[101] There are two notable exceptions: 5 and 6, where ε drops from 42 to 32 and from 115 to 10, respectively. This can potentially be attributed to the differences in polarity among the radicals that causes them to interact differently with the surface, as observed previously with the difference passivation of the surface. Wessig *et al.* showed by EPR that matching the polarity of the solvent and the surface minimizes radical-surface interactions.[122] This hypothesis is supported here by the measure of the $T_2'(^{29}Si)$. For the other radicals $T_2'(^{29}Si)$ is shorter than 14 ms, but it increases to 20 ms for 6 and to 29 ms for 5, indicating that in these cases the radical is further away from the surface, for example, through a partial exclusion from the pores thereby explaining the reduction in DNP efficiency. The quenching

factor is also higher for this two radicals supporting the hypothesis of lesser interactions with the surface.

4.4 Are big radicals compatibles with small pores?

With the introduction of the bTbK derivatives of increasing performances, but also increasing size, as well as the increasingly bulky functionnalization of the surface, the question arises of the penetration of these radicals inside the mesopores. We thus performed comparative study of the model material **Mat-PrIm,TMS** (Figure 5.5) impregnated with 32 mM electron concentration solutions of TEMPO, bTbK, bCTbK and TEKPOL2 in TCE. Measurement of the T_1 build-up curves for the solvent yielded data that could not be fitted properly with a mono-exponential function. The fit could be improved using stretched exponential functions:

$$I = I_0(1 - exp(-(t/T_1^*)^\beta) \tag{4.4}$$

This type of behavior has previously been observed for systems where the distribution of radicals is not homogenous (see Chapter 6). MW Off build up curves were also measured, and were found to be significantly different than the MW On ones. ε was therefore observed to depend on the recycle delay τ, which we already observed for microcrystals coated with radical containing solutions (ref [123] and Chapter 6), therefore indicating various environments for the radicals.The profile of ε as a function of the recycle delay τ is given in Figure 4.6. TEKPOL2 presents a different behavior than the other three radicals, indicating different distribution of the radical in the pores. The quenching factor θ has been measured for all the radicals and results are displayed in Figure 4.6. θ is four times bigger for TEKPOL2 than for the other radicals, indicating less affinity with the pore of the material. Partial exclusion from the pores while still retaining high enhancements would be beneficial for the NMR sensitivity since proximity of the radical induces signal losses and shortened relaxation times. Further tests and simulations are currently being run to explain this phenomenon.

In conclusion, many parameters were investigated to optimize the sample preparation. This leads to high sensitivity enhancement factors (up to 200) of the materials, which made it possible to apply this technique to probe the structure of many complex systems over the past three years. Selected applications are presented in the next chapter.

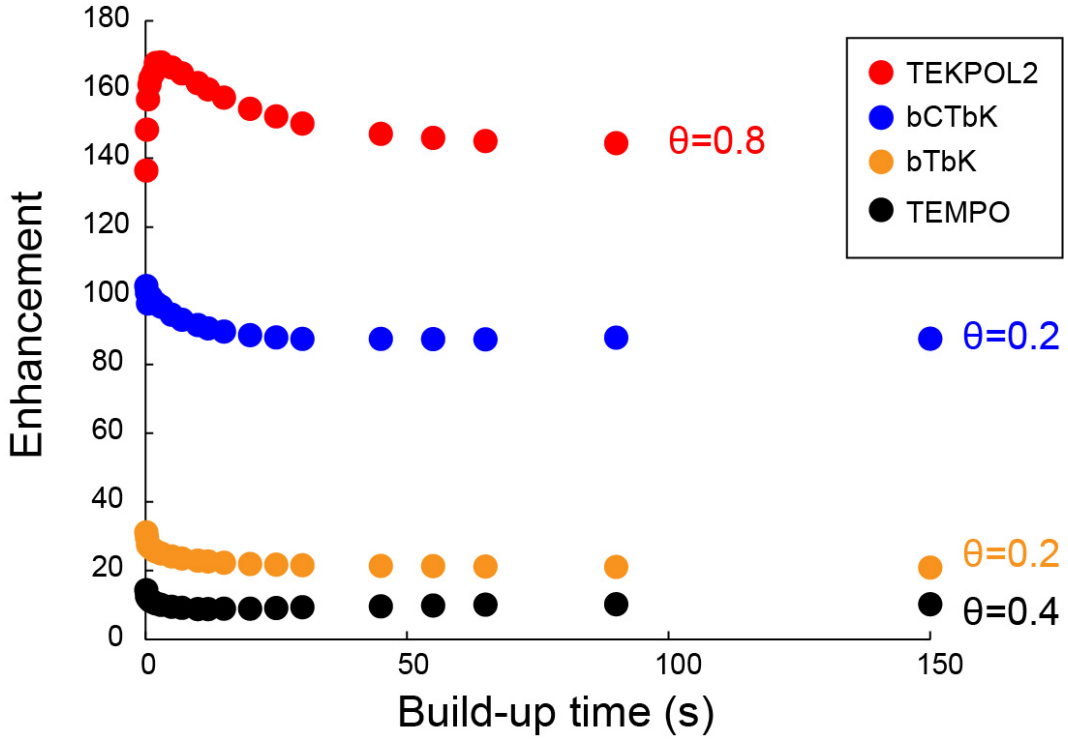

Figure 4.6: Enhancement as a function of the build-up time for **MatPrIm,TMS** impregnated with 32 mM electron concentration solutions of TEMPO (black), bTbK (orange), bCTbK (blue) and TEKPOL2 (red). The signal was measured using a saturation-recovery CP pulse sequence. The quenching factor θ is displayed next to the curves.

Chapter 5

Applications to functionalized materials.

This Chapter reports various applications of DNP SENS to materials in which I was involved over the past three years. The method was improved over this period of time, so the applications go from basic structural investigation to the implementation of more challenging NMR experiments. Application to materials that include the characterization of Periodic Mesoporous Organosilicas (PMO) or luminescent yttrium complex grafted on silica nanoparticles are not reported here can be found in ref. [110, 124]

5.1 Metal Organic Framework

Metal–organic frameworks (MOF) constitute an important class of crystalline porous materials.[125, 126, 127] Since the introduction of the first porous MOF more than twenty years ago,[128] more than 2000 three-dimensional MOF topologies have been described. The large surface areas (up to 6000 m2 $g.^{-1}$) and tunable pore sizes (ranging from 0.5 to 3 nm) of MOFs makes them well suited for a variety of applications including gas storage, molecular sieving, or heterogeneous catalysis.[129] Many MOF materials have been shown to be efficient and selective catalysts in a wide variety of key chemical reactions. As for other classes of solid catalysts, establishing structure-activity relationships is key for the rational design of MOFs with improved catalytic properties. Of course, when mono crystals can be grown, XRD is the method of choice for the structural investigation of MOFs. However, when the MOF is partially functionalized, XRD becomes unable to resolve the structure. Solid-state NMR is well suited to characterize the molecular structure and dynamics of MOF materials,[130] but when the sensitivity is

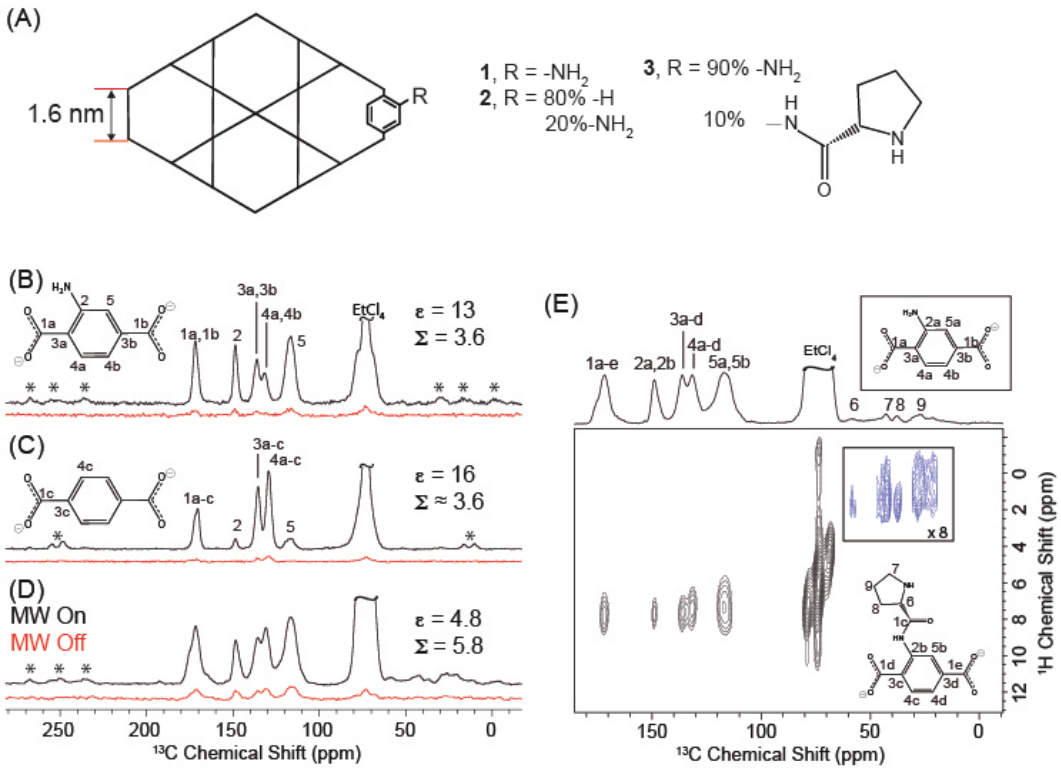

Figure 5.1: (A) Schematic structures of the three N-functionalized MOFs which are isostructural to MIL-68. All these MOFs display one-dimensional rod-shaped structures, composed by hexahedral and triangular channels with an aperture of 1.6 and 0.6 nm, respectively. (B-D) One-dimensional ^{1}H-^{13}C CP MAS spectra of 1, 2 and 3, respectively, recorded with (black) or without microwave irradiation (red) to induce DNP. The samples were impregnated with a 16 mM bTbK TCE solution. Both the observed (ε) and overall signal enhancement factors (Σ) provided by the DNP experiment are listed. DNP enhancement factors for the solvent resonance (ε_S) are also provided. Spinning sidebands are marked with asterisks. (E) Two-dimensional ^{1}H-^{13}C HETCOR spectrum of 3 (acquired in 10.6 h total experiment time). Adapted from ref [88].

too low to do so, the usual method to characterize the systems becomes to "digest" the system in acid and run liquid state NMR on the resulting solution, preventing the study of the pristine material. The aim of this study was to determine the applicability of DNP experiments to the structural determination of MOFs, illustrated here on 3 MOFs: a N-functionalized MOF

compound (In)-MIL-68-NH **(1)**, on a partially functionalized variant of 1 with a terephthalate:aminoterephthalate ratio of 80 :20 **(2)**, and on a 10 % proline-functionalized derivative of **1** (In)-MIL-68-NH-Pro **(1)** (Figure 5.1). These three materials are representatives of an as-synthesized functionalized MOF (compound **1**), a partially functionalized MOF (also called MIXMOF, compound **2**), and of a post- synthetically modified MOF (compound **3**).

Figure 5.1 (B),(C) and (D) shows the one-dimensional ^{1}H-^{13}C CP MAS spectra recorded on the three MOF samples with or without microwave (MW) irradiation. The observed DNP enhancement (ε) and the overall sensitivity enhancement factors (Σ) are indicated for each of the three compounds. As the MOF samples investigated ere could not be impregnated with an aqueous solution (due to a chemical reaction with water), solutions of bTbK in TCE were utilized. Incipient wetness impregnation was used to impregnate the dry materials with a minimal amount of radical containing solution. In particular the influence of radical concentration, spinning frequency (ν_{rot}), and the amount of time the impregnated samples were allowed to rest before solid-state NMR experiments were optimized on **1**.[88] It was found that 16 mM bTbK solutions provided both the highest ε and Σ. Although ε was observed to be higher with a sample spinning frequency ν_{rot} of 8 kHz, the absolute signal of the spectra was similar with a ν_{rot} of 12 kHz. In order to reduce overlap of spinning sidebands with isotropic resonances, a ν_{rot} of 12 kHz was employed for all subsequent experiments. Finally, DNP ^{1}H-^{13}C CP MAS solid-state NMR spectra of the same sample of **1** impregnated with a 16 mm bTbK solution were periodically acquired after the sample was allowed to rest on the bench top inside the rotor for times of 5 min, 1 h and 25 h in between acquisitions. Both ε and Σ were observed to steadily increase from 7 to 13 and 3.0 to 3.6, respectively, with longer sample resting times. This suggests the biradical species slowly diffuse through the relatively small (1.6 nm) pores of the material. Spectra of 1 and 2 were recorded after 25 and 0.5 h of resting time, respectively. For compound 3, however, the enhancement factors were independent of sample resting time and spectra were recorded 5 min after rotor packing. Note that the enhancements for the TCE resonance ($\varepsilon_S > 20$ in all cases) is always larger than that for the MOF materials, suggesting that the biradical molecules are partly excluded from the pores for all three types of the materials.

Under these optimal experimental conditions, for MOF samples **1** and **2**, ε values of 13 and 16 were observed, respectively. Significantly lower values of Σ were measured, corresponding to the fact that the biradicals inside of the material cause a reduction in the signal intensity through various para-

magnetic effects. On the other hand, for 3, similar values of ε and Σ are observed (4.8 and 5.8, respectively). This strongly suggests that the bTbK molecules are excluded from the pores of **3**, leading to a low value for ε, and a relatively high value for Σ. This suggests that the whole material is contributing to the NMR signal under DNP conditions. This is in agreement with the fact that for 3, ε does not increase with additional sample resting times, and that a much larger value of ε is observed for the solvent resonances ($\varepsilon_S = 26$). It is likely that for **3**, the proline groups block the one-dimensional pores of the material and hinder the relatively large bTbK radical from diffusing into the material. TEM images of the as prepared **3** reveal that the average crystal size is less than 300 nm. Griffin and coworkers have previously applied DNP to needle-like nano- crystalline peptides which possessed an average crystal width of 150 nm.[79] In their system it was not possible for the radical to enter the lattice of the crystal and larger ε values were obtained for the solvent resonances than the resonances of nuclei inside the crystals, as observed here. In a similar way, we postulate that for **3**, the bTbK molecules reside on or near the surface of the crystallites, and that the enhanced polarization is distributed into the crystal by spin diffusion.

For all three samples, we estimate that the overall sensitivity gain with respect to a dry sample at room temperature is between 10 and 30, corresponding to a reduction in experimental time by a factor between 100 and 900. This allows high quality one-dimensional ^{13}C CP MAS spectra of **1**-**3** to be acquired in less than 5 min at natural isotopic abundance. For comparison, a ^{1}H-^{13}C CP MAS spectrum of **1** at room temperature with a similar signal-to-noise ratio has been recorded in 2.3 h using standard instrumentation. However, it should be noted that the full width at half height (Λ) of the ^{13}C resonances of all DNP solid-state NMR spectra of **1** are around 2.8 ppm, while at room temperature Λ is 1.2 ppm and is typical of a crystalline MOF. The increase in Λ primarily originates from the low sample temperatures and inclusion of the solvent in the pores of the material. Therefore, the DNP and Boltzmann signal enhancements are slightly offset by increases in Λ. Despite the slightly broader peaks, the DNP ^{13}C solid-state NMR spectra can readily be used to obtain structural information about the materials.

Assignment of the carbon resonances is reported in Figure 5.1, based on the chemical shift values and on comparison of the various spectra. Notably, the resonances corresponding to carbons 2 and 5 of the aminoterephthalate are clearly identified based on the fact that their intensity is reduced in Figure 5.1 (C), as only 20% of the linkers contained an amine moiety in **2**. The spectra of **3** are consistent with the replacement of 10 % of the amine func-

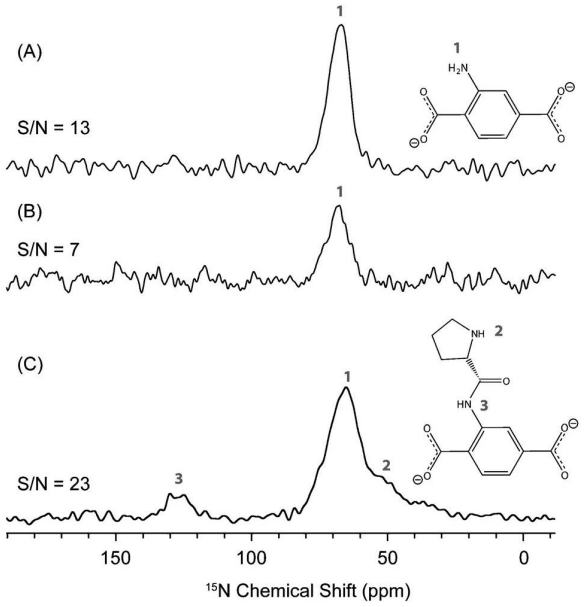

Figure 5.2: DNP ^{1}H-^{15}N CP MAS spectra of 1–3. All spectra were acquired with ν_{rot} = 12 kHz and a 2.0 ms contact time of (A) 1 (34 min total experiment time), (B) 2, (2.3 h total experiment time), and (C) 3 (5 h total experiment time). The signal-to-noise (S/N) ratios of the largest peaks are listed to the left of each spectrum. Chemical shifts are referenced to the NH_4^+ resonance of ammonium nitrate. Taken from ref [88].

tionalities with proline ligands. In the aliphatic region of the 1D ^{13}C CP MAS spectrum, the resonances from the carbon nuclei of proline are hardly visible and overlap with the spinning sidebands of the aromatic resonances. The corresponding correlations are, however, unambiguously observed in the 2D dipolar ^{1}H-^{13}C HETCOR spectrum (Figure 5.1 (E)). With the signal enhancement afforded by low temperature DNP experiments the 2D HETCOR spectrum could be acquired in 10.6 h. Note that without DNP, the acquisition of a such a spectrum with high enough signal-to-noise ratio to observe the weak proline resonances would require experiment times on the order of weeks. It should also be noted that it was possible to acquire a 2D ^{1}H-^{13}C HETCOR spectrum of **1** in 22 min.

DNP-enhanced ^{1}H-^{15}N CP MAS solid-state NMR spectra of **1**-**3** are shown in Figure 5.2. Natural abundance ^{15}N solid- state NMR experiments represent a considerable challenge due to the low gyromagnetic ratio and low

natural abundance (N.A. = 0.37 %) of ^{15}N. The ^{15}N CP MAS spectrum of 1 shows a single broad resonance at a chemical shift of 66ppm, consistent with a neutral primary amine bound to an aromatic carbon (an aniline). The ^{15}N CP MAS spectrum of **2** required a longer experimental time (2.3 h) to attain a reasonable S/N, due to the reduction in the number of ^{15}N spins by a factor of 80 % in comparison to **1**. As expected, the ^{15}N resonance of **2** has a similar chemical shift as for **1**. The spectrum of **3** (recorded in 5 h) shows the presence of two additional ^{15}N resonances consistent with the incorporation of proline into the MOF material. The proline amine resonance is observed as a shoulder (δ=50ppm) on the side of the aniline resonance while the amide resonance is centered at δ = 127 ppm. While the standard method used to characterize N-functionalized MOFs typically consists in the entire digestion/dissolution of the solids into strongly acidic solutions to enable solution NMR and mass spectrometry experiments, the strategy proposed here allows for the rapid characterization of intact MOF topologies. As such, DNP-enhanced solid-state NMR spectroscopy is expected to be applicable for the widespread characterization of MOFs. Recent applications of DNP to the study of MOFs shows well the potential of DNP for this kind of investigation.[131]

5.2 Well-Defined Surface Organometallic Catalysts

5.2.1 Monitoring Surface Functionalization

In this part, we investigate the stepwise chemical transformation and the formation of imidazolium containing materials (**Mat-PrIm**), which can be used as permanently immobilized "ionic liquids"[132, 133, 134, 135] or as precursors to N-heterocyclic carbenes[116, 136] an important class of ligands for stable single-site catalysts (Figure 5.3 (A)). Here, the imidazolium unit was introduced by a stepwise postfunctionalization of **Mat-PrN$_3$** prepared by a direct synthesis approach.[136] This allows the formation of high-surface area mesostructured materials as evidenced by TEM and N_2 adsorption experiments as well as the controlled site distribution of surface functionalities.[101] Moreover, the nonpolar nature of azido group enables one to access a broad range of concentrations, including high concentrations, and makes it possible to prepare a variety of materials via postfunctionalization or click chemistry.[137] To monitor these synthetic postfunctionalization steps at the surface of materials with conventional room-temperature solid-state NMR would be prohibitively time-consuming (experiments typically

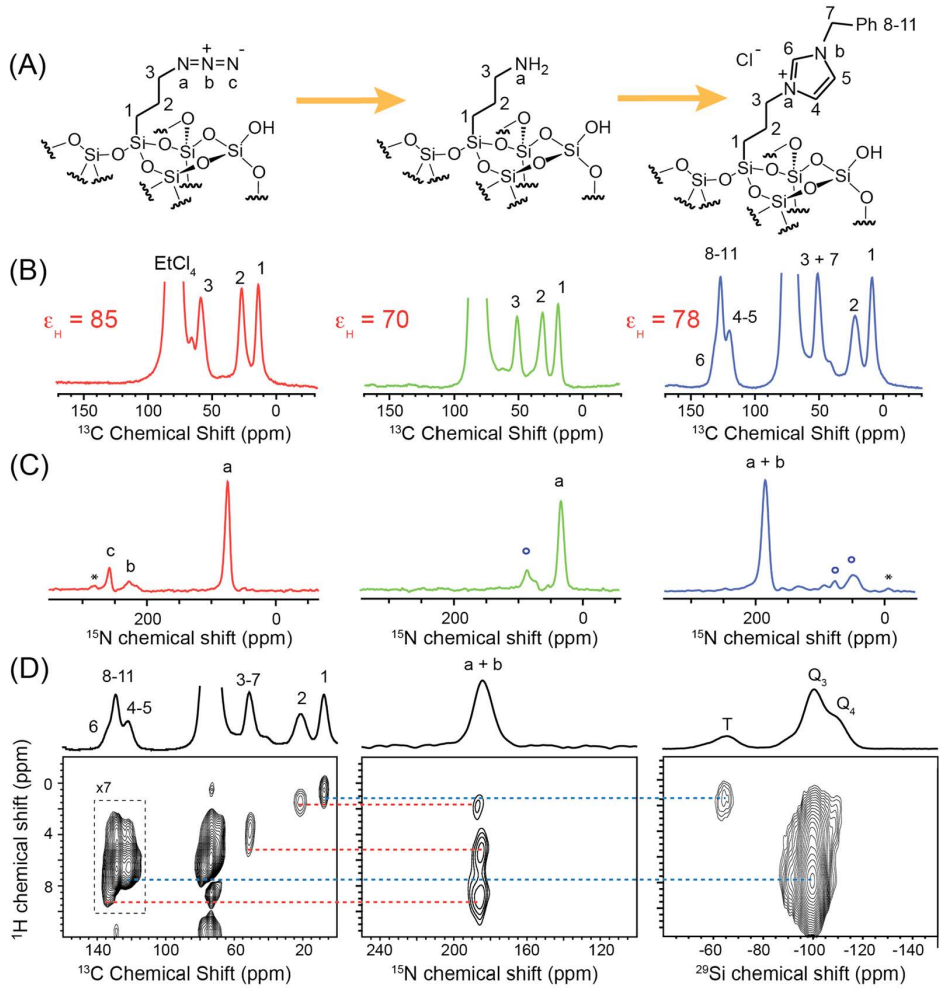

Figure 5.3: (A) Structure,(B) ^{13}C(C) ^{15}N DNP SENS CP MAS spectra of materials **Mat-PrN$_3$**, **Mat-PrNH$_2$** ,and **Mat-PrIm**.(D) ^{1}H-^{13}C, ^{1}H-^{15}N, ^{1}H-^{29}Si DNP SENS two-dimensional HETCOR spectra of **Mat-PrIm**. The open circles indicate byproducts or incomplete conversion from the previous synthetic steps. 1D and 2D ^{15}N DNP SENS spectra were acquired with total experiment times of 14 h. Take from ref [2].

take between 12 and 24 h for a one-dimensional ^{13}C CP MAS spectra). In particular, acquisition of 2D correlation spectra or ^{15}N spectra at natural isotopic abundance is not conceivable even when they would be necessary for unambiguous assignment.

Here, DNP SENS provides a means of routine characterization, by enabling the expeditious acquisition of ^{13}C, ^{15}N and ^{29}Si 1D and 2D solid-state NMR spectra at natural isotopic abundances. For example, using bCTbK as a polarizing agent, high-quality 1D ^{1}H- ^{13}C CP MAS spectra (10 min, Figure 5.3 (B)) and a 2D ^{1}H- ^{13}C correlation spectra (3.5 h, Figure 5.3 (D)) could be acquired and allow for the complete characterization of the carbon skeletons. The surface functionalities were also identified with ^{1}H- ^{15}N CP MAS spectra (14 h each, Figure 5.3 (C)). These high-quality ^{15}N CP MAS spectra even allow for minor reaction byproducts to be observed. Note that spectra with a signal-to-noise ratio of 20, high enough for routine characterization, can be acquired in 40 min. A 2D ^{1}H- ^{15}N correlation spectrum of **Mat-PrIm** was also acquired overnight (14 h, Figure 5.3). None of these would have been possible without the gain in sensitivity provided by DNP SENS. These results are all the more impressive considering that, as previously stated, ^{15}N is an extremely unreceptive NMR nucleus.

The interpretation and assignment of the DNP enhanced solid-state NMR spectra are now discussed in detail. The ^{13}C CP MAS spectra of **Mat-PrN$_3$** display three carbon resonances with chemical shifts of 8.1, 21.1, and 53.0 ppm, as expected from its proposed structure. They correlate with protons whose chemical shifts are 1.1, 2.15, and 3.2 ppm, respectively, which is coherent with a propylazide moiety. The ^{15}N spectra of **Mat-PrN$_3$** displays three resonances at 73.7, 219.5, and 248.5 ppm, confirming the presence of the azide group (Figure Figure 5.3 (C)). Upon conversion to **Mat-PrNH$_2$** with the Staudinger reaction, the ^{13}C resonance of C_3 is shifted from 53.0 to 41.5 ppm, consistent with conversion of the azide group into an amine. The nitrogen spectrum now displays one main resonance at 34.3 ppm, characteristic of the NH_2 group (Figure Figure 5.3 (C)). The byproducts observed on the ^{15}N spectrum at 89 ppm are attributed to a small amount of unconverted starting azide units (ca. 10%). One interpretation for the incomplete conversion is the inaccessibility of some of these organic fragments on the surface. The ^{13}C spectrum of **Mat-PrIm** displays resonances with chemical shifts characteristic of aromatic groups (129.2 ppm ^{13}C/6.8 ppm ^{1}H) and (122.1 ppm ^{13}C/6.8 ppm ^{1}H), as well as the three expected aliphatic resonances (Figures 5.3 (B) and 5.3 (D)). The ^{15}N spectrum confirms the presence of imidazolium nitrogen atoms with the most intense resonance centered at 185 ppm (the two nitrogen resonances being not resolved, Figure 5.3 (C)).
The complete and detailed characterization of **Mat-PrIm** was further obtained by the acquisition of a 2D ^{1}H-^{15}N correlation spectrum (Figure 5.3 (D)), which shows three resolved cross peaks, all consistent with the structure of **Mat-PrIm**. The cross peak at (185.6 ppm ^{15}N/8.9 ppm ^{1}H) corresponds

to a correlation between the nitrogens and aromatic protons, notably the C6-H proton. A shoulder at (131.1 ppm ^{13}C/8.9 ppm ^{1}H) can be discerned in the ^{1}H- ^{13}C HETCOR spectra corresponding to a correlation between C_6 and this proton. The cross peak at (185.3 ppm ^{15}N/5.4 ppm ^{1}H) corresponds to the correlations between N_a" and N_b" and the CH_2 protons of C_3" and C_7. The peak at (187.2 ppm ^{15}/1.9 ppm^{1}H) indicates the correlation between the protons of C_2" and N_a", which is the only nitrogen close enough for magnetization transfer with this CP contact time (1 ms). The ^{15}N chemical shift for this cross peak is slightly different from those of the previous two, confirming the presence of two distinct imidazolium nitrogens in the molecule. This analysis is confirmed by the lower intensity of this peak as compared to the other two, indicating a longer distance from the protons correlating with the other nitrogen, once again compatible with the molecular structure of **Mat-PrIm**. The conformation of the organic moieties with respect to the surface is also important to help understand the folding of functionalities and the derived properties. A 2D ^{1}H-^{29}Si correlation spectrum of **Mat-PrIm** could be acquired in 10 min. The cross peak at (-64.7 ppm 29Si/1.2 ppm 1H) shows the expected correlations between the T site silicon atoms (silicon bonded to the carbon of the organic moiety) and the aliphatic protons of carbon C1" and C2". The cross peak at (-99.8 ppm 29Si/7.6 ppm ^{1}H) shows a correlation between the Q sites silicon atoms and the aromatic protons. This correlation indicates that the imidazolium ring is in close proximity to the surface of the material and that the tether folds to maximize the interaction between the aromatic groups and the surface functionalities.[81, 82]

5.2.2 Full Characterization of a New Pd Catalyst

Following this study, we naturally turned our attention to a metal functionnalized material, with the study of a palladium-NHC complex (**Mat-Pd**, Figure 5.4 (A)), an efficient precatalyst for the Z-selective semihydrogenation of alkynes.[138] The material was passivated with deuterated TMS for the reasons developed in chapter IV and a 16 mM solution of bCTbK in TCE was used as a polarizing solution. However, the enhancements obtained on the material remained quite low (20), probably due to the presence of residual KHMDS (Figure 5.4 (A)), a base used to deprotonate the imidazolium ring during the synthesis. KHMDS posses 6 methyl groups, with short T_1, therefore harming the DNP enhancements. KHMDS can be clearly identified on the ^{13}C and ^{29}Si 1D spectra and 2D spectra ([-15 ppm ^{29}Si/0 ppm ^{1}H] and [0 ppm ^{13}C/0 ppm ^{1}H]), and the correlation spectra seem to indicate that the KHMDS is in an isolated environment. Complete assignment of the ^{1}H, ^{13}C and ^{29}Si resonance compatible with the proposed molecular struc-

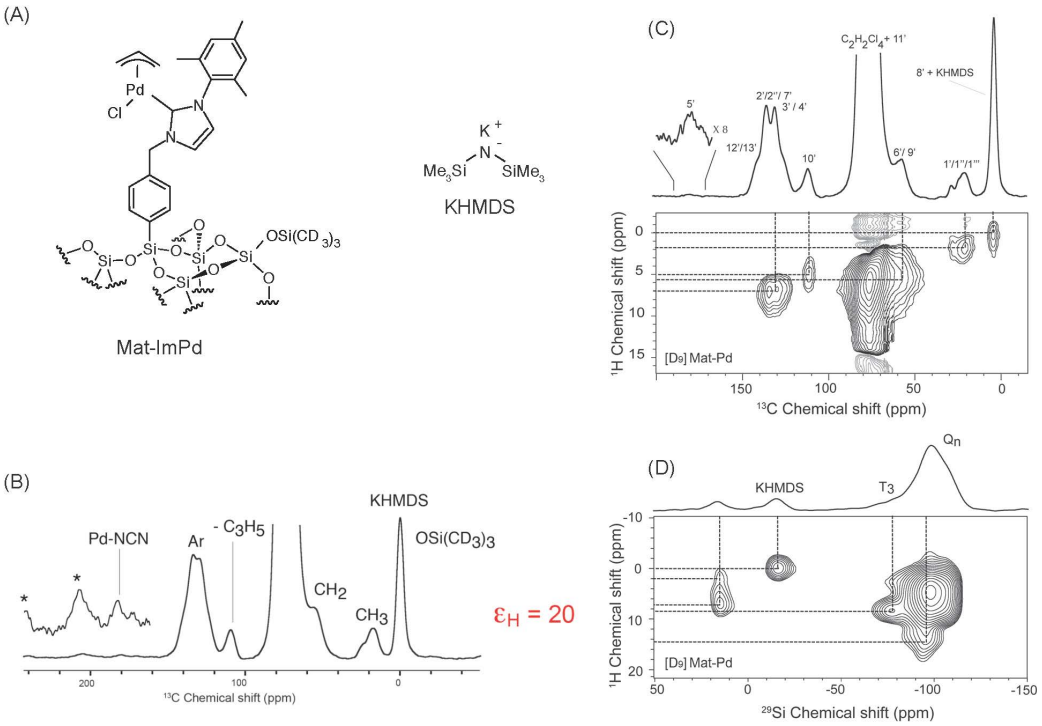

Figure 5.4: (A) Structure, (B) ^{13}C DNP SENS CP MAS spectra (C) ^{1}H-^{13}C and (D) ^{1}H-^{29}Si DNP SENS two-dimensional HETCOR spectra of **Mat-Pd**. Leftover of KHMDS (structure given in (A)) can be clearly identified on the NMR spectra.

ture were possible, but will be spared to the reader here. The interested reader can find the complete reasoning leading to the attribution in ref [138]. Note that the low enhancements were sufficient to observe the carbene center (carbon bound to the palladium) within 35 minutes, when such experiments usually require partial labeling of the sample and over a day of acquisition using rt NMR.[136] As previously observed on similar materials, the ^{1}H-^{29}Si HETCOR spectra indicate proximities between the Pd-allyl protons and the carbons of surface trimethylsilyl groups. Lelli *et al.* demonstrated that these interactions can be linked to the activity of the catalysts.[82] The higher enhancements provided by bulkier radicals, as well as the optimization of the sample preparation made it possible to use NMR to try and measure distance constraints in view of determining quantitatively the conformation of the catalyst with respect to the surface, detailed in the next section.

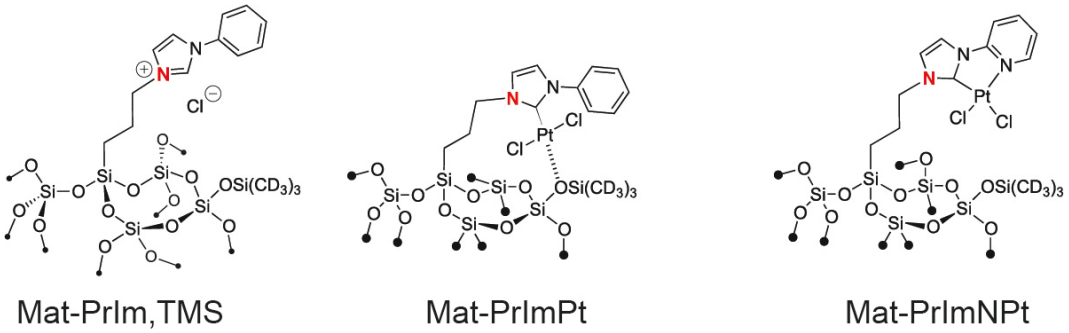

Figure 5.5: Molecular structure of **Mat-PrIm,TMS**, **Mat-PrImPt** and **Mat-PrImNPt**. The labelled nitrogen is marked in red on the structures.

5.3 Surface Conformation.

As previously stated, the conformation of heterogeneous catalysts with respect to the surface is of great importance for their catalytic activity; and therefore the knowledge of these conformations is essential for the rational design of efficient materials. Solid-state NMR is a technique that allows the direct experiments measurement of distance constraints (atom-atom distances, dihedral angles for instance). As shown by Lelli *et al.* DNP SENS applied on catalysts precursor allow the qualitative determination of surface interaction, which can eventually be linked to the activity of the catalyst[82]. We propose to investigate the detailed structure of a Pt catalyst **Mat-PrImPt**, and of a slightly modified compound **Mat-PrImNPt** (Figure 5.5) which should present different interaction with the surface. In order to probe the proximity of the organic moiety to the surface, ^{1}H-^{13}C and ^{1}H-^{29}Si Lee-Goldburg CP (LGCP) build-up curves are used.[139] If the organic moiety folds on the surface, proximities between the aromatic protons and the silicon Q sites are expected. Interaction with the TMS silicon provides another source of structural information. Figure 5.6 (A) shows the 2D LGCP-HETCOR pulse sequence, as well as an example of ^{1}H-^{13}C and ^{1}H-^{29}Si LGCP-HECTOR on the precursor of this catalyst, **Mat-PrIm,TMS**. Note that the resolution in the proton dimension is sufficient to discriminate the H_1, H_2, H_3 and aromatic protons. Build-up curves were extracted from a series of 2D LGCP-HETCOR experiments with various contact times (Figure 5.6 (B) and (C)). As expected, the LGCP build-up indicate proximities between the aromatic protons and carbon, and H_1 and the silicon T sites. Interestingly, correlation between protons of the organic moiety and the silicon Q sites and TMS silicon could be obtained, indicating folding of the organic moiety towards

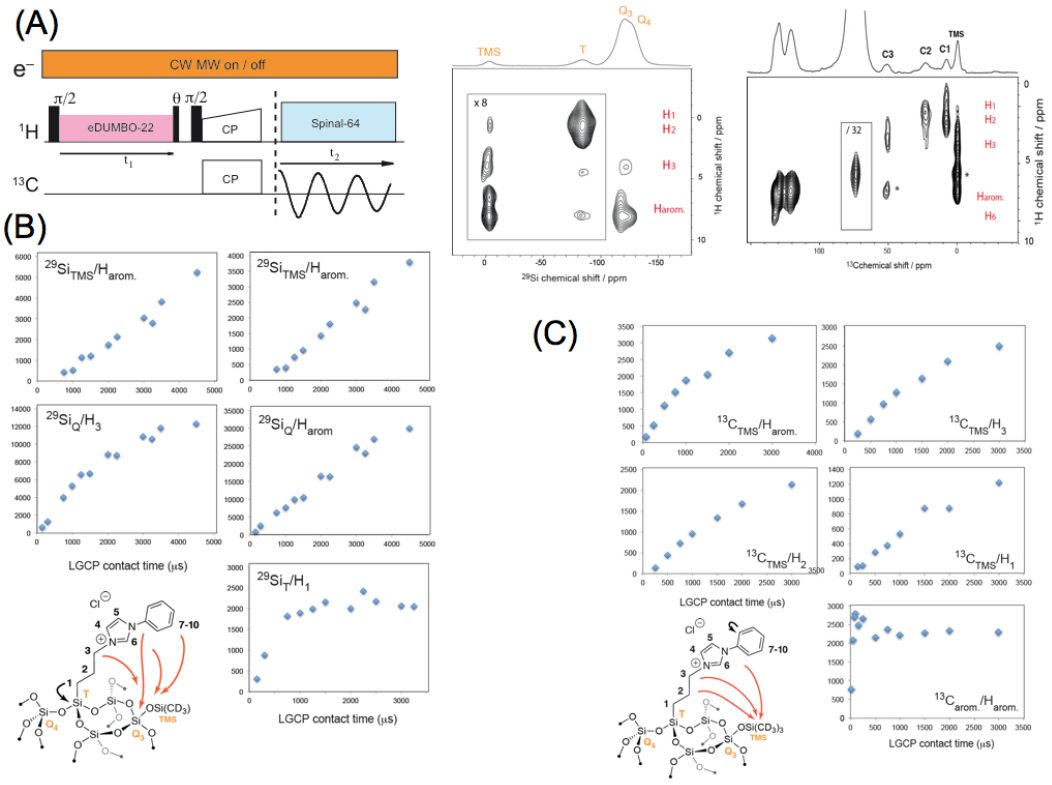

Figure 5.6: (A) LGCP-HETCOR pulse sequence, (B) **Mat-PrIm,TMS** impregnated with 16 mM TEKPOL2 solution in TCE

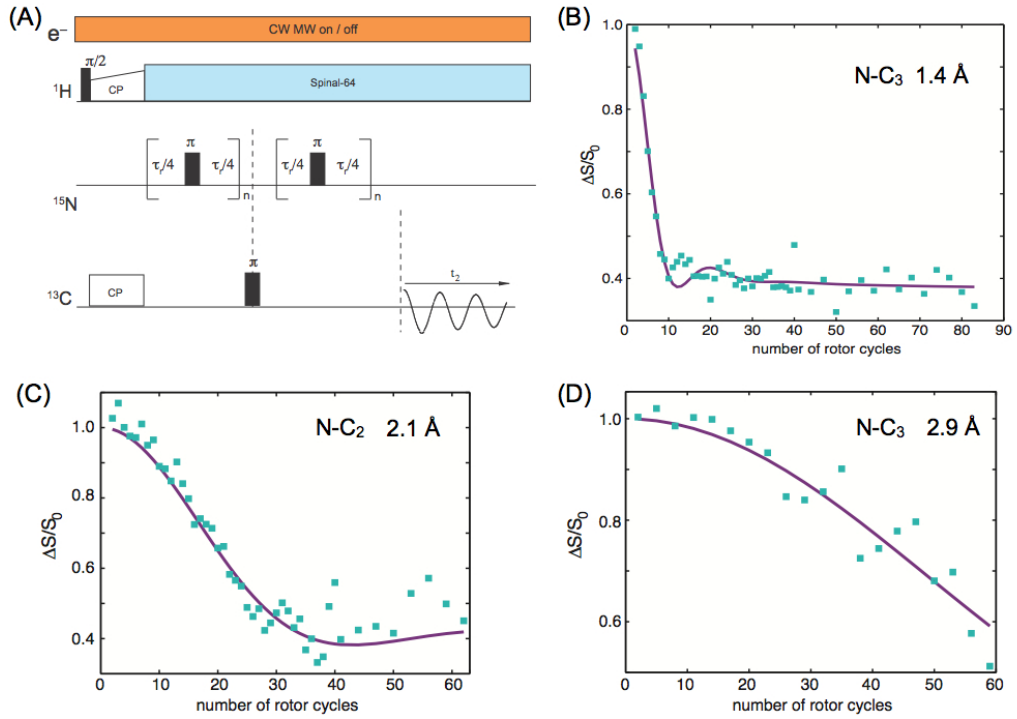

Figure 5.7: (A) REDOR pulse sequence (B) ^{15}N-$^{13}C_3$ (C) ^{15}N-$^{13}C_2$ and (D) ^{15}N-$^{13}C_1$ REDOR dephasing curves of **Mat-PrIm,TMS** impregnated with 16 mM TEKPOL2 solution in TCE (squares) and the best distance fit (line)

the surface. The fitting of these curves to determine complete structures is currently underway.

Structural information can also be obtained from Rotational-Echo, Double-Resonance NMR (REDOR), an experiment for measuring the dipolar coupling between a heteronuclear spin pair, and eventually the distance between the two atoms.[140] In our case, it is used to probe ^{15}N-^{13}C. Due to sensitivity issues, and the presence of multiple nitrogens in the molecule, labeling of one of the nitrogen was mandatory (see Figure 5.5). ^{15}N-$^{13}C_3$, ^{15}N-$^{13}C_2$, and^{15}N-$^{13}C_1$ distances could be extracted (Figure 5.7). The ^{15}N-$^{13}C_3$ and ^{15}N-$^{13}C_2$ extracted are relatively close to canonical values. The ^{15}N-$^{13}C_1$ provides a strong distance constraint on the conformation of the chain and allows to discriminate between trans and gauche conformation and fixes the C_1-C_2-C_3-N dihedral angles, once again indicating folding onto the surface. More work on the REDOR is currently being done, and the possibility of us-

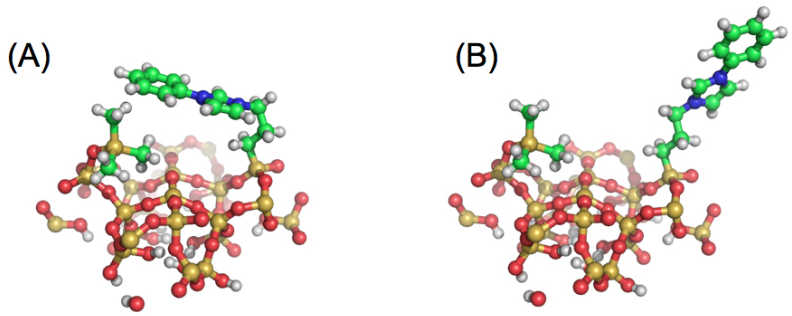

Figure 5.8: Molecular structures of **Mat-PrIm,TMS** with (A) the ^{15}N-^{13}C$_1$ distance of 2.9 Åobtained with the REDOR experiments and proximities between the aromatic ring and the TMS moiety given by the LGCP experiments, and (B) in a trans conformation and the ring pointing away from the surface., yielding a ^{15}N-^{13}C$_1$ of 3.6 Å. Structure A is compatible with the data, while structure B is not.

ing ^{15}N-^{29}Si REDOR experiments to extract more constraints is investigated. The next step in this study would be to run the same experiments on the Pt functionalized material and see if the conformation is changed.

Chapter 6

DNP SENS on polarisation conductors

So far, DNP SENS was used to selectively polarize the protons at the surface of materials, and subsequently the heteroatoms present at the surface (or just underneath[83]) via CP. As the core of the materials contained no protons, this technique is very efficient at selecting the surface of the materials, where the active sites reside. This approach presents many similarities with DNP in bulk; with the radical being more or less homogeneously dispersed in the pores of the materials (or interstices between the materials). But if the materials contains a significant amount of protons in its core, the hyperpolarization is expected to be transferred to the core of the material via proton-proton spin diffusion, thereby changing significantly the dynamics of the system. This chapter will explore some application of DNP SENS to polarization-conductors. After laying a succinct theoretical background on spin diffusion, we will see how polarization of the surface of micro crystals can lead to hyperpolarization of the whole systems, before seeing an application of this technique to pharmaceutical compounds. Finally, a last part will be dedicated to the calculation of spin-diffusion coefficient using *ab initio* spin dynamics simulations.

6.1 Spin Diffusion

6.1.1 Generalities

Spin diffusion is a process which opposes any inhomogeneity of polarization in a solid. The concept was first introduced in 1949 by Bloembergen to explain the unexpected efficiency of paramagnetic impurities as relaxation sinks in a

solid sample:[141] although paramagnetic impurities are expected to reduce considerably the T_1, their range of action is limited. Their impact over the whole sample had to involve spatial transfer of polarization, via what was called spin diffusion. Nuclear spin diffusion can be defined as a spontaneous transfer of polarization between (homonuclear) spins driven by the dipolar interaction. A non-uniform distribution of polarization in the sample can be created by selecting a group of spin using spectroscopic parameters allowing for their individual selection (such as chemical shift); or can be found when polarization is created or depleted faster in some regions of the sample (due to differences in relaxation times for instance or local hyperpolarization).

The high-field secular Hamiltonian for two coupled spins i and j is:

$$H = \frac{\mu_0 \gamma^2 \hbar^2}{8\pi r_{ij}^3}(1 - 3cos^2\theta_{ij})(2I_{iz}I_{jz} - \frac{1}{2}(I_{i+}I_{j-} + I_{i-}I_{j+})) \tag{6.1}$$

where r_{ij} is the distance between the spins and θ_{ij} is the angle between the static magnetic field and the internuclear vector.

Although spin diffusion is a coherent microscopic process driven by dipolar interaction, the dynamic of the system can be described by a macroscopic equation of diffusion:[141, 118, 142, 143, 144]

$$\frac{\partial P}{\partial t} = D\Delta P \tag{6.2}$$

where P is the polarization in the lattice, Δ the Laplacian operator and D the diffusion constant. This constant can be measured experimentally and number of experiments are available to do so.[145, 146] Due to its spatial dependance, spin diffusion is also widely used in NMR to measure distances between nuclei and plays an important role in structural determination.

In our case, spin diffusion is of great importance because the DNP process will create a gradient of polarization in the sample, between the spins that are directly polarized by the electrons and the others. With the impregnation DNP approach used for DNP SENS above, only the surface is polarized, but if the material can conduct polarization (i.e. protons are present in the bulk), spin diffusion will be important to polarize the whole structure, as we will see in the next sections.

6.1.2 DNP and Spin Diffusion

In Frozen Solution

A simple picture of DNP was for a long time to say that protons close to the radical center were polarized directly through the CE and that ^{1}H-^{1}H spin diffusion equilibrated the polarization throughout the sample. Recent studies showed that the actual picture is more complicated, and that protons further away from the radical could be directly polarized.[34, 35, 37, 36] Although very interesting, this debate is out of the scope of this work and will not be detailed here.

Polarizing Nanocrystals

In 2006, van der Wel *et al.* used DNP to investigate nanocrystals of the amyloid-forming peptide $GNNQQNY_{7-13}$ derived from the yeast prion protein Sup35p.[79] Even if these crystals are insoluble in water, they managed to obtain high enhancements ($\sim$ 120 at 5 T and 90 K) by suspending them in the usual TOTAPOL solution in 60:30:10 glycerol:D_2O:H_2O. Their study shows that only a small fraction of the crystal is polarized directly through the usual DNP processes, at the solvent/matrix interface; and that spin diffusion allows for the hyperpolarization to travel into the crystal. Using a 1D steady-state model based on Fick's law, and taking into account nuclear relaxation, they showed that in their case, substantial polarization could be obtained at the center of the crystal (up to 50 % of the surface enhancement). Using these results, Debelouchkina *et al.* investigated by NMR the structure of both GNNQQNY nanocrystals and amyloid fibrils.[66]

These results proved that polarization conducting materials could be studied using DNP and that objects up to 100 nm could be efficiently polarized. The longstanding interest of our team for NMR crystallography made us wonder wether this technique could be applied to micro crystals, and in particular to compounds with long T_1.

6.2 DNP on Organic Micro-Crystals

Solid-state NMR is the richest source of structural and dynamic information for powdered solids. Today it is probably most widely employed to characterize powdered (microcrystalline) molecular samples, and experiments employing ^{1}H, ^{13}C, and increasingly other nuclei (e.g., $^{15/14}$N, ^{19}F, ^{31}P, ^{35}Cl, etc.) are now routinely employed as probes of structure and packing (i.e., hydrogen

bonding).[147, 145, 148, 149, 150, 151, 152, 153, 154, 155, 156, 157, 158, 159, 160] For example, structural polymorphism is an issue of great importance for pharmaceutically relevant compounds, and solid-state NMR is today a primary tool for investigating and differentiating polymorphs.[149, 152, 161, 162, 163, 164, 165, 166] In favorable cases it is possible to determine complete *de novo* three-dimensional crystal structures from solid-state NMR of powders. Such NMR crystallography approaches are performed with a number of techniques, using NMR alone, or in combination with DFT chemical shift calculations, structure prediction methods, or powder X-ray diffraction.

However, the main limitation to the broader application of these methods is the poor sensitivity of NMR. This can be illustrated through the low sensitivity of natural abundance ^{13}C or ^{15}N experiments. It is often impractical to record ^{15}N spectra at natural abundance except for the simplest, most concentrated compounds. Even in favorable cases, two-dimensional ^{13}C-^{13}C correlation experiments or one-dimensional spectral editing experiments require times on the order of days. Such experiments are usually unavoidable to assign resonances, with the assignment step being essential to determine detailed structures or dynamics. For compounds with unfavorable properties one-dimensional spectra are often a challenge and it is usually impossible to perform more complex NMR experiments.

Long relaxation times are particularly problematic. Rigid compounds, for example, sulfathiazole,[167] glucose, and many other organic solids,[168, 169, 170, 171, 172] typically possess proton spin-lattice relaxation times ranging from 150 to 1000 s at room temperature. In comparison, compounds, such as most proteins, which are flexible and/or possess methyl groups, are characterized by short $T_1(^1H)$ on the order of 2 s. The sensitivity of solid-state NMR experiments will thus be reduced by at least an order of magnitude in such compounds.[141] One solution to the relaxation time problem is to add low concentrations of paramagnetic impurities into the crystalline lattice to enhance relaxation;[168, 141] however, this cannot be a general approach as doping requires recrystallization or irradiation and results in modified or impure phases. In particular, for example, it is not applicable to the study of polymorphs or pharmaceutical compounds. Another approach currently developed in our group, and which would not modify the sample, would be to coat the exterior of the crystal with paramagnetic species and therefore reduce the $T_1(^1H)$ of the sample. This approach can easily be combined with DNP, using the usual polarizing agents (TOTAPOL, bTbK, bCTbK...) as the coating paramagnet. DNP-enhanced NMR spectra can be obtained from micro-crystalline solids by impregnation with radical-containing organic so-

lutions, where the impregnating liquids are carefully chosen to be nonsolvents for the compounds. In order to understand how for such externally doped organic solids ^{1}H-^{1}H spin diffusion can efficiently relay enhanced polarization over micrometer length scales and yield substantial bulk ε a numerical model has been developed taking into account both spin diffusion and T_1 relaxation.

6.2.1 Numerical Simulations of Spin Diffusion.

The theoretical model is similar to that presented by Griffin and co-workers;[79] however, here we develop a framework suited to samples with long T_1 values and larger three-dimensional objects. Notably the framework is numerical and is not limited to the steady state. We note in passing that several other research groups have presented models describing the enhanced longitudinal relaxation of systems heterogeneously doped with paramagnets.

Theoretical framework

The aim is to simulate polarization build-up curves for crystalline materials externally coated with radical solutions. The model must account for experiments with and without microwave irradiation to drive DNP. The starting point here for the analysis is the diffusion equation under the assumption that the crystals possess spherical symmetry:

$$\frac{\partial P(r,t)}{\partial t} = D(\frac{\partial^2 P(r,t)}{\partial r^2} + \frac{2}{r}\frac{\partial P(r,t)}{\partial r}) - \frac{P(r,t) - P_0(r)}{T_1(r)} \qquad (6.3)$$

where r is the distance from the center of the spherical crystal in angstroms ($0 < r < R$ with R the crystal radius), t is time in seconds ($0 < t < \infty$), $P(r,t)$ represents the polarization, which is a function of position and time, and $P_0(r)$ is the local equilibrium polarization in the absence of spin diffusion (for example, thermal equilibrium corresponds to $P_0(r) = 1$). To solve this equation we make the following assumptions: (i) we assume that at the surface of the crystal there is a layer for which T_1 is reduced by direct paramagnetic relaxation. The T_1 at the surface is short ($T_{1,surf}$, taken here to be 1 ms). The T_1 of the nuclei near the surface increases with increasing distance from the surface with a classical (r^{-6}) dependence. Within a few tens of angstroms from the surface T_1 attains the value of the intrinsic core T_1 ($T_{1,core}$, assumed here to be 700 s). (ii) $P_0(r)$ is set as follows: for the case of no microwave irradiation, the equilibrium polarization is arbitrarily chosen to be 1 everywhere. For simulations with microwave irradiation to drive DNP, we consider that a 20 Å shell is directly enhanced by DNP. For this shell P_0 is 100, while for the rest of the crystal P_0 is 1. Under the influence

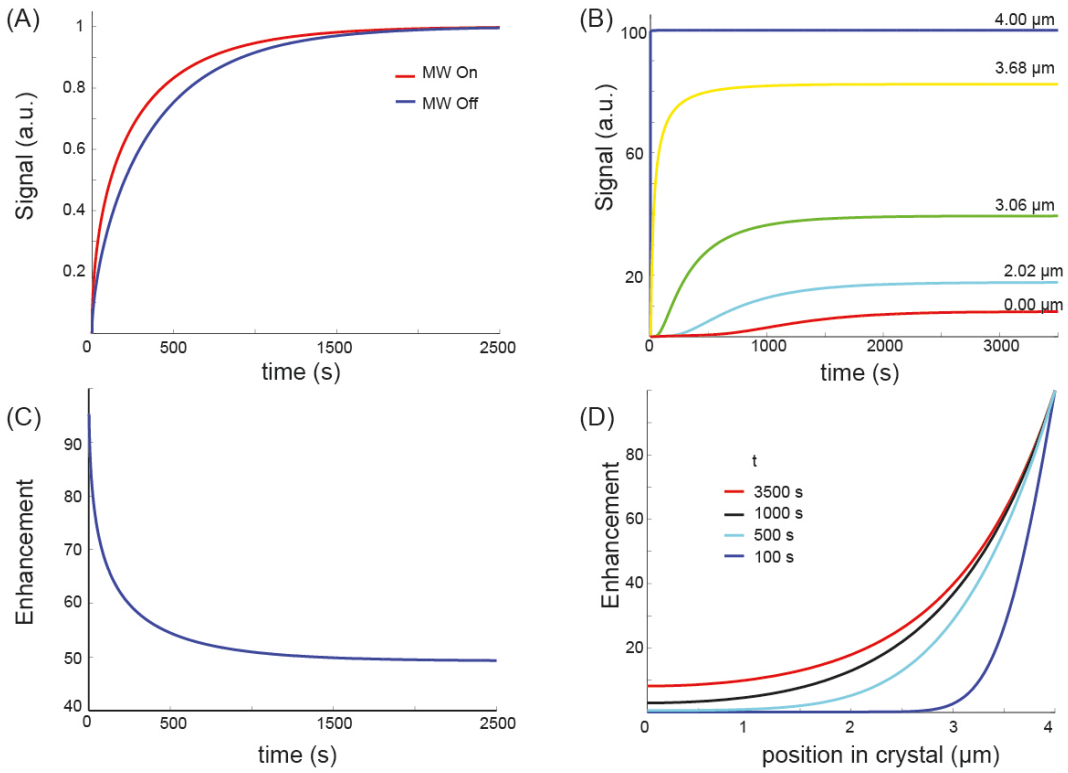

Figure 6.1: (A) MW On and Off build up curves (B) Signal build-up MW On for various positions in the crystal (C) ε as a function of build-up time and (D) ε profiles in the crystal for different times simulated for a crystal of 4μm diameter, with a T_1 of 700 seconds. The surface T_1 was set to 2 s, and the diffusion constant was set to 10^{-3} $\mu^2.s^{-1}$

of spin diffusion, polarization will then tend to be equalized throughout the crystal. Here we do not assume a steady state condition, since $T_{1,core}$ for the microcrystalline samples is often greater than 500 s at low temperatures, and a steady state is not usually achieved in the experiments.

To solve this equation, it is necessary to have a set of initial and boundary conditions. Here our initial condition corresponds to the saturation of all polarization before the build-up; and the boundary condition is a so-called Neumann boundary condition and corresponds to a situation where no polarization is diffusing out of the crystal (i.e., there can only be diffusion of polarization from the surface of the crystal inward; this is physically reasonable if the radical-containing solvent layer has a short T_1, which will always be the case here). These conditions translates in mathematical terms to:

$$P(r,0) = 0 \tag{6.4}$$

and

$$D\frac{\partial P(R,t)}{\partial r} - \frac{R}{T_{1,surf}}[P(R,t) - P_0(R)] = 0 \tag{6.5}$$

With these two conditions the diffusion equation can be numerically integrated to obtain the polarization as a function of time and position. If the polarization is integrated over the spherical crystal, the volume weighted signal build-up function $S(t,R)$ for a crystal of radius R can be obtained:

$$S_{on/off}(R,t) = \int_0^R P_{on/off}(r,t)r^2 dr \tag{6.6}$$

where S_{on} corresponds to the microwave irradiation case and S_{off} corresponds to no microwave. The DNP enhancement for a single crystallite as a function of time can then be calculated as:

$$\varepsilon(R,t) = \frac{S_{on}(R,t)}{S_{off}(R,t)} \tag{6.7}$$

Using these assumptions, numerical spin diffusion models were constructed with MatLab v7.10 (The MathWorks, Inc.).

First results, analysis of the MW on and off build up curves

The few angstrom layer affected by the PRE will build up polarization quickly (with a T_1 ranging between 1ms and 700s). The rest of the crystal will build up polarization slowly. This difference of build-up rate throughout the crystal means that at any time, there will be a gradient of polarization in the

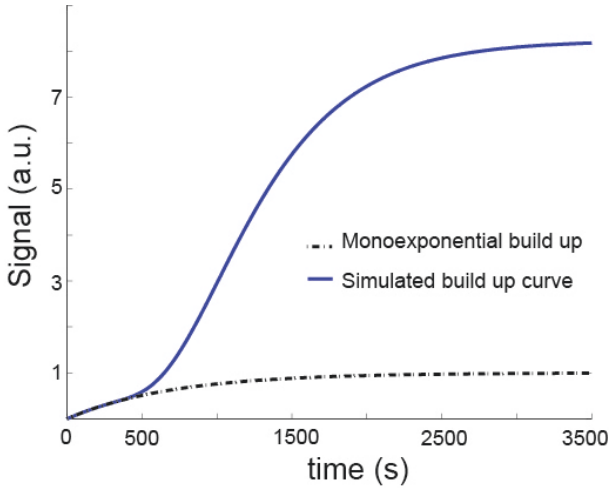

Figure 6.2: blue: Simulated build up curve of the signal at the center of a 4 μm crystal, with a 700 s core T_1 and a 2 s surface T_1. The surface enhancement was set to 100. Black: Theoretical monoexponential build-up curve for a pristine crystal with a 700 s T_1. The thermal equilibrium polarization was arbitrarily set to 1.

crystal (the outside being more polarized than the inside). Spin diffusion will tend to homogenize polarization by transferring some from the outside of the crystal to its inside, therefore leading to a quicker build-up. At a given time, the amount of polarization transferred from faster-building regions depends on the position in the crystal, therefore leading to position-dependent build up curves (Figure 6.1) Therefore, integration over the whole crystal leads to a build up that can be fitted using stretched exponentials to take into account the distribution build up behaviors throughout the crystal, as illustrated if Figure 6.1 and Table 6.2.1. When the MW is turned on, not only the outside of the crystal relaxes rapidly, but it builds up to a enhanced, non-thermal polarization due to direct DNP enhancement (100 in our simulations). This hyperpolarization will be propagated inside the crystal in the same fashion thermal polarization was, but T_1 relaxation will tend to dissipate it as it progresses inside of the material. The outer zones of the crystals are going to be the more polarized ones, and therefore will weight more on the signal (obtained by integration over the crystal). As they also are the one building faster, the MW ON build-up curve will each more quickly equilibrium than the MW Off one. The behavior of ε as a function of time seen in Figure 6.1 can be explained by the fact that at short times, only the outside of the crystal weights in the integral, therefore leading to high enhancements.

	MW Off	MW On
T_1^{*a} (s)	192	251
β^a	0.65	0.69
$\bar{T_1}^b$	262	322
r^{2c}	0.999	0.999

a: The simulated build-up curves were fitted with a stretched exponential function of the form: $I(t) = I_0[1 - exp(-(t/T_1^*)^\beta)]$. *b*: Center of the T_1 distribution given by: $\bar{T_1} = T_1^*/\beta * \Gamma(1/\beta)$. *c* correlation coefficient.

Table 6.1: Fit parameters for the simulated build-up curves

At longer times, the center of the crystal starts to get polarized, with lower enhancements than the surface due to T_1 induced dissipation, therefore lowering the overall enhancement of the crystal. This can be seen in details in Figure 6.2: up to 500s, the build up of polarization at the center of the crystal matches the theoretical mono exponential build up. After this point, hyperpolarization reaches the center of the crystal and its polarization increases more rapidly and to a higher value (around 8 here).

Influence of $T_1(^1H)$ on ε

As seen in Figure 6.3, with larger values of the core T_1 values the DNP enhancements are larger since enhanced polarization can diffuse over greater distances before being dispersed by longitudinal relaxation. However, longer core T_1 values are also predicted to be accompanied by slower signal build-up rates

Influence of the crystal size on ε

Figure 6.3 shows that smaller crystals yield higher enhancements. This can be explained by the smaller length over which polarization has to diffuse, yielding to less efficient T_1 relaxation. Note that as the particle size goes to zero, the enhancement profile converges toward that of a frozen solution, where ε do not depend on the build up time. In order to more accurately reproduce the experimental results and reproduce the dispersion of crystal

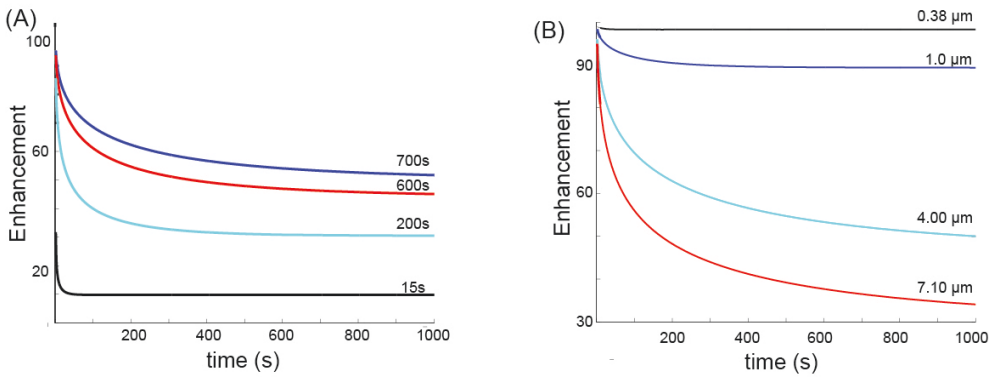

Figure 6.3: Simulated ε for (A) a 4 μm radius crystal with different $T_{1,core}$ and (B) various crystal sizes with a 700s $T_{1,core}$

sizes, powder-averaged results can be generating using a distribution of sizes (normal, Weibull etc...). To reproduce the results on crystal ground by hand, we used a Weibull distribution. However, the general trends obtained for ε as a function of time, particle size or proton T_1 are similar to the ones obtained using single crystals, so the powder-averaged results will not be treated here. The interested reader can find them in ref [123].

6.2.2 Experimental results.

DNP Solid-State NMR Experiments on Microcrystalline Glucose.

Glucose was chosen for this study because it possesses a long $T_1(^1H)$ of $\sim$ 180 s at room temperature. The T_1 at 100 K is estimated to be 650 s. Prior to DNP experiments, its solubility in several organic liquids suitable for DNP was screened by visual inspection and solution NMR experiments.[123] Glucose was found to be insoluble or very weakly soluble in several organic liquids. 1,1,2,2-tetrabromoethane ($EtBr_4$) was chosen since the ^{13}C chemical shift of this solvent (centered around 47 ppm) has minimal overlap with the glucose resonances. The bCTbK biradical was employed as a polarizing agent. The glucose sample was finely ground by hand in a mortar and pestle to reduce the average grain size. The sample was impregnated with a minimal amount of 16 mM bCTbK $EtBr_4$ solution by using the incipient wetness impregnation technique, then transferred to a sapphire rotor.
$\varepsilon_{C,CP}$ greater than 60 are readily obtained, and as predicted above the magnitude of $\varepsilon_{C,CP}$ depends upon the recycle delay (τ) used to acquire the spectra

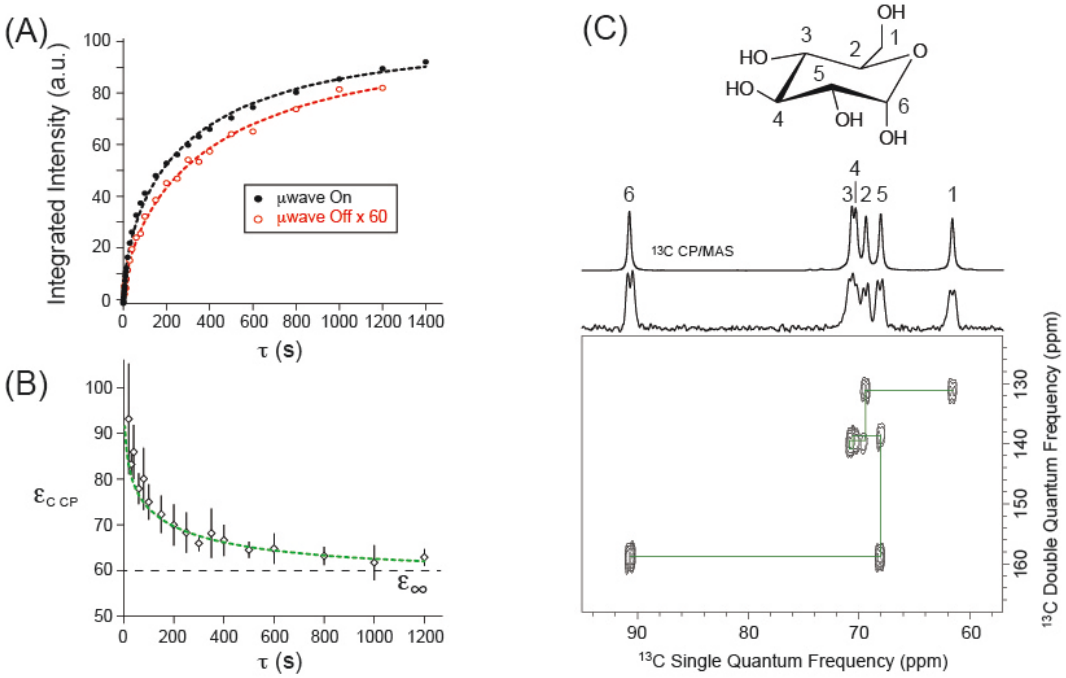

Figure 6.4: (A) Normalized signal intensities as a function of τ for the ^{13}C resonance at 90.7 ppm acquired with (black) and without (red) microwave irradiation. Stretched exponential fits of the experimental curves are shown in dashed lines. The results of the curve fitting are given in Table 1. (B) The measured value of $\varepsilon_{C,CP}$ as a function of τ (open circles) and values calculated with a ratio of stretched exponential functions (green line). (C) 2D refocused INADEQUATE[173] ^{13}C-^{13}C correlation spectrum of glucose acquired at natural isotopic abundance. A ^{13}C CP/MAS spectrum acquired with 4 scans and a 60 s recycle delay is overlaid on top of the projection spectrum for comparison. The spectrum was acquired in a total experiment time of 16 h (30 s recycle delay, 30 t_1 increments, 64 scans per t_1 increment, and $\Delta t_1 = 80$ μs). A 4 ms delay was employed for generation of double quantum coherences. The molecular structure of glucose is shown and the carbon resonances are assigned. The connectivity of the carbon atoms is mapped out on the 2D spectrum (green line). Note that the one bond carbon-carbon scalar (J) couplings are resolved in ω_2 dimension of the INADEQUATE spectrum.

	MW Off	MW On
T_1^{*a} (s)	293	390
β^a	0.60	0.66
$\bar{T_1}^b$	440	524
ε_∞^c	-	60

a: Experimental build-up curves were fitted with a stretched exponential function of the form: $I(t) = I_0[1 - exp(-(t/T_1^*)^\beta)]$. The average build up fitted over 3 pics are given here *b*: Center of the T_1 distribution given by: $\bar{T_1} = T_1^*/\beta * \Gamma(1/\beta)$. *c* Steady-state ε.

Table 6.2: Fit parameters for the experimental build-up curves

(Figure 6.4 (A),(B)). With DNP very high S/N spectra can be rapidly acquired. For example, for the spectrum acquired with microwave irradiation and a 60 s recycle delay the S/N is about 750 after only 4 scans (4 minutes experimental time). As expected, the MW On and Off build up differ quite significantly and can be fitted quite accurately using stretched exponential functions (Figure 6.4 (A) (B) and table 6.2.2).

Importantly, we note that despite the fact that the samples are cooled to 100 K to obtain a large ε , the resolution of the spectrum is comparable to that obtained at room temperature, with average full widths at half height (Λ) of 0.33 ppm at 105 K as compared to 0.28 ppm at 298 K for dry powdered glucose.[123] The high spectral resolution observed here contrasts with that typically observed in DNP solid-state NMR experiments on molecules dissolved/immobilized in glass-forming solvents where Λ is typically on the order of 2-5 ppm. The small Λ for glucose (and other microcrystalline solids, vide infra) at 105 K are obtained because such rigid molecules exist in a highly ordered environment within the crystalline lattice that does not become disordered at low temperature. This is consistent with Griffin and co-workers who obtained high resolution for microcrystalline tripeptides at 85 K.[79]

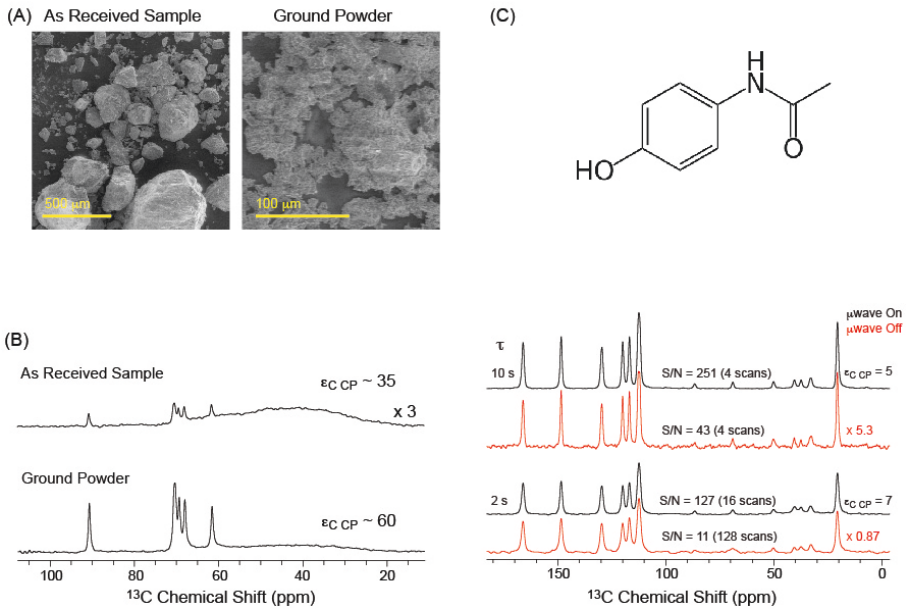

Figure 6.5: (A) SEM images (FEI Quanta 200 FEG ESEM) of the as-received microcrystalline glucose and glucose that was ground by hand in a mortar and pestle. (B) DNP-enhanced ^{1}H-^{13}C CP MAS spectra of the as-received glucose and ground glucose acquired with 4 scans and a 10 s recycle delay. The broad resonance of $EtBr_4$ centered around 45 ppm is also visible. (C) Molecular structure and ^{1}H-^{13}C CP MAS solid-state NMR spectra of paracetamol impregnated with 16 mM bCTbK 1,3-dibromobutane solution acquired with (black) and without (red) microwave irradiation. The $\varepsilon_{C,CP}$, intensity scaling factor of the microwave off spectra, S/N, recycle delay, and number of scans acquired for each spectrum are provided.

The Influence of Grain Size and T_1 on ε

The effects of the grain size on ε were investigated by performing DNP experiments on both glucose ground by hand in a mortar and pestle and on as-received glucose (Figure 6.5). Scanning electron microscope (SEM) images of both samples are also pictured (Figure 6.5). As predicted in the theory section, for the ground and as received samples we observed $\varepsilon_{C,CP}$ of 60 and 35 respectively, for experiments conducted with a τ of 10 s. In addition to the reduction in $\varepsilon_{C,CP}$ for the as-received sample, the signal per unit mass of the as-received sample was 11.5 times lower than that of the ground sample. This reduction occurs because both the $\varepsilon_{C,CP}$ and the relaxation properties of the as-received sample will be less favorable due to the lower accessible surface area, and larger grain size. SEM images of the two samples show that the grain sizes are heterogeneous in both samples; however, for the as-received sample there are many more large particles, with particles as large as 500 μm present (Figure 6.5). Conversely, in the ground sample there are many more sub-20 μm diameter grains. Both the reduction in ε and an increase in T_1^* are predicted for larger grain sizes by our theoretical model. This illustrates that by simply grinding the sample by hand prior to DNP experiments, larger enhancements and improved sensitivity can be obtained. (Although we note that this may not always be possible since some polymorphs are sensitive to even gentle grinding. In rare cases, extreme grinding may also introduce defects into the crystal or at the surface that enhance longitudinal relaxation rates; which might reduce the DNP enhancement that could be obtained).

In order to verify the predicted impact of short T_1 on the enhancement, similar experiments were performed on microcrystalline paracetamol (acetaminophen). Paracetamol contains a methyl group and $T_1(^1H)$ is on the order of 2 s at room temperature. At 105 K for a sample impregnated with a 16 mM bCTbK Br_2Bu solution (which provides lower DNP enhancements than $EtBr_4$; but was necessary as paracetamol is soluble in $EtBr_4$) the relaxation data could be fit with a monoexponential function and $T_1(^1H)$ was measured to be 13.7(5) s (with DNP). A $\varepsilon_{C,CP}$ of 5 was obtained. As expected from the short value of T_1 and our theoretical modeling, the value of $\varepsilon_{C,CP}$ is greatly reduced as compared to the $\varepsilon_{C,CP}$ for glucose.

Acquisition of Natural Abundance 2D ^{13}C-^{13}C Correlation Spectra.

For glucose the large sensitivity enhancements provided by low-temperature DNP experiments enable the acquisition of ^{13}C CP/MAS spectra with S/N of around 1000 in experiment times on the order of minutes. It is necessary

to have a high level of S/N for natural abundance ^{13}C-^{13}C correlation experiments since the S/N will be reduced by at least a factor of 100 by the double-quantum ^{13}C filter. Figure 6.4 (D) shows a 2D ^{13}C-^{13}C through-bond refocused INADEQUATE spectrum. The INADEQUATE spectrum enables the connectivity of the molecule to be determined, which immediately yields the assignment of the complete ^{13}C spectrum. We note that the carbon-carbon J- couplings are well resolved in , highlighting the high resolution of the low-temperature spectrum. A natural abundance through-space (dipolar) 2D POST-C7 1^{13}C-^{13}C correlation spectrum was also acquired, probing through-space contacts.[123] We note that both 2D spectra were acquired with experiment times of only approximately 16 h each. For comparison, the acquisition of natural abundance ^{13}C 2D INADEQUATE spectra of microcrystalline organic complexes with favorable relaxation characteristics usually requires experiment times on the order of 3 to 10 days even with larger size rotors and higher static magnetic fields than those used here. Acquisition of a ^{13}C-^{13}C correlation spectrum of crystalline glucose without DNP would require months of spectrometer time, which clearly demonstrates the large sensitivity enhancement provided by DNP.

To prove the applicability of this technique to non-model and more complex systems, we used it on a classic system that displays polymorphism and has been extensively studied: sulfathiazole.[167] Sulfathiazole lacks methyl groups and its $T_1(^1H)$ is between 200 and 500 s at rt for the various polymorphs. Experiments were performed on a sample of ground sulfathiazole impregnated with a 16 mM bCTbK solution in $BuBr_2$ (sulfathiazole being soluble in $EtBr_4$). All of the results and observations from DNP experiments on sulfathiazole are similar to those made for glucose. While relaxation measurements of $T_1(^1H)$ were not performed for sulfathiazole, the value of $\varepsilon_{C,CP}$ was observed to be strongly dependent upon τ ($\varepsilon(\tau = 10s) = 57$, $\varepsilon(\tau = 30) = 51$ and$\varepsilon(\tau = 120s) = 43$). With $\varepsilon_{C,CP}$ greater than 40, very high S/N spectra could be rapidly acquired and once again there appears to be no major loss in resolution at low temperatures. The large sensitivity gain provided by DNP again enabled the acquisition of a 2D refocused INADEQUATE in only 16 h at natural ^{13}C isotopic abundance (Figure 6.6), yielding the complete carbon-13 assignment.

These examples show that DNP could be of great use for the study of compounds with long T_1 by NMR, providing both enhancement and faster build up of the signal. This method is also potentially useful to study solid solutions or formulations, and could be used to extract domain sizes thanks to the dependance of ε with the size of the particles. In the next session, we

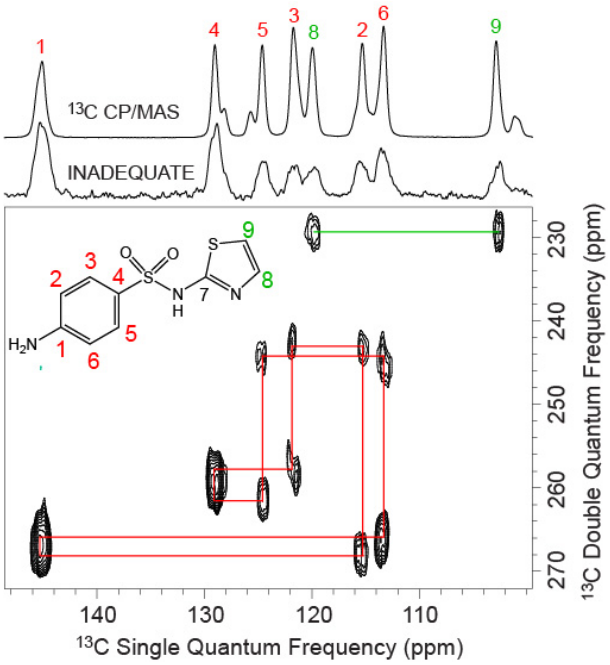

Figure 6.6: 2D refocused INADEQUATE ^{13}C-^{13}C correlation spectrum of sulfathiazole acquired at natural isotopic abundance. A ^{13}C CP MAS spectrum is overlaid on top of the projection spectrum for comparison. The spectrum was acquired in the same condition as the glucose INADEQUATE described in the caption of Figure 6.4. The molecular structure of sulfathiazole is shown and the carbon resonances are assigned. The connectivity of the carbon atoms is mapped out on the 2D spectrum.

will focus on the application of DNP on pharmaceutical formulations.

6.3 DNP Enhanced NMR to Probe the Microstructure of Formulations

The characterization of the composition and structure of formulated multi-component materials in general, and of pharmaceutical formulations in particular, is of great industrial importance today, yet in many respects it remains an unsolved analytical challenge. While several methods can be used as indirect probes of the properties of formulations, there are very few direct probes available. While NMR based techniques have have been successfully demonstrated for the characterization of pure crystalline powdered solids, it

would be of great interest to extend these techniques to the characterization of active pharmaceutical ingredients (API) in formulations. This could enable solid-state NMR structure determination "in situ", allowing polymorph screening and identification, quantification of the degree of crystallinity of the API, measurement of domain sizes, and/or the determination of API-excipient interactions. Characterization of these properties is especially important, since they influence the activity/release properties of the formulations, and the overall stability of the API phase.[174, 175, 176, 177] However, the characterization of formulated APIs by solid-state NMR is often challenging due to the combination of the intrinsically low sensitivity of NMR, long T_1 and the low API content of many formulations (typically between 5 and 10 wt %). More importantly, the ^{1}H and ^{13}C solid-state NMR spectra of formulations generally possess many overlapping resonances from the large number of constituents, and multidimensional NMR spectra are generally required to restore spectral resolution and information content. Moreover, multidimensional methods are often essential to probe API-excipient interactions, or any of the other structural features discussed above. In formulations where resolution is high enough to permit ^{1}H NMR experiments[161] or highly receptive nuclei are present (such as ^{19}F and ^{23}Na), multidimensional experiments are possible even at low API loadings.[178, 179, 180, 181] However, the low sensitivity of NMR usually precludes multidimensional acquisitions at natural isotopic abundance for ^{13}C and ^{15}N (to our knowledge, multidimensional ^{13}C experiments have only been previously reported for model formulations with high API contents >30 wt %),[182, 183, 184, 162] and thus, low sensitivity is the key barrier to the introduction of in situ NMR structural characterization methods for formulations. Applying the method previously developed on microcrystalline samples to pharmaceutical formulations would allows the rapid acquisition of 1D and 2D ^{1}H-^{13}C and ^{1}H-^{15}N solid-state NMR spectra from drug formulations, at natural isotopic abundance, with low API contents between and could be used to determine in situ the distributions of domain sizes of the API in a formulation.

6.3.1 Measuring API Domain Sizes with DNP

Here we use the dependance of ε on the build-up time τ to probe the domain sizes of the particles of amorphous cetirizine dihydrochloride (A) present within the complex superstructure within the formulation F1, obtained by impregnating a tablet containing 8.6 wt% of API with a 24 mM solution of TEKPOL in TCE. Very detailed description of the sample preparation, solubility of the API in TCE and other experimental parameters can be found in ref. [185], but will not be developed here. Such NMR domain

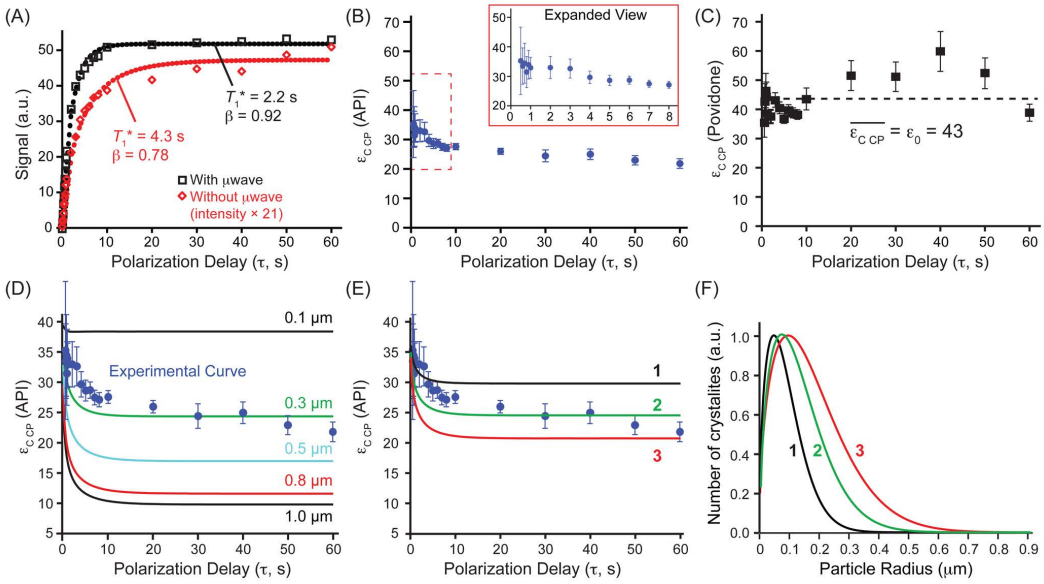

Figure 6.7: (A) Signal build-ups observed for F1 with a saturation recovery CP pulse sequence with (black) and without (red) microwave irradiation. Curves were fit with stretched exponential functions. The values of T_1^* and β are indicated. (B) The measured values of $\varepsilon_{C,CP}$ for the API resonance of F1 at 128 ppm as a function of polarization time. The inset shows $\varepsilon_{C,CP}$ at short τ. Error bars were calculated by propagation of error using the noise levels of the spectra acquired with and without microwave irradiation as the standard deviation. (C) Measured values of ^{13}C CP for the povidone resonance of F1 at 41.5 ppm. The average value of $\varepsilon_{C,CP}$ for P was 43, and this was assumed to be the enhancement at the surface of the API particles (ε_0). (D) Comparison between experimental and simulated ε of the API as a function of τ using a numerical model of spin diffusion for spherical particles of the indicated radius. (E) Simulations of the variation of ε for different Weibull distributions of the particle radius. (F) Plots of the Weibull distributions of the particle radius used in part E. Weibull distributions 1, 2 and 3 employed shape parameters (k) of 1.5 and the center of the distributions (?) was 0.10, 0.15 and 0.20 μm, respectively. For all simulations, the surface enhancement (ε_0) was fixed at 43, the proton longitudinal relaxation time (T_1) of the API was 5.3 s, the T_1 at the surface of the particles was set to 2.3 s to match the T_1 measured for povidone, and the diffusion constant (D) was 1.0 10^5A^2.s^{-1}. Taken from ref [185].

size measurements in complex materials (such as polymer blends) are usually accomplished with ^{1}H spin diffusion correlation experiments; however, this requires resolution of the different phases (or amorphous/crystalline domains) within the directly or indirectly detected ^{1}H NMR spectrum. For example, the molecular level association of APIs and excipients can be confirmed with dipolar HETCOR experiments. Carbon-13 detected proton T_1 measurements for excipients and API signals are also useful to place an upper limit on the size of API domains: the observation of distinct T_1's for the API and excipients proves phase separation, while the observation of a common T_1 usually suggests that the API exists in domains smaller than 100 nm that are well mixed with the excipient(s). However, domain sizes have never been directly measured by NMR for a formulated pharmaceutical compound. The advantage of the DNP based method is that no ^{1}H chemical shift differences are required; rather, only CP signal build-ups with and without microwaves need to be observed. For these experiments, F1 was packed into a thin wall 3.2 mm zirconia rotor to maximize sensitivity in the experiments without DNP.

As shown in Figure 6.7 (A) and (B), similar to previous observations for crystalline solids, we observed stretched exponential signal build-ups and a significant variation in $\varepsilon_{C,CP}$ for the aromatic API carbon resonances as a function of τ. This clearly indicates that A exists in distinct particulate domains within F1 and that the API is externally polarized through proton spin diffusion. Using our previously developed numerical model of the diffusion equation, we can simulate the signal build-up rates and variation in ε with τ for different particle size ranges. We assume that the proton longitudinal relaxation time within the amorphous A particles is 5.3 s based upon a measurement of the proton T_1 for amorphous A in F1 in the absence of added radical solution at 110 K. The enhancement at the surface of the API particles (ε_0) was assumed to be equal to the $\varepsilon_{C,CP}$ value measured for the P resonance at 41.5 ppm, which was found to be 43 (Figure 6.7 (C)). This assumption was made because the enhancement for the API is similar (but less than) the enhancement for P at short polarization delays. The enhancement for P does not decrease with the polarization delay (within the uncertainty of the measurements), and DNP experiments on pure impregnated P also indicate that the biradical solution is directly incorporated into the polymer. The spin diffusion constant (D) was assumed to be equal to 1.0 10^5 $A^2.s^{-1}$, a value typical of fully protonated organic solids. Using these parameters, simulations of ε as a function of τ with uniform radius particles provide the best agreement for 0.3 μm radius particles (Figure 6.7 (D)). For simulations with (traditional) Weibull distributions of particle radii, we find the agree-

ment is best with an equivalent distribution having a maximum around 0.07 μm (Figure 6.7 (E)). Note that both the single particle model and Weibull distribution models predict that the majority of particles have radii less than 0.3 μm. We attempted to confirm the DNP solid-state NMR based API domain size measurements with scanning electron microscopy-energy dispersive X-ray spectroscopy (SEM-EDX) mapping of chlorine within F1; however, the measurements were too insensitive because of the low Cl content of F1. SEM images of ground F1 indicate the presence of particles smaller than 1 μm in diameter, which is consistent with the DNP-NMR particle size measurements. As discussed above, in the present case, the impregnation procedure may slightly reduce the domain size of A due to the partial solubility of amorphous A in TCE. For formulations with crystalline API, this should not be an issue.

6.3.2 Probing API-Excipient Interactions with DNP Enhanced Solid-State NMR

For F1, both the ^{13}C and ^{15}N resonances of the API are much broader than those observed for the corresponding DNP enhanced spectra of crystalline A.[185] The observed chemical shifts and breadths of the observed resonances are similar to those observed for pure amorphous A, consistent with an amorphous phase of A within the formulations. The DNP enhanced ^{15}N CP MAS spectra of F1 possess two separated broad features with shifts centered around ca. 58 and 44 ppm. Additional broad ^{15}N sites with shifts between 54 and 51 ppm are also clearly visible for F1 and amorphous A. Natural abundance 2D ^{1}H-^{15}N HETCOR spectra of crystalline and amorphous A and F1 are shown in Figure ^{1}H-^{15}N HETCOR NMR spectra were acquired for F1, since it had the highest API wt %, although sensitivity is high enough that 2D 15N NMR spectra could also be acquired for the other formulations. The ^{1}H-^{15}N HETCOR spectrum of F1 acquired with a 3.0 ms contact time shown in Figure 5F indicates the presence of a ^{15}N chemical shift for A centered at 51.5 ppm. This ^{15}N chemical shift was not observed in the ^{15}N CP MAS spectra of crystalline A, but a similar chemical shift is observed in spectra of amorphous A. Within F1, the site at 51.5 ppm correlates to ^{1}H nuclei with chemical shifts of 1.7 ppm (and other aliphatic protons with shifts $>$2.0 ppm). Importantly, this correlation is not observed in the HETCOR spectra of amorphous A alone. ^{1}H-^{13}C and ^{1}H-^{15}N HETCOR spectra of P show that the ^{1}H nuclei of P possess shifts between 1.0 and 1.8 ppm, while all the ^{1}H nuclei in both amorphous and crystalline A possess chemical shifts greater than 2.7 ppm. Therefore, the ^{1}H-^{15}N correlation at 1.7 and 51.5 ppm

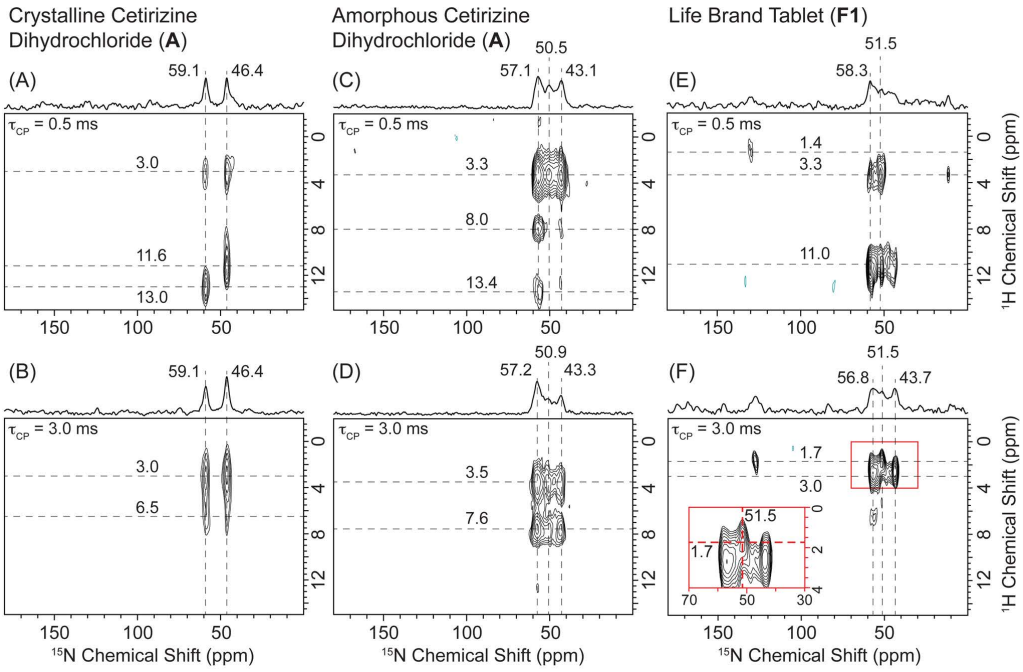

Figure 6.8: Natural abundance DNP enhanced ^{1}H-^{15}N dipolar HETCOR spectra of crystalline A (A and B), amorphous A (C and D), and F1 (E and F). The spectra were acquired with contact times (τ_{CP}) of 0.5 ms (top spectra) and 3.0 ms (lower spectra) to probe for short- and long-range ^{1}H-^{15}N distances, respectively. Key ^{15}N chemical shifts and ^{1}H correlations are indicated on the spectra with dashed lines. An expanded view of the correlations is provided for part F. HETCOR spectra of crystalline A were acquired with 4 scans per increment, an 8 s polarization delay, 52 individual t_1 increments, and a 64 μs t_1 increment (27 min each). HETCOR spectra of amorphous A were acquired with (C) 64 or (D) 48 scans per increment, a 5.2 s polarization delay, 64 individual t_1 increments, and a 64 μs t_1 increment (5.2 and 4.4 h, respectively). HETCOR spectra of F1 were acquired with 128 scans (E) or 96 scans (F) per increment, a 3 s polarization delay, 52 individual t_1 increments, and a 64 μs t1 increment (5.5 and 4.2 h, respectively). During t_1, eDUMBO-122 homonuclear ^{1}H dipolar decoupling[186] was applied and proton chemical shifts were corrected by applying a scaling factor of 0.57. The States-TPPI procedure was employed to achieve quadrature detection in the indirect dimension. Taken from ref [185].

indicates that a small amount of A is in contact with P (likely through dispersive forces and/or hydrogen bonding interactions). As discussed above, amorphous A exists within small sub-μm domains within F1. The ^{15}N resonance at 51.5 ppm likely corresponds to molecules of A at the surface of the amorphous API particles which interact with P. ^{1}H-^{13}C HETCOR spectra of F1 do not unambiguously show correlations between the povidone carbon nuclei and the protons of A because these key correlations are obscured in the crowded ^{1}H and ^{13}C spectra. This demonstrates one of the advantages of ^{15}N solid-state NMR for the analysis of pharmaceutical formulations. Finally, we note that as discussed above solution ^{1}H NMR spectra of extracts of F4 in an excess of TCE show signals from A. However, in the solution ^{1}H NMR spectrum, the peaks of A and P are both significantly broadened, suggesting that the A observed in solution is associated with P, consistent with the hypotheses above regarding A-P intermolecular interactions.

6.4 Prediction of spin-diffusion coefficients

As stated previously, spin diffusion arises from dipolar coupling and can be interpreted both on a microscopic an macroscopic level. On a microscopic level, the exchange of polarization via dipolar coupling is well defined and can be readily simulated for small spin systems (N $<$ 13) using standard density-matrix-type approaches.[187, 188, 189] However, the calculation of macroscopic spin diffusion rates directly from atomic coordinates is complicated by the very large number of spins involved[190] as well as by effects such as powder averaging and magic-angle spinning (MAS). Typically, spin diffusion is described on the macroscopic scale using the diffusion equation or a kinetic model where the polarization transfer rates are determined either empirically or from approximations based on simulations of small spin systems. No method currently exists for the calculation of the macroscopic spin diffusion rates for large spin systems, directly from the atomic coordinates. In this part, we bridge the gap between the microscopic and the macroscopic by combining an efficient first-principles method for simulating the evolution of large-N spin systems with an analytical solution of the 3D diffusion equation to extract macroscopic spin diffusion coefficients directly from crystal structures and including experimentally relevant effects such as MAS and powder averaging.

Our simulation method, called LCL for low-order correlations in Liouville space, uses a reduced Liouville space that includes only low spin orders to efficiently simulate spin diffusion in very large spin systems.[191] This

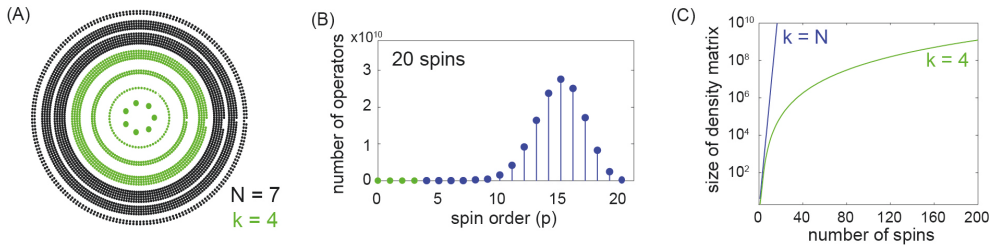

Figure 6.9: (A) Liouville-space representation of the density matrix (zero-quantum subspace) for N = 7 spins. Each dot represents an element of the density matrix, organized in rings according to spin order, p. For k = 4, only the elements in green (p ⩽ k) are propagated in the simulation. (B) Histogram of the number of zero-quantum-basis operators for a system of N = 20 spins as a function of spin order, p. (C) The size of the density matrix as a function of the number of spins, N, for the full-space (k = N) and reduced-space (k = 4) cases.

approach has previously been shown to be very effective for the numerical simulation of ^{1}H spin diffusion in systems of more than 100 spins undergoing magic-angle spinning (0.5 kHz $< \nu_{rot} <$ 50 kHz). [192, 193] The density matrix, σ, for a system of N spin-1/2 nuclei in Liouville space can be expanded as a linear combination of 2^{2^N} basis operators, B_n:

$$\sigma = \sum_{n=1}^{2^{2^N}} b_n(t) B_n \tag{6.8}$$

Each member B_n of the basis set can be described as the product of N single spin operators, where E is the identity.

$$B_n = 2^{p-1} \prod_{i=1}^{N} I_{i,n} \tag{6.9}$$

$$I_{i,n} \in \{E_n, I_{nz}, \frac{1}{\sqrt{2}} I_n^+, \frac{1}{\sqrt{2}} I_n^-\} \tag{6.10}$$

For each product operator, we define the spin order, p, as the number of constituent single-spin operators that are not the identity (E). For example, the single-spin polarization operator, $I_1 z$, has a spin-order of p = 1, while the product operator $I_{2z} I_3^+ I_5^-$ has a spin order of p = 3. In Figure 6.9 (A), we present a visualization of a density matrix in Liouville space (N = 7) where each dot is a single element, and the elements have been organized

into rings according to spin order. (Note, here we have limited ourselves to the zero-quantum subspace, which can be done in the case of spontaneous polarization transfer with no loss of generality.[193]) A simulation of spin diffusion should calculate the evolution of the single-spin polarizations (the central ring); however, as the number of spins, N, increases the size of the outer rings increases dramatically, driving the overall exponential increase in the size of the density matrix. This can be seen for the example of N = 20 spins in Figure 6.9 (B), where we break down the total number of density matrix elements into the different spin orders. It is clear that the size of the density matrix is concentrated at high spin orders. The central hypothesis of the LCL method states that in order to quantitatively simulate the dynamics of the single-spin polarizations it is not necessary to exactly simulate the full density matrix, but instead only requires the inclusion of spin orders: p $<$ k « N. This corresponds in Figure 1a to carrying out the density matrix simulation for only the central k rings (shown here in green for k = 4). Using this approximation, systems with N $>$ 100 can be simulated because, as shown in Figure 6.9 (C), the growth in the size of the density matrix in the reduced space (green, k = 4) is polynomial in N, in contrast to the full-space density matrix (blue, k = N), which grows exponentially. It has been shown previously that this approximation is valid when the system is subjected to a time-dependent interaction such as magic-angle spinning; however, the approximation breaks down and produces non-physical results in the absence of spinning.[191, 193, 194] The first step in our method for calculating macroscopic spin diffusion coefficients from atomic coordinates is to use LCL to simulate spin diffusion within a bulk crystal. To do this, we define a box of dimension d^3 and fill it with the spins of interest at coordinates according to the structure. The system is initialised with a unit of polarization on the spin at the centre of the box and then the system is allowed to evolve with time in the reduced space (k = 4) under the influence of the homonuclear dipolar coupling Hamiltonian. MAS and powder averaging are included in the simulation as described in Ref. [193]. The result of the LCL simulation is a polarization transfer curve for each spin, such as those presented for a system of N ^{1}H spins corresponding to the structure of ice in Figure 6.9.

The second step is to calculate the evolution of the polarization in the box, P(r,t), using the 3D diffusion equation for an isotropic diffusion coefficient, D. The solution of the diffusion equation for a point source is well known:

$$P(r,t) = \frac{1}{(4\pi Dt)^{3/2}} exp(\frac{|r - r_0|}{4Dt}) \tag{6.11}$$

This solution can be adapted for diffusion in a box of dimension, d^3, by

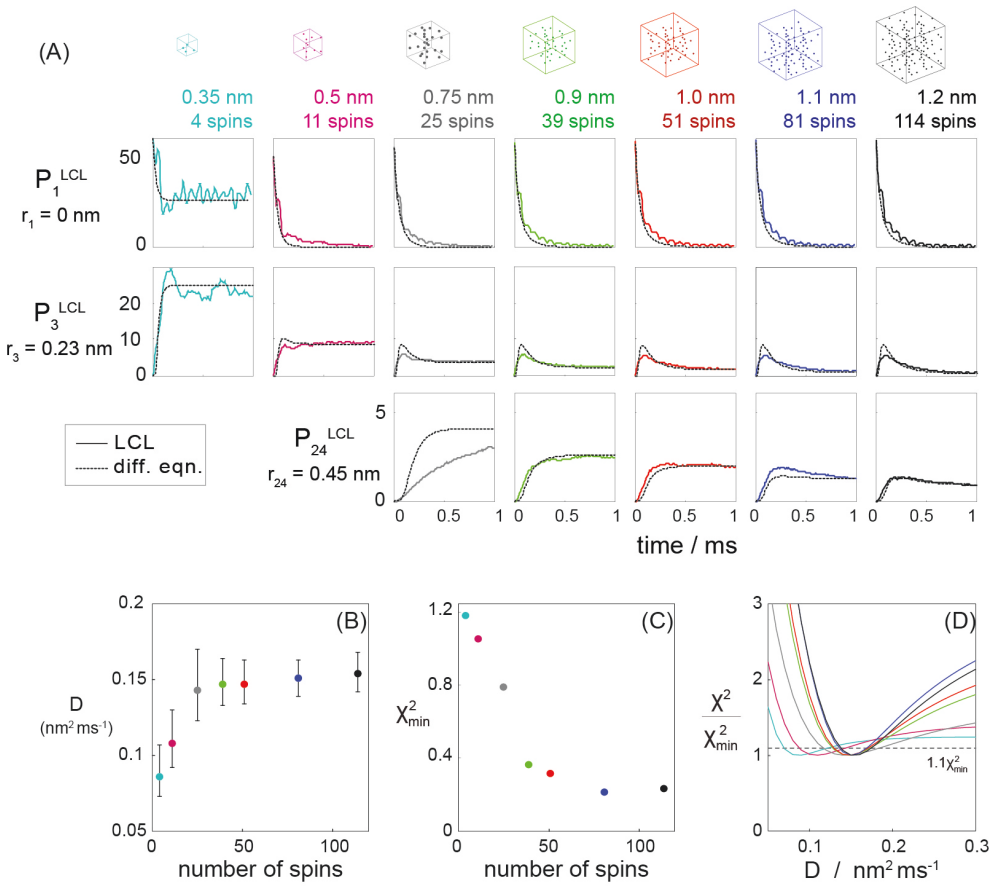

Figure 6.10: (A) Representative LCL spin-diffusion curves (solid lines) for a system of hexagonal ice in a box of dimension d which contains N ^{1}H nuclei (see plot labels). The dashed lines are the corresponding fits to the 3D diffusion equation. The curves shown correspond to the initially polarized ^{1}H spin located at the centre of the box (r = 0, top row), and non-initially polarized spins located at r = 2.3 nm (middle row) and r = 4.5 nm (bottom row) (B) Convergence of the diffusion coefficient, D, as the number of spins in the LCL simulation, N, increases from 4 to 114. Error bars correspond to χ^2/χ_{min}=1.1 (dashed line in (D).) (C) Reduction in χ^2 as a function of N. (D) Convergence of the fit between the LCL curves and the 3D diffusion equation for N = 4 (cyan), N = 11 (magenta), N = 25 (grey), N = 39 (green), N = 51 (red), N = 81 (blue) and N = 114 (black). The MAS rate was 12.5 kHz in all cases.

using the method of images. That is, we introduce a matrix of additional point sources of polarization outside the box, images of the source (and of one another) with respect to the boundaries of the box, such that the flux of polarization at each boundary remains zero throughout the duration of the simulation. The third step is to compare the LCL polarization transfer curves with the 3D diffusion equation result, and to determine the value of D that provides the minimum sum-of-squares difference, χ^2_{min}

This comparison is not straightforward because the 3D diffusion equation is continuous and so the conserved quantity is the integral of the polarization within the box. By contrast, the LCL simulation is discrete in the sense that polarization can only reside at points in the box occupied by a nuclear spin and so the conserved quantity is the sum of the polarization over all spin locations. Here we overcome this problem by evaluating the diffusion equation at each of the discrete spin positions and then renormalizing the result such that the total polarization remains fixed. The validity of this approach relies on two assumptions. First, we assume that the spins are relatively evenly distributed throughout the box so that no weighting is required during the renormalization step. Second, we assume that the average diffusion length $l = \sqrt{6Dt}$ is, at each step of the simulation, larger than the average distance between spins, r_{avg}. This latter point means that this renormalization step will only be valid for evolution times t > t_0, where $t_0 = r^2_{avg}/6D$. In all of the results presented herein a value of t_0 = 60 μs is used. This corresponds to a 3D diffusion length of 0.2 nm for a typical diffusion coefficient of 0.15 $nm^2.ms^{-1}$.

For our first example, we use the crystal structure for hexagonal ice and run a series of LCL simulations for box sizes ranging from d = 0.35 nm (cyan, N = 4) to d = 1.2 nm (black, N = 125) as shown in Figure 6.10 (A). Each simulation includes MAS with ν_r = 12.5 kHz and powder averaging. A series of representative LCL polarization transfer curves (solid lines) and corresponding diffusion equation fits (dashed lines) are presented in Fig 6.10. In this example, we find that both the χ^2 (Fig. 6.10 (C)) and the width of the minimum (Fig. 6.10 (D)) decrease as N increases, indicating an improved agreement between LCL and the diffusion model as more spins are included in the simulation. The value of D (Fig. 6.10 (B)) increases with N until a plateau value of approximately 0.15 $nm^2.ms^{-1}$ is reached for N > 25. The converged value of the diffusion coefficient for ice (ν_r = 12.5 kHz) and is in good agreement with the experimentally determined values for ^{1}H spin diffusion coefficients of polymers in the literature. Claus et al. found values of D = 0.8 $\pm$ 0.2 $nm^2.ms^{-1}$ for polymers at 4.5 kHz MAS over distances

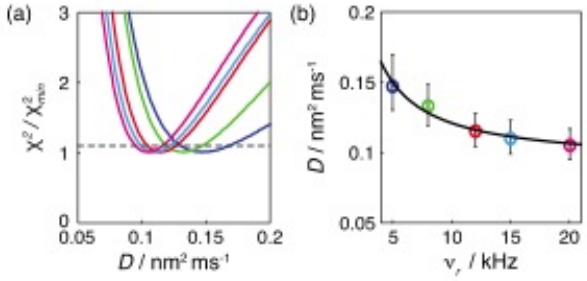

Figure 6.11: Convergence of the fit between the LCL curves and the 3D diffusion equation for a system of 84 ^{1}H spins of L-histidine.H2O.HCl (CSD entry histcm12) in a box with d = 1.2 nm for: ν_r=5 kHz (blue), ν_r= 8 kHz, ν_r = 12.5 kHz(red), ν_r= 15 kHz(cyan), and ν_r = 20 kHz (magenta). (b) Dependence of the diffusion coefficient on the on the MAS rate. The solid line is a fit of the diffusion coefficients to $D_r = a\nu_r^{-2} + b$.

of d = 1-100 nm.[195] Chen and Schmidt-Rohr have found that this value is smaller (D = 0.2 -0.5 nm^2.ms^{-1}) if measured over smaller distances (d = 0.5 - 1.0 nm).[146] A s a second example, we explore the effect of the MAS rate on the calculated spin diffusion coefficient using the crystal structure of L-histidine with d = 1.2 nm (N = 85). The results of a series of fits of ^{1}H LCL simulations to the 3D diffusion equation for spinning rates ranging from ν_r = 5 kHz (blue) to ν_r =20 kHz (magenta) are summarized in Fig. 6.11. If we compare the results for L-histidine to those for ice, we observe a decrease in D at 12.5 kHz MAS from D = 0.15 nm^2.ms^{-1} for ice to D = 0.11 nm^2.ms^{-1} for L-histidine. This result is consistent with the decrease in the density of ^{1}H spins in L-histidine when compared to ice. Second, we observe a decrease in the diffusion coefficient as the MAS rate increases. This decrease is due to the increased averaging of the dipolar coupling by the magic-angle spinning. As predicted by Average Hamiltonian theory the downward trend in spin-diffusion coefficient is here found to be proportional to ν_r^{-2} (black line in Figure 6.11).

In conclusion, we have introduced a method for quantitatively calculating spin diffusion coefficients directly from crystal structures and including both MAS and powder averaging effects. This approach uses the first-principles LCL method to simulate spin diffusion in a box, starting from a atomic geometry and including both MAS and powder averaging effects. These simulations were fit to the 3D diffusion equation to extract quantitative

^{1}H spin diffusion coefficients for ice and L-histidine, which are consistent with literature values for ^{1}H spin diffusion in polymers and follow the expected trends with respect to MAS rate and the density of ^{1}H spins.

Chapter 7

Conclusion

We have now come to the end of this work.[1]I hope the reader enjoyed the reading of the thesis, aimed at summarizing three years of developments and applications of DNP on materials carried out in the CRMN Lyon. I also hope they are now convinced of the potential of DNP for the study of surfaces. When I started this PhD the field was still a nascent area. Over these three years, we have witnessed a tremendous development with now several groups working on the application of DNP SENS (or similar techniques) to various complex materials including polymers, zeolites, cements, or alumina.

The nature of the polarizing agent dictates the enhancements accessible; and therefore the types of NMR experiments that can be done with reasonable sensitivity, together with the range of materials amenable to DNP SENS. The design of polarizing agents for CE DNP is therefore an important matter, and was illustrated here through a series of derivatives of the bTbK biradical. In particular, the importance of electron relaxation times has been highlighted. Both long T_1 and T_m have been shown to be beneficial to DNP, by increasing the saturation factor. Better saturation of the electron resonances could be linked with the DNP enhancement. In particular, the TEKPOL derivatives of bTbK were shown to yield unprecedented enhancement of over 200 at 9.4 T and 100 K. Efficient polarization with these radicals has also been reported at high temperature and at high spinning rate. Lots remain to be done in radical design, and in particular moving from nitroxide biradicals to narrow line radicals is expected to improve the CE, especially at higher fields.

Of course, in our case, the radical has to also yield high sensitivity en-

[1]Part of this work has been taken from published work I am an author on, in particular ref: [2, 110, 119, 101, 98, 138, 123, 185]

hancement when in the material. DNP SENS implies modifications of the sample with the introduction of both a solvent and radicals. Detrimental effects of the radicals on the NMR signal means that the optimal radical concentration for sensitivity is not necessarily the one yielding the highest enhancements. The type of surface and of radicals also affects their interactions. Bulky radicals have been shown to have different interaction with mesoporous silica, being partially excluded from the pores. These interaction could potentially be used to keep the radical away from the active center, thus enhancing the sensitivity, while still retaining high enhancements.

The high signal and sensitivity enhancement provided by the radicals introduced previously allowed us to apply DNP SENS to many functional materials, including MOFs, functionnalized mesoporous silica, and in particular to a surface Pd catalyst. Conformation determination of a Pt NHC complex grafted on a mesoporous silica is currently underway.

Finally, we turned our attention to polarization conductors, i.e materials with protons in their cores. The surface of impregnated organic micro crystals can be polarized using DNP, and polarization is propagated throughout the crystal by ^{1}H-^{1}H spin diffusion. A numerical model has been developed to explain the results obtained on glucose and sulfathiazole. Application to pharmaceutical compounds were given and we showed how to probe domain sizes of API and API/excipient interactions for instance. Finally, a last part focused on the prediction of spin diffusion constants from *ab initio* simulations. The model developed in the first part is currently being modified to be able to extract precise domain sizes from build-up curves.

Lots remain to be done in the field of DNP, both in the design of polarizing agents and in the development of methods for the study of materials. Developing narrow line biradicals that would retain high enhancements at higher magnetic fields is, for instance, one of the main challenges of DNP enhanced solid-state NMR, that will open the way to the investigation of increasingly complex modern materials, including materials with very low surface area. The hardware instrumentation for DNP is also rapidly developing, with lower temperature probes being developed for instance. More efficient MW sources, faster MAS probes for DNP are also under development, or pulsed EPR sources for pulsed DNP applications.

Bibliography

[1] Gabor A Somorjai, Heinz Frei, and Jeong Y Park. Advancing the frontiers in nanocatalysis, biointerfaces, and renewable energy conversion by innovations of surface techniques. *J. Am. Chem. Soc.*, 131(46):16589–16605, November 2009.

[2] Aaron J Rossini, Alexandre Zagdoun, Moreno Lelli, Anne Lesage, Christophe Copéret, and Lyndon Emsley. Dynamic Nuclear Polarization Surface Enhanced NMR Spectroscopy. *Acc. Chem. Res.*, 46(9):1942–1951, September 2013.

[3] Gary E Maciel and Dean W Sindorf. Silicon-29 NMR study of the surface of silica gel by cross polarization and magic-angle spinning. *J. Am. Chem. Soc.*, 102(25):7606–7607, December 1980.

[4] G E Maciel, D W SINDORF, and V J BARTUSKA. Characterization of Silica-Attached Systems by Si-29 and C-13 Cross-Polarization and Magic-Angle Spinning Nuclear Magnetic-Resonance. *Journal of Chromatography*, 205(2):438–443, 1981.

[5] L Bemi, H C Clark, J A Davies, C A Fyfe, and R E Wasylishen. Studies of phosphorus(III) ligands and their complexes of nickel(II), palladium(II), and platinum(II) immobilized on insoluble supports by high-resolution solid-state phosphorus-31 NMR using magic-angle spinning techniques. *J. Am. Chem. Soc.*, 104(2):438–445, January 1982.

[6] Mathieu Chabanas, Elsje Alessandra Quadrelli, Bernard Fenet, Christophe Copéret, Jean Thivolle-Cazat, Jean-Marie Basset, Anne Lesage, and Lyndon Emsley. Molecular Insight Into Surface Organometallic Chemistry Through the Combined Use of 2D HETCOR Solid-State NMR Spectroscopy and Silsesquioxane Analogues. *Angew. Chem. Int. Ed.*, 40(23):4493–4496, December 2001.

[7] Franck Rataboul, Anne Baudouin, Chloé Thieuleux, Laurent Veyre, Christophe Copéret, Jean Thivolle-Cazat, Jean-Marie Basset, Anne

Lesage, and Lyndon Emsley. Molecular understanding of the formation of surface zirconium hydrides upon thermal treatment under hydrogen of [([triple bond]SiO)Zr(CH2tBu)3] by using advanced solid-state NMR techniques. *J. Am. Chem. Soc.*, 126(39):12541–12550, October 2004.

[8] Frédéric Blanc, Christophe Copéret, Jean Thivolle-Cazat, Jean-Marie Basset, Anne Lesage, Lyndon Emsley, Amritanshu Sinha, and Richard R Schrock. Surface versus molecular siloxy ligands in well-defined olefin metathesis catalysts: [(RO)3SiOMo(=NAr)(=CHtBu)(CH2tBu)]. *Angew. Chem. Int. Ed. Engl.*, 45(8):1216–1220, February 2006.

[9] P Avenier, M Taoufik, A Lesage, X Solans-Monfort, A Baudouin, A de Mallmann, L Veyre, J-M Basset, O Eisenstein, L Emsley, and E A Quadrelli. Dinitrogen dissociation on an isolated surface tantalum atom. *Science*, 317(5841):1056–1060, August 2007.

[10] Frédéric Blanc, Jean-Marie Basset, Christophe Copéret, Amritanshu Sinha, Zachary J Tonzetich, Richard R Schrock, Xavier Solans-Monfort, Eric Clot, Odile Eisenstein, Anne Lesage, and Lyndon Emsley. Dynamics of silica-supported catalysts determined by combining solid-state NMR spectroscopy and DFT calculations. *J. Am. Chem. Soc.*, 130(18):5886–5900, May 2008.

[11] Frédéric Blanc, Christophe Copéret, Anne Lesage, and Lyndon Emsley. High resolution solid state NMR spectroscopy in surface organometallic chemistry: access to molecular understanding of active sites of well-defined heterogeneous catalysts. *Chem. Soc. Rev.*, 37(3):518, 2008.

[12] Anne Lesage. Recent advances in solid-state NMR spectroscopy of spin I=1/2 nuclei. *Phys. Chem. Chem. Phys.*, 11(32):6876–6891, August 2009.

[13] Sharon E Ashbrook. Recent advances in solid-state NMR spectroscopy of quadrupolar nuclei. *Phys. Chem. Chem. Phys.*, 11(32):6892–6905, August 2009.

[14] Jerzy W Wiench, Charles E Bronnimann, Victor S Y Lin, and Marek Pruski. Chemical shift correlation NMR spectroscopy with indirect detection in fast rotating solids: studies of organically functionalized mesoporous silicas. *J. Am. Chem. Soc.*, 129(40):12076–12077, October 2007.

[15] T R Carver and C P Slichter. Polarization of Nuclear Spins in Metals. *Phys. Rev.*, 92(1):212–213, 1953.

[16] Charles P Slichter. The discovery and demonstration of dynamic nuclear polarization—a personal and historical account. *Phys. Chem. Chem. Phys.*, 12(22):5741, 2010.

[17] Albert Overhauser. Polarization of Nuclei in Metals. *Phys. Rev.*, 92(2):411–415, October 1953.

[18] TR Carver. Experimental verification of the Overhauser nuclear polarization effect. *Phys. Rev.*, 102:975–981, 1956.

[19] I Solomon and N Bloembergen. Nuclear Magnetic Interactions in the HF Molecule. *J. Chem. Phys.*, 25(2):261, 1956.

[20] Abragam A. Une nouvelle methode de polarisation dynamique des noyaux atomiques dans les solides. *C. R. Hebd. Seances Acad. Sci.*, 246:2253–22566, 1958.

[21] E Erb, J L Motchane, and J Uebersfeld. Sur une nouvelle methode de polarisation nucleaire dans les fluides adsorbes sur les charbons- extension aux solides et en particulier aux substances organiques irradiees. *C. R. Hebd. Seances Acad. Sci.*, 246:2253–22566, 1958.

[22] A V Kessenikh, V I Lushchikov, A A Manenkov, and I V Tara. *Sov. Phys. Solid State.*, 321, 1963.

[23] A V Kessenikh, A A Manenkov, and Pyatnitskii G I. *Sov. Phys. Solid State.*, 641, 1964.

[24] CF Hwang. New Effect in Dynamic Polarization. *Phys. Rev. Lett.*, 1967.

[25] CF Hwang. Phenomenological Model for the New Effect in Dynamic Polarization. *Phys. Rev. Lett.*, 1967.

[26] D G Crabb and W Meyer. Solid polarized targets for nuclear and particle physics experiments. *Annual Review of Nuclear and Particle Science*, 47(1):67–109, 1997.

[27] Marina Bennati, Claudio Luchinat, Giacomo Parigi, and Maria-Teresa Türke. Water 1H relaxation dispersion analysis on a nitroxide radical provides information on the maximal signal enhancement in Overhauser dynamic nuclear polarization experiments. *Phys. Chem. Chem. Phys.*, 12(22):5902, 2010.

[28] Brandon D Armstrong, Jennifer Choi, Carlos López, Darryl A Wesener, Wayne Hubbell, Silvia Cavagnero, and Songi Han. Site-specific hydration dynamics in the nonpolar core of a molten globule by dynamic nuclear polarization of water. *J. Am. Chem. Soc.*, 133(15):5987–5995, April 2011.

[29] Vasyl Denysenkov, Mark J Prandolini, Marat Gafurov, Deniz Sezer, Burkhard Endeward, and Thomas F Prisner. Liquid state DNP using a 260 GHz high power gyrotron. *Phys. Chem. Chem. Phys.*, 12(22):5786, 2010.

[30] Kathleen G Valentine, Guinevere Mathies, Sabrina Bédard, Nathaniel V Nucci, Igor Dodevski, Matthew A Stetz, Thach V Can, Robert G Griffin, and A Joshua Wand. Reverse micelles as a platform for dynamic nuclear polarization in solution NMR of proteins. *J. Am. Chem. Soc.*, 136(7):2800–2807, February 2014.

[31] Qing Zhe Ni, Eugenio Daviso, Thach V Can, Evgeny Markhasin, Sudheer K Jawla, Timothy M Swager, Richard J Temkin, Judith Herzfeld, and Robert G Griffin. High frequency dynamic nuclear polarization. *Acc. Chem. Res.*, 46(9):1933–1941, September 2013.

[32] Jan H Ardenkjaer-Larsen, Björn Fridlund, Andreas Gram, Georg Hansson, Lennart Hansson, Mathilde H Lerche, Rolf Servin, Mikkel Thaning, and Klaes Golman. Increase in signal-to-noise ratio of $>$ 10,000 times in liquid-state NMR. *Proc. Natl. Acad. Sci. U.S.A.*, 100(18):10158–10163, September 2003.

[33] Thorsten Maly, Galia T Debelouchina, Vikram S Bajaj, Kan-Nian Hu, Chan-Gyu Joo, Melody L Mak Jurkauskas, Jagadishwar R Sirigiri, Patrick C A van der Wel, Judith Herzfeld, Richard J Temkin, and Robert G Griffin. Dynamic nuclear polarization at high magnetic fields. *J. Chem. Phys.*, 128(5):052211, 2008.

[34] Yonatan Hovav, Akiva Feintuch, and Shimon Vega. Theoretical aspects of dynamic nuclear polarization in the solid state - The solid effect. *Journal of Magnetic Resonance*, 207(2):176–189, December 2010.

[35] Yonatan Hovav, Akiva Feintuch, and Shimon Vega. Dynamic nuclear polarization assisted spin diffusion for the solid effect case. *J. Chem. Phys.*, 134(7):074509, 2011.

[36] Albert A Smith, Björn Corzilius, Alexander B Barnes, Thorsten Maly, and Robert G Griffin. Solid effect dynamic nuclear polarization and polarization pathways. *J. Chem. Phys.*, 136(1):015101, January 2012.

[37] Yonatan Hovav, Akiva Feintuch, and Shimon Vega. Theoretical aspects of dynamic nuclear polarization in the solid state - The cross effect. *J. Magn. Reson.*, 214(1):29–41, January 2012.

[38] Kent R Thurber and Robert Tycko. Theory for cross effect dynamic nuclear polarization under magic-angle spinning in solid state nuclear magnetic resonance: The importance of level crossings. *J. Chem. Phys.*, 137(8):084508, 2012.

[39] Frederic Mentink-Vigier, Ümit Akbey, Yonatan Hovav, Shimon Vega, Hartmut Oschkinat, and Akiva Feintuch. Fast passage dynamic nuclear polarization on rotating solids. *Journal of Magnetic Resonance*, 224(C):13–21, November 2012.

[40] Lloyd Lumata, Ashish K Jindal, Matthew E Merritt, Craig R Malloy, A Dean Sherry, and Zoltan Kovacs. DNP by Thermal Mixing under Optimized Conditions Yields >60000 fold Enhancement of 89Y NMR Signal. *J. Am. Chem. Soc.*, 133(22):8673–8680, June 2011.

[41] Kan-Nian Hu. Polarizing agents and mechanisms for high-field dynamic nuclear polarization of frozen dielectric solids. *Solid State Nucl Magn Reson*, 40(2):31–41, September 2011.

[42] Lloyd Lumata, Matthew E Merritt, and Zoltan Kovacs. Influence of deuteration in the glassing matrix on 13C dynamic nuclear polarization. *Phys. Chem. Chem. Phys.*, 15(19):7032, 2013.

[43] Thorsten Maly, Loren B Andreas, Albert A Smith, and Robert G Griffin. 2H-DNP-enhanced 2H–13C solid-state NMR correlation spectroscopy. *Phys. Chem. Chem. Phys.*, 12(22):5872, 2010.

[44] Vladimir K Michaelis, Björn Corzilius, Albert A Smith, and Robert G Griffin. Dynamic Nuclear Polarization of 17O: Direct Polarization. *J. Phys. Chem. B*, page 131122100626008, November 2013.

[45] Debamalya Banerjee, Daphna Shimon, Akiva Feintuch, Shimon Vega, and Daniella Goldfarb. Journal of Magnetic Resonance. *Journal of Magnetic Resonance*, 230(C):212–219, May 2013.

[46] Shamon A Walker, Devin T Edwards, Ting Ann Siaw, Brandon D Armstrong, and Songi Han. Temperature dependence of high field 13C dynamic nuclear polarization processes with trityl radicals below 35 Kelvin. *Phys. Chem. Chem. Phys.*, 15(36):15106, 2013.

[47] GJ Gerfen, LR Becerra, DA Hall, and RG Griffin. High frequency (140 GHz) dynamic nuclear polarization: Polarization transfer to a solute in frozen aqueous solution. *J. Chem. Phys.*, 102:9494–9496, 1995.

[48] P Michon and A Rassat. Conformational analysis of a nitroxide biradical using nmr and electron spin resonance. *Nouv. J. Chim.*, 9, 1985.

[49] Kan-Nian Hu, Hsiao-hua Yu, Timothy M Swager, and Robert G Griffin. Dynamic Nuclear Polarization with Biradicals. *J. Am. Chem. Soc.*, 126(35):10844–10845, September 2004.

[50] Changsik Song, Kan-Nian Hu, Chan-Gyu Joo, Timothy M Swager, and Robert G Griffin. TOTAPOL: A Biradical Polarizing Agent for Dynamic Nuclear Polarization Experiments in Aqueous Media. *J. Am. Chem. Soc.*, 128(35):11385–11390, September 2006.

[51] Kan-Nian Hu, Changsik Song, Hsiao-hua Yu, Timothy M Swager, and Robert G Griffin. High-frequency dynamic nuclear polarization using biradicals: A multifrequency EPR lineshape analysis. *J. Chem. Phys.*, 128(5):052302, 2008.

[52] Yoh Matsuki, Thorsten Maly, Olivier Ouari, Hakim Karoui, François Le Moigne, Egon Rizzato, Sevdalina Lyubenova, Judith Herzfeld, Thomas Prisner, Paul Tordo, and Robert G Griffin. Dynamic Nuclear Polarization with a Rigid Biradical. *Angew. Chem. Int. Ed.*, 48(27):4996–5000, June 2009.

[53] Eric L Dane, Björn Corzilius, Egon Rizzato, Pierre Stocker, Thorsten Maly, Albert A Smith, Robert G Griffin, Olivier Ouari, Paul Tordo, and Timothy M Swager. Rigid Orthogonal Bis-TEMPO Biradicals with Improved Solubility for Dynamic Nuclear Polarization. *J. Org. Chem.*, 77(4):1789–1797, February 2012.

[54] Matthew K Kiesewetter, Björn Corzilius, Albert A Smith, Robert G Griffin, and Timothy M Swager. Dynamic Nuclear Polarization with a Water-Soluble Rigid Biradical. *J. Am. Chem. Soc.*, 134(10):4537–4540, March 2012.

[55] Claire Sauvée, Melanie Rosay, Gilles Casano, Fabien Aussenac, Ralph T Weber, Olivier Ouari, and Paul Tordo. Highly Efficient, Water-Soluble Polarizing Agents for Dynamic Nuclear Polarization at High Frequency. *Angew. Chem. Int. Ed.*, 52(41):10858–10861, August 2013.

[56] Leah B Casabianca, Alexander I Shames, Alexander M Panich, Olga Shenderova, and Lucio Frydman. Factors Affecting DNP NMR in Polycrystalline Diamond Samples. *J. Phys. Chem. C*, 115(39):19041–19048, October 2011.

[57] Kent R Thurber, Wai-Ming Yau, and Robert Tycko. Low-temperature dynamic nuclear polarization at 9.4T with a 30mW microwave source. *Journal of Magnetic Resonance*, 204(2):303–313, June 2010.

[58] Björn Corzilius, Albert A Smith, Alexander B Barnes, Claudio Luchinat, Ivano Bertini, and Robert G Griffin. High-Field Dynamic Nuclear Polarization with High-Spin Transition Metal Ions. *J. Am. Chem. Soc.*, 133(15):5648–5651, April 2011.

[59] Claudio Luchinat, Giacomo Parigi, and Enrico Ravera. Can metal ion complexes be used as polarizing agents for solution DNP? A theoretical discussion. *J Biomol NMR*, 58(4):239–249, April 2014.

[60] Melanie Rosay, Leo Tometich, Shane Pawsey, Reto Bader, Robert Schauwecker, Monica Blank, Philipp M Borchard, Stephen R Cauffman, Kevin L Felch, Ralph T Weber, Richard J Temkin, Robert G Griffin, and Werner E Maas. Solid-state dynamic nuclear polarization at 263 GHz: spectrometer design and experimental results. *Phys. Chem. Chem. Phys.*, 12(22):5850, 2010.

[61] Maria ConcistrÈ, Ole G Johannessen, Elisa Carignani, Marco Geppi, and Malcolm H Levitt. Magic-Angle Spinning NMR of Cold Samples. *Acc. Chem. Res.*, 46(9):1914–1922, September 2013.

[62] LR Becerra, GJ Gerfen, RJ Temkin, DJ Singel, and RG Griffin. Dynamic nuclear polarization with a cyclotron resonance maser at 5 T. *Phys. Rev. Lett.*, 71(21):3561–3564, November 1993.

[63] Paul P Woskov, Vikram S Bajaj, Melissa K Hornstein, Richard J Temkin, and Robert G Griffin. Corrugated Waveguide and Directional Coupler for CW 250-GHz Gyrotron DNP Experiments. *IEEE Trans Microw Theory Tech*, 53(6 I):1863–1869, June 2005.

[64] Alexander B Barnes, Emilio A Nanni, Judith Herzfeld, Robert G Griffin, and Richard J Temkin. A 250GHz gyrotron with a 3GHz tuning bandwidth for dynamic nuclear polarization. *Journal of Magnetic Resonance*, 221(C):147–153, August 2012.

[65] Alexander B Barnes, Evgeny Markhasin, Eugenio Daviso, Vladimir K Michaelis, Emilio A Nanni, Sudheer K Jawla, Elijah L Mena, Ronald DeRocher, Ajay Thakkar, Paul P Woskov, Judith Herzfeld, Richard J Temkin, and Robert G Griffin. Dynamic nuclear polarization at 700MHz/460GHz. *Journal of Magnetic Resonance*, 224(C):1–7, November 2012.

[66] Galia T Debelouchina, Marvin J Bayro, Patrick C A van der Wel, Marc A Caporini, Alexander B Barnes, Melanie Rosay, Werner E Maas, and Robert G Griffin. Dynamic nuclear polarization-enhanced solid-state NMR spectroscopy of GNNQQNY nanocrystals and amyloid fibrils. *Phys. Chem. Chem. Phys.*, 12(22):5911, 2010.

[67] Vikram S Bajaj, Melody L Mak Jurkauskas, Marina Belenky, Judith Herzfeld, and Robert G Griffin. DNP enhanced frequency-selective TEDOR experiments in bacteriorhodopsin. *Journal of Magnetic Resonance*, 202(1):9–13, January 2010.

[68] Marvin J Bayro, Galia T Debelouchina, Matthew T Eddy, Neil R Birkett, Catherine E MacPhee, Melanie Rosay, Werner E Maas, Christopher M Dobson, and Robert G Griffin. Intermolecular Structure Determination of Amyloid Fibrils with Magic-Angle Spinning and Dynamic Nuclear Polarization NMR. *J. Am. Chem. Soc.*, 133(35):13967–13974, September 2011.

[69] Galia T Debelouchina, Marvin J Bayro, Anthony W Fitzpatrick, Vladimir Ladizhansky, Michael T Colvin, Marc A Caporini, Christopher P Jaroniec, Vikram S Bajaj, Melanie Rosay, Cait E MacPhee, Michele Vendruscolo, Werner E Maas, Christopher M Dobson, and Robert G Griffin. Higher Order Amyloid Fibril Structure by MAS NMR and DNP Spectroscopy. *J. Am. Chem. Soc.*, 135(51):19237–19247, December 2013.

[70] Melanie Rosay, Ana-Carolina Zeri, Nathan S Astrof, Stanley J Opella, Judith Herzfeld, and Robert G Griffin. Sensitivity-Enhanced NMR of Biological Solids: Dynamic Nuclear Polarization of Y21M fd Bacteriophage and Purple Membrane. *J. Am. Chem. Soc.*, 123(5):1010–1011, February 2001.

[71] Melanie Rosay, Jonathan C Lansing, Kristin C Haddad, William W Bachovchin, Judith Herzfeld, Richard J Temkin, and Robert G Griffin. High-Frequency Dynamic Nuclear Polarization in MAS Spectra of Membrane and Soluble Proteins. *J. Am. Chem. Soc.*, 125(45):13626–13627, November 2003.

[72] Melody L Mak Jurkauskas, Vikram S Bajaj, Melissa K Hornstein, Marina Belenky, Robert G Griffin, and Judith Herzfeld. Energy transformations early in the bacteriorhodopsin photocycle revealed by DNP-enhanced solid-state NMR. *Proc. Natl. Acad. Sci. U.S.A.*, 105(3):883–888, January 2008.

[73] Vikram S Bajaj, Melody L Mak Jurkauskas, Marina Belenky, Judith Herzfeld, and Robert G Griffin. Functional and shunt states of bacteriorhodopsin resolved by 250 GHz dynamic nuclear polarization-enhanced solid-state NMR. *Proc. Natl. Acad. Sci. U.S.A.*, 106(23):9244–9249, June 2009.

[74] Arne H Linden, Sascha Lange, W Trent Franks, Ümit Akbey, Edgar Specker, Barth-Jan van Rossum, and Hartmut Oschkinat. Neurotoxin II Bound to Acetylcholine Receptors in Native Membranes Studied by Dynamic Nuclear Polarization NMR. *J. Am. Chem. Soc.*, 133(48):19266–19269, December 2011.

[75] Tomas Jacso, W Trent Franks, Honor Rose, Uwe Fink, Jana Broecker, Sandro Keller, Hartmut Oschkinat, and Bernd Reif. Characterization of membrane proteins in isolated native cellular membranes by dynamic nuclear polarization solid-state NMR spectroscopy without purification and reconstitution. *Angew. Chem. Int. Ed.*, 51(2):432–435, January 2012.

[76] Ivan V Sergeyev, Loren A Day, Amir Goldbourt, and Ann E McDermott. Chemical Shifts for the Unusual DNA Structure in Pf1 Bacteriophage from Dynamic-Nuclear-Polarization-Enhanced Solid-State NMR Spectroscopy. *J. Am. Chem. Soc.*, 133(50):20208–20217, December 2011.

[77] Marie Renault, Shane Pawsey, Martine P Bos, Eline J Koers, Deepak Nand, Ria Tommassen-van Boxtel, Melanie Rosay, Jan Tommassen, Werner E Maas, and Marc Baldus. Solid-State NMR Spectroscopy on Cellular Preparations Enhanced by Dynamic Nuclear Polarization. *Angew. Chem. Int. Ed.*, 51:2998–3001, February 2012.

[78] Hiroki Takahashi, Isabel Ayala, Michel Bardet, Gaël De Paëpe, Jean-Pierre Simorre, and Sabine Hediger. Solid-State NMR on Bacterial Cells: Selective Cell Wall Signal Enhancement and Resolution Improvement using Dynamic Nuclear Polarization. *J. Am. Chem. Soc.*, 135(13):5105–5110, April 2013.

[79] Patrick C A van der Wel, Kan-Nian Hu, Józef Lewandowski, and Robert G Griffin. Dynamic Nuclear Polarization of Amyloidogenic Peptide Nanocrystals: GNNQQNY, a Core Segment of the Yeast Prion Protein Sup35p. *J. Am. Chem. Soc.*, 128(33):10840–10846, August 2006.

[80] Anne Lesage, Moreno Lelli, David Gajan, Marc A Caporini, Veronika Vitzthum, Pascal Miéville, Johan Alauzun, Arthur Roussey, Chloé Thieuleux, Ahmad Mehdi, Geoffrey Bodenhausen, Christophe Copéret, and Lyndon Emsley. Surface Enhanced NMR Spectroscopy by Dynamic Nuclear Polarization. *J. Am. Chem. Soc.*, 132(44):15459–15461, November 2010.

[81] Moreno Lelli, David Gajan, Anne Lesage, Marc A Caporini, Veronika Vitzthum, Pascal Miéville, Florent Héroguel, Fernando Rascón, Arthur Roussey, Chloé Thieuleux, Malika Boualleg, Laurent Veyre, Geoffrey Bodenhausen, Christophe Copéret, and Lyndon Emsley. Fast Characterization of Functionalized Silica Materials by Silicon-29 Surface-Enhanced NMR Spectroscopy Using Dynamic Nuclear Polarization. *J. Am. Chem. Soc.*, 133(7):2104–2107, February 2011.

[82] Manoja K Samantaray, Johan Alauzun, David Gajan, Santosh Kavitake, Ahmad Mehdi, Laurent Veyre, Moreno Lelli, Anne Lesage, Lyndon Emsley, Christophe Copéret, and Chloé Thieuleux. Evidence for Metal–Surface Interactions and Their Role in Stabilizing Well-Defined Immobilized Ru–NHC Alkene Metathesis Catalysts. *J. Am. Chem. Soc.*, 135(8):3193–3199, February 2013.

[83] Olivier Lafon, Melanie Rosay, Fabien Aussenac, Xingyu Lu, Julien Trébosc, Odile Cristini, Christophe Kinowski, Nadia Touati, Hervé Vezin, and Jean-Paul Amoureux. Beyond the Silica Surface by Direct Silicon-29 Dynamic Nuclear Polarization. *Angew. Chem. Int. Ed.*, 50(36):8367–8370, July 2011.

[84] Olivier Lafon, Aany S Lilly Thankamony, Takeshi Kobayashi, Diego Carnevale, Veronika Vitzthum, Igor I Slowing, Kapil Kandel, Hervé Vezin, Jean-Paul Amoureux, Geoffrey Bodenhausen, and Marek

Pruski. Mesoporous Silica Nanoparticles Loaded with Surfactant: Low Temperature Magic Angle Spinning 13C and 29Si NMR Enhanced by Dynamic Nuclear Polarization. *J. Phys. Chem. C*, 117(3):1375–1382, January 2013.

[85] Veronika Vitzthum, Françoise Borcard, Sami Jannin, Mylène Morin, Pascal Miéville, Marc A Caporini, Andrzej Sienkiewicz, Sandrine Gerber-Lemaire, and Geoffrey Bodenhausen. Fractional Spin-Labeling of Polymers for Enhancing NMR Sensitivity by Solvent-Free Dynamic Nuclear Polarization. *ChemPhysChem*, 12(16):2929–2932, October 2011.

[86] Frédéric Blanc, Samantha Y Chong, Tom O McDonald, Dave J Adams, Shane Pawsey, Marc A Caporini, and Andrew I Cooper. Dynamic Nuclear Polarization NMR Spectroscopy Allows High-Throughput Characterization of Microporous Organic Polymers. *J. Am. Chem. Soc.*, 135(41):15290–15293, October 2013.

[87] Hiroki Takahashi, Bastien Viverge, Daniel Lee, Patrice Rannou, and Gaël De Paëpe. Towards structure determination of self-assembled peptides using dynamic nuclear polarization enhanced solid-state NMR spectroscopy. *Angew. Chem. Int. Ed.*, 52(27):6979–6982, July 2013.

[88] Aaron J Rossini, Alexandre Zagdoun, Moreno Lelli, Jérôme Canivet, Sonia Aguado, Olivier Ouari, Paul Tordo, Melanie Rosay, Werner E Maas, Christophe Copéret, David Farrusseng, Lyndon Emsley, and Anne Lesage. Dynamic nuclear polarization enhanced solid-state NMR spectroscopy of functionalized metal-organic frameworks. *Angew. Chem. Int. Ed.*, 51(1):123–127, January 2012.

[89] Frédéric Blanc, Luke Sperrin, David A Jefferson, Shane Pawsey, Melanie Rosay, and Clare P Grey. Dynamic Nuclear Polarization Enhanced Natural Abundance 17O Spectroscopy. *J. Am. Chem. Soc.*, 135(8):2975–2978, February 2013.

[90] Veronika Vitzthum, Pascal Miéville, Diego Carnevale, Marc A Caporini, David Gajan, Christophe Copéret, Moreno Lelli, Alexandre Zagdoun, Aaron J Rossini, Anne Lesage, Lyndon Emsley, and Geoffrey Bodenhausen. Dynamic nuclear polarization of quadrupolar nuclei using cross polarization from protons: surface-enhanced aluminium-27 NMR. *Chem. Commun.*, 48(14):1988–1990, February 2012.

[91] Daniel Lee, Hiroki Takahashi, Aany S L Thankamony, Jean-Philippe Dacquin, Michel Bardet, Olivier Lafon, and Gaël De Paëpe. Enhanced Solid-State NMR Correlation Spectroscopy of Quadrupolar Nuclei Using Dynamic Nuclear Polarization. *J. Am. Chem. Soc.*, 134(45):18491–18494, November 2012.

[92] J L Berliner, S Eaton, and G Eaton. *Distance Measurements in Biological Systems by EPR*. Plenum Publisher New York.

[93] Y. Zhou, B.E. Bowler, G R Eaton, and S S Eaton. Electron Spin Lattice Relaxation Rates for S=1/2 Molecular Species in Glassy Matrices or Magnetically Dilute Solids at Temperatures between 10 and 300 K. *Journal of Magnetic Resonance*, 139(1):165–174, 1999.

[94] H Sato, V Kathirvelu, A Fielding, J P Blinco, A S Micallef, S E Bottle, S S Eaton, and G R Eaton. Impact of molecular size on electron spin relaxation rates of nitroxyl radicals in glassy solvents between 100 and 300 K. *Molecular Physics*, 105(15-16):2137–2151, August 2007.

[95] Hideo Sato, Steven E Bottle, James P Blinco, Aaron S Micallef, Gareth R Eaton, and Sandra S Eaton. Electron spin-lattice relaxation of nitroxyl radicals in temperature ranges that span glassy solutions to low-viscosity liquids. *Journal of Magnetic Resonance*, 191(1):66–77, March 2008.

[96] Andrzej Rajca, Velavan Kathirvelu, Sandip K Roy, Maren Pink, Suchada Rajca, Santanu Sarkar, Sandra S Eaton, and Gareth R Eaton. A spirocyclohexyl nitroxide amino acid spin label for pulsed EPR spectroscopy distance measurements. *Chemistry*, 16(19):5778–5782, May 2010.

[97] V Kathirvelu, C. Smith, C. Parks, M.A. Mannan, Y. Miura, K. Takeshita, S S Eaton, and G R Eaton. Relaxation rates for spirocyclohexyl nitroxyl radicals are suitable for interspin distance measurements at temperatures up to about 125 K. *Chem. Commun.*, (4):454–456, 2009.

[98] Alexandre Zagdoun, Gilles Casano, Olivier Ouari, Martin Schwarzwälder, Aaron J Rossini, Fabien Aussenac, Maxim Yulikov, Gunnar Jeschke, Christophe Copéret, Anne Lesage, Paul Tordo, and Lyndon Emsley. Large Molecular Weight Nitroxide Biradicals Providing Efficient Dynamic Nuclear Polarization at Temperatures up to 200 K. *J. Am. Chem. Soc.*, 135(34):12790–12797, August 2013.

[99] Melanie Rosay. . *PhD thesis*, Massachuchetts Institute of Technology, August 2001.

[100] Enrico Ravera, Björn Corzilius, Vladimir K Michaelis, Camilla Rosa, Robert G Griffin, Claudio Luchinat, and Ivano Bertini. Dynamic Nuclear Polarization of Sedimented Solutes. *J. Am. Chem. Soc.*, 135(5):1641–1644, February 2013.

[101] Alexandre Zagdoun, Gilles Casano, Olivier Ouari, Giuseppe Lapadula, Aaron J Rossini, Moreno Lelli, Mathieu Baffert, David Gajan, Laurent Veyre, Werner E Maas, Melanie Rosay, Ralph T Weber, Chloé Thieuleux, Christophe Copéret, Anne Lesage, Paul Tordo, and Lyndon Emsley. A Slowly Relaxing Rigid Biradical for Efficient Dynamic Nuclear Polarization Surface-Enhanced NMR Spectroscopy: Expeditious Characterization of Functional Group Manipulation in Hybrid Materials. *J. Am. Chem. Soc.*, 134(4):2284–2291, February 2012.

[102] Hideo Sato, Velavan Kathirvelu, Gaëlle Spagnol, Suchada Rajca, Andrzej Rajca, Sandra S Eaton, and Gareth R Eaton. Impact of electron-electron spin interaction on electron spin relaxation of nitroxide diradicals and tetraradical in glassy solvents between 10 and 300 k. *J. Phys. Chem. B*, 112(10):2818–2828, March 2008.

[103] Vladimir K Michaelis, Albert A Smith, Björn Corzilius, Olesya Haze, Timothy M Swager, and Robert G Griffin. High-Field 13C Dynamic Nuclear Polarization with a Radical Mixture. *J. Am. Chem. Soc.*, 135(8):2935–2938, February 2013.

[104] Ümit Akbey, Arne H Linden, and Hartmut Oschkinat. High-Temperature Dynamic Nuclear Polarization Enhanced Magic-Angle-Spinning NMR. *Appl Magn Reson*, 43(1-2):81–90, May 2012.

[105] Kent R Thurber and Robert Tycko. Measurement of sample temperatures under magic-angle spinning from the chemical shift and spin-lattice relaxation rate of 79Br in KBr powder. *Journal of Magnetic Resonance*, 196(1):84–87, January 2009.

[106] Jiafei Mao, Dmitry Akhmetzyanov, Olivier Ouari, Vasyl Denysenkov, Björn Corzilius, Jörn Plackmeyer, Paul Tordo, Thomas F Prisner, and Clemens Glaubitz. Host–Guest Complexes as Water-Soluble High-Performance DNP Polarizing Agents. *J. Am. Chem. Soc.*, 135(51):19275–19281, December 2013.

[107] David Gajan, Martin Schwarzwälder, Matthew P Conley, Wolfram R Grüning, Aaron J Rossini, Alexandre Zagdoun, Moreno Lelli, Maxim Yulikov, Gunnar Jeschke, Claire Sauvée, Olivier Ouari, Paul Tordo, Laurent Veyre, Anne Lesage, Chloé Thieuleux, Lyndon Emsley, and Christophe Copéret. Solid-Phase Polarization Matrixes for Dynamic Nuclear Polarization from Homogeneously Distributed Radicals in Mesostructured Hybrid Silica Materials. *J. Am. Chem. Soc.*, 135(41):15459–15466, October 2013.

[108] C. L. Jackson and G. B. McKenna. *J. Chem. Phys.*, 93, 1990.

[109] D. Aksnes and L. Kimtys, 2004.

[110] Alexandre Zagdoun, Aaron J Rossini, David Gajan, Adrien Bourdolle, Olivier Ouari, Melanie Rosay, Werner E Maas, Paul Tordo, Moreno Lelli, Lyndon Emsley, Anne Lesage, and Christophe Copéret. Non-aqueous solvents for DNP surface enhanced NMR spectroscopy. *Chem. Commun.*, 48(5):654–656, January 2012.

[111] Aaron J Rossini, Alexandre Zagdoun, Moreno Lelli, David Gajan, Fernando Rascón, Melanie Rosay, Werner E Maas, Christophe Copéret, Anne Lesage, and Lyndon Emsley. One hundred fold overall sensitivity enhancements for Silicon-29 NMR spectroscopy of surfaces by dynamic nuclear polarization with CPMG acquisition. *Chem. Sci.*, 3(1):108–115, 2012.

[112] Sascha Lange, Arne H Linden, Ümit Akbey, W Trent Franks, Nikolaus M Loening, Barth-Jan van Rossum, and Hartmut Oschkinat. The effect of biradical concentration on the performance of DNP-MAS-NMR. *Journal of Magnetic Resonance*, 216(C):209–212, March 2012.

[113] BjÃ rn Corzilius, Loren B Andreas, Albert A Smith, Qing Zhe Ni, and Robert G Griffin. Journal of Magnetic Resonance. *Journal of Magnetic Resonance*, 240(C):113–123, March 2014.

[114] Hiroki Takahashi, Carlos Fernández-de Alba, Daniel Lee, Vincent Maurel, Serge Gambarelli, Michel Bardet, Sabine Hediger, Anne-Laure Barra, and Gaël De Paëpe. Journal of Magnetic Resonance. *Journal of Magnetic Resonance*, 239(C):91–99, February 2014.

[115] Hiroki Takahashi, Daniel Lee, Lionel Dubois, Michel Bardet, Sabine Hediger, and Gaël De Paëpe. Rapid natural-abundance 2D 13C-13C correlation spectroscopy using dynamic nuclear polarization enhanced

solid-state NMR and matrix-free sample preparation. *Angew. Chem. Int. Ed.*, 51(47):11766–11769, November 2012.

[116] Tarun K Maishal, Johan Alauzun, Jean-Marie Basset, Christophe Copéret, Robert J P Corriu, Erwan Jeanneau, Ahmad Mehdi, Catherine Reyé, Laurent Veyre, and Chloé Thieuleux. A Tailored Organometallic-Inorganic Hybrid Mesostructured Material: A Route to a Well-Defined, Active, and Reusable Heterogeneous Iridium-NHC Catalyst for H/D Exchange. *Angew. Chem. Int. Ed.*, 47(45):8654–8656, October 2008.

[117] Arthur Roussey, David Gajan, Tarun K Maishal, Anhurada Mukerjee, Laurent Veyre, Anne Lesage, Lyndon Emsley, Christophe Copéret, and Chloé Thieuleux. A highly ordered mesostructured material containing regularly distributed phenols: preparation and characterization at a molecular level through ultra-fast magic angle spinning proton NMR spectroscopy. *Phys. Chem. Chem. Phys.*, 13(10):4230–4233, 2011.

[118] Abragam A. *Principle of Nuclear Magnetism*. Oxford Science Publications.

[119] Alexandre Zagdoun, Aaron J Rossini, Matthew P Conley, Wolfram R Grüning, Martin Schwarzwälder, Moreno Lelli, W Trent Franks, Hartmut Oschkinat, Christophe Copéret, Lyndon Emsley, and Anne Lesage. Improved Dynamic Nuclear Polarization Surface-Enhanced NMR Spectroscopy through Controlled Incorporation of Deuterated Functional Groups. *Angew. Chem. Int. Ed.*, 52(4):1222–1225, January 2013.

[120] P. S. Allen and S. Clough. Tunneling-Assisted Nuclear Spin-Lattice Relaxation. *Phys. Rev. Lett.*, 22(25):1351, 1969.

[121] Ümit Akbey, W Trent Franks, Arne Linden, Sascha Lange, Robert G Griffin, Barth-Jan van Rossum, and Hartmut Oschkinat. Dynamic Nuclear Polarization of Deuterated Proteins. *Angew. Chem. Int. Ed.*, 49(42):7803–7806, August 2010.

[122] Martin Wessig, Malte Drescher, and Sebastian Polarz. Probing Functional Group Specific Surface Interactions in Porous Solids Using ESR Spectroscopy as a Sensitive and Quantitative Tool. *J. Phys. Chem. C*, 117(6):2805–2816, February 2013.

[123] Aaron J Rossini, Alexandre Zagdoun, Franziska Hegner, Martin Schwarzwälder, David Gajan, Christophe Copéret, Anne Lesage, and

Lyndon Emsley. Dynamic Nuclear Polarization NMR Spectroscopy of Microcrystalline Solids. *J. Am. Chem. Soc.*, 134(40):16899–16908, October 2012.

[124] Wolfram R Grüning, Aaron J Rossini, Alexandre Zagdoun, David Gajan, Anne Lesage, Lyndon Emsley, and Christophe Copéret. Molecular-level characterization of the structure and the surface chemistry of periodic mesoporous organosilicates using DNP-surface enhanced NMR spectroscopy. *Phys. Chem. Chem. Phys.*, 2013.

[125] Omar M Yaghi, Michael O'Keeffe, Nathan W Ockwig, Hee K Chae, Mohamed Eddaoudi, and Jaheon Kim. Reticular synthesis and the design of new materials. *Nature*, 423(6941):705–714, June 2003.

[126] Gérard Férey. Hybrid porous solids: past, present, future. *Chem. Soc. Rev.*, 37(1):191–214, January 2008.

[127] Susumu Kitagawa, Ryo Kitaura, and Shin-ichiro Noro. Functional porous coordination polymers. *Angew. Chem. Int. Ed. Engl.*, 43(18):2334–2375, April 2004.

[128] Bernard F Hoskins and Richard Robson. Infinite polymeric frameworks consisting of three dimensionally linked rod-like segments. *J. Am. Chem. Soc.*, 111(15):5962–5964, 1989.

[129] David Farrusseng, Sonia Aguado, and Catherine Pinel. Metal-organic frameworks: opportunities for catalysis. *Angew. Chem. Int. Ed.*, 48(41):7502–7513, 2009.

[130] Christophe Volkringer, Mohamed Meddouri, Thierry Loiseau, Nathalie Guillou, Jérôme Marrot, Gérard Férey, Mohamed Haouas, Francis Taulelle, Nathalie Audebrand, and Michel Latroche. The Kagomé topology of the gallium and indium metal-organic framework types with a MIL-68 structure: synthesis, XRD, solid-state NMR characterizations, and hydrogen adsorption. *Inorg Chem*, 47(24):11892–11901, December 2008.

[131] Frédérique Pourpoint, Aany Sofia Lilly Thankamony, Christophe Volkringer, Thierry Loiseau, Julien Trébosc, Fabien Aussenac, Diego Carnevale, Geoffrey Bodenhausen, Hervé Vezin, Olivier Lafon, and Jean-Paul Amoureux. Probing 27Al–13C proximities in metal–organic frameworks using dynamic nuclear polarization enhanced NMR spectroscopy. *Chem. Commun.*, 50(8):933, 2013.

[132] Taewook Kang, Seogil Oh, Honggon Kim, and Jongheop Yi. Facile Synthesis of Mesoporous Silica Sublayer with Hierarchical Pore Structure on Ceramic Membrane Using Anionic Polyelectrolyte. *Langmuir*, 21(13):5859–5864, June 2005.

[133] Takehiko Sasaki, Chongmin Zhong, Mizuki Tada, and Yasuhiro Iwasawa. Immobilized metal ion-containing ionic liquids: preparation, structure and catalytic performance in Kharasch addition reaction. *Chem. Commun.*, (19):2506, 2005.

[134] Ralf Lungwitz, Thomas Linder, Jörg Sundermeyer, Igor Tkatchenko, and Stefan Spange. Synthesis of chemisorbed imidazolium and phosphonium cations by reaction of ionic liquid precursors with silica. *Chem. Commun.*, 46(32):5903, 2010.

[135] Olga C Vangeli, George E Romanos, Konstantinos G Beltsios, Demosthenes Fokas, Evangelos P Kouvelos, Konstantinos L Stefanopoulos, and Nick K Kanellopoulos. Grafting of Imidazolium Based Ionic Liquid on the Pore Surface of Nanoporous Materials—Study of Physicochemical and Thermodynamic Properties. *J. Phys. Chem. B*, 114(19):6480–6491, May 2010.

[136] Iyad Karamé, Malika Boualleg, Jean-Michel Camus, Tarun K Maishal, Johan Alauzun, Jean-Marie Basset, Christophe Copéret, Robert J P Corriu, Erwan Jeanneau, Ahmad Mehdi, Catherine Reyé, Laurent Veyre, and Chloé Thieuleux. Tailored Ru-NHC Heterogeneous Catalysts for Alkene Metathesis. *Chem. Eur. J.*, 15(44):11820–11823, November 2009.

[137] Jun Nakazawa and T Daniel P Stack. Controlled Loadings in a Mesoporous Material: Click-on Silica. *J. Am. Chem. Soc.*, 130(44):14360–14361, November 2008.

[138] Matthew P Conley, Ruben M Drost, Mathieu Baffert, David Gajan, Cornelis Elsevier, W Trent Franks, Hartmut Oschkinat, Laurent Veyre, Alexandre Zagdoun, Aaron Rossini, Moreno Lelli, Anne Lesage, Gilles Casano, Olivier Ouari, Paul Tordo, Lyndon Emsley, Christophe Copéret, and Chloé Thieuleux. A Well-Defined Pd Hybrid Material for the Z-Selective Semihydrogenation of Alkynes Characterized at the Molecular Level by DNP SENS. *Chem. Eur. J.*, 19(37):12234–12238, August 2013.

[139] V Ladizhansky and S Vega. A Method for Measuring Heteronuclear (1H - 13C) Distances in High Speed MAS NMR. *J. Am. Chem. Soc.*, 122(14):3465–3472, April 2000.

[140] Terry Gullion and Jacob Schaefer. Rotational-echo double-resonance NMR. 1989. *J. Magn. Reson.*, 213(2):413–417, December 2011.

[141] N Bloembergen. On the Interaction of Nuclear Spins in a Crystalline Lattice. *Physica*, 15(3-4):386–426, 1949.

[142] P G De Gennes. Sur la relaxation nucleaire dans les cristaux ioniques. *Journal of Physics and Chemistry of Solids*, 7(4):345–350, 1958.

[143] J I Kaplan. Modified Linear-Response Method for Obtaining the Spin-Diffusion Constant of a Rigid Dipole System. *Phys. Rev. B*, 2:4578–4579, December 1970.

[144] T T P Cheung. Spin diffusion in NMR in solids. *Phys. Rev. B*, 23:1404–1418, February 1981.

[145] Steven P Brown and Hans Wolfgang Spiess. Advanced Solid-State NMR Methods for the Elucidation of Structure and Dynamics of Molecular, Macromolecular, and Supramolecular Systems. *Chem. Rev.*, 101(12):4125–4156, December 2001.

[146] Q Chen and K Schmidt-Rohr. Measurement of the local 1H spin-diffusion coefficient in polymers. *Solid State Nucl Magn Reson*, 29(1–3):142–152, February 2006.

[147] David L Bryce, Myrlene Gee, and Roderick E Wasylishen. High-Field Chlorine NMR Spectroscopy of Solid Organic Hydrochloride Salts: A Sensitive Probe of Hydrogen Bonding Environment. *J Phys Chem A*, 105(45):10413–10421, November 2001.

[148] David L Bryce, Gregory D Sward, and Samyuktha Adiga. Solid-state 35/37Cl NMR spectroscopy of hydrochloride salts of amino acids implicated in chloride ion transport channel selectivity: opportunities at 900 MHz. *J. Am. Chem. Soc.*, 128(6):2121–2134, February 2006.

[149] Robin K Harris. NMR studies of organic polymorphs and solvates. *Analyst*, 131(3):351–373, March 2006.

[150] Torsten Schaller, Uta P Buchele, Frank-Gerrit Klarner, Dieter Blaser, Roland Boese, Steven P Brown, Hans Wolfgang Spiess, Felix Koziol,

Jorg Kussmann, and Christian Ochsenfeld. Structure of molecular tweezer complexes in the solid state: NMR experiments, X-ray investigations, and quantum chemical calculations. *J. Am. Chem. Soc.*, 129(5):1293–1303, February 2007.

[151] Hiyam Hamaed, Jenna M Pawlowski, Benjamin F T Cooper, Riqiang Fu, S Holger Eichhorn, and Robert W Schurko. Application of solid-state 35Cl NMR to the structural characterization of hydrochloride pharmaceuticals and their polymorphs. *J. Am. Chem. Soc.*, 130(33):11056–11065, August 2008.

[152] Frederick G Vogt, Jacalyn S Clawson, Mark Strohmeier, Andrew J Edwards, Tran N Pham, and Simon A Watson. Solid-State NMR Analysis of Organic Cocrystals and Complexes. *Crystal Growth & Design*, 9(2):921–937, February 2009.

[153] Daniel Lee, Jochem Struppe, Douglas W Elliott, Leonard J Mueller, and Jeremy J Titman. Sensitive absorptive refocused scalar correlation NMR spectroscopy in solids. *Phys. Chem. Chem. Phys.*, 11(18):3547–3553, May 2009.

[154] Amy L Webber, Benedicte Elena, John M Griffin, Jonathan R Yates, Tran N Pham, Francesco Mauri, Chris J Pickard, Ana M Gil, Robin Stein, Anne Lesage, Lyndon Emsley, and Steven P Brown. Complete (1)H resonance assignment of beta-maltose from (1)H-(1)H DQ-SQ CRAMPS and (1)H (DQ-DUMBO)-(13)C SQ refocused INEPT 2D solid-state NMR spectra and first principles GIPAW calculations. *Phys. Chem. Chem. Phys.*, 12(26):6970–6983, July 2010.

[155] Andrew J Ilott, Sebastian Palucha, Andrei S Batsanov, Mark R Wilson, and Paul Hodgkinson. Elucidation of structure and dynamics in solid octafluoronaphthalene from combined NMR, diffraction, and molecular dynamics studies. *J. Am. Chem. Soc.*, 132(14):5179–5185, April 2010.

[156] Amy L Webber, Stefano Masiero, Silvia Pieraccini, Jonathan C Burley, Andrew S Tatton, Dinu Iuga, Tran N Pham, Gian Piero Spada, and Steven P Brown. Identifying guanosine self assembly at natural isotopic abundance by high-resolution 1H and 13C solid-state NMR spectroscopy. *J. Am. Chem. Soc.*, 133(49):19777–19795, December 2011.

[157] Jochen Autschbach, Shaohui Zheng, and Robert W Schurko. Analysis of electric field gradient tensors at quadrupolar nuclei in common structural motifs. *Concepts Magn. Reson.*, 36A(2):84–126, March 2010.

[158] Andrew S Tatton, Tran N Pham, Frederick G Vogt, Dinu Iuga, Andrew J Edwards, and Steven P Brown. Probing intermolecular interactions and nitrogen protonation in pharmaceuticals by novel 15N-edited and 2D 14N-1H solid-state NMR. *CrystEngComm*, 14(8):2654, 2012.

[159] Luis Mafra, Sergio M Santos, Renee Siegel, Ines Alves, Filipe A Almeida Paz, Dmytro Dudenko, and Hans W Spiess. Packing interactions in hydrated and anhydrous forms of the antibiotic Ciprofloxacin: a solid-state NMR, X-ray diffraction, and computer simulation study. *J. Am. Chem. Soc.*, 134(1):71–74, January 2012.

[160] Alexandra Dos, Volkmar Schimming, Monique Chan Huot, and Hans-Heinrich Limbach. Acid-Induced Amino Side-Chain Interactions and Secondary Structure of Solid Poly- l-lysine Probed by 15N and 13C Solid State NMR and ab InitioModel Calculations. *J. Am. Chem. Soc.*, 131(22):7641–7653, June 2009.

[161] John M Griffin, Dave R Martin, and Steven P Brown. Distinguishing anhydrous and hydrous forms of an active pharmaceutical ingredient in a tablet formulation using solid-state NMR spectroscopy. *Angew. Chem. Int. Ed. Engl.*, 46(42):8036–8038, 2007.

[162] Frederick G Vogt. Evolution of solid-state NMR in pharmaceutical analysis. *Future Medicinal Chemistry*, 2(6):915–921, June 2010.

[163] Terence L Threlfall. Analysis of organic polymorphs. A review. *Analyst*, 120(10):2435, 1995.

[164] Robin K Harris. NMR crystallography: the use of chemical shifts. *Thematic section: NMR crystallography*, 6(10):1025–1037, October 2004.

[165] Joseph W Lubach and Eric J Munson. Solid-state NMR Spectroscopy. In *Polymorphism*, pages 81–93. Wiley-VCH Verlag GmbH & Co. KGaA, 2006.

[166] Robert T Berendt, Diana M Sperger, Eric J Munson, and Paul K Isbester. Solid-state NMR spectroscopy in pharmaceutical research and analysis. *TrAC Trends in Analytical Chemistry*, 25(10):977–984.

[167] D C Apperley, R A Fletton, R K Harris, R W Lancaster, S Tavener, and T L Threlfall. Sulfathiazole polymorphism studied by magic-angle spinning NMR. *J Pharm Sci*, 88(12):1275–1280, December 1999.

[168] S Ganapathy, A Naito, and C A McDowell. Paramagnetic doping as an aid in obtaining high-resolution carbon-13 NMR spectra of biomolecules in the solid state. *J. Am. Chem. Soc.*, 103(20):6011–6015, 1981.

[169] L B Alemany, D M Grant, R J Pugmire, T D Alger, and K W Zilm. Cross Polarization and Magic Angle Sample Spinning Nmr-Spectra of Model Organic-Compounds .1. Highly Protonated Molecules. *J. Am. Chem. Soc.*, 105(8):2133–2141, 1983.

[170] L B Alemany, D M Grant, R J Pugmire, T D Alger, and K W Zilm. Cross Polarization and Magic Angle Sample Spinning Nmr-Spectra of Model Organic-Compounds .1. Highly Protonated Molecules. *J. Am. Chem. Soc.*, 105(8):2133–2141, 1983.

[171] Daniel P Murray, James J Dechter, and Lowell D Kispert. Cross-polarization and magic angle sample spinning NMR of model organic compounds with extremely long 1H T1's. *J. Polym. Sci. B Polym. Lett. Ed.*, 22(10):519–522, October 1984.

[172] Benjamin N Nelson, Loren J Schieber, Dewey H Barich, Joseph W Lubach, Thomas J Offerdahl, David H Lewis, John P Heinrich, and Eric J Munson. Multiple-sample probe for solid-state NMR studies of pharmaceuticals. *Solid State Nucl Magn Reson*, 29(1–3):204–213, February 2006.

[173] A Lesage, C Auger, S Caldarelli, and L Emsley. Determination of through-bond carbon-carbon connectivities in solid-state NMR using the INADEQUATE experiment. *J. Am. Chem. Soc.*, 119(33):7867–7868, 1997.

[174] P J Saindon, N S Cauchon, P A Sutton, C J Chang, G E Peck, and S R Byrn. Solid-state nuclear magnetic resonance (NMR) spectra of pharmaceutical dosage forms. *Pharm Res*, 10(2):197–203, February 1993.

[175] Joseph W Lubach, Brian E Padden, Stephanie L Winslow, Jonathon S Salsbury, David B Masters, Elizabeth M Topp, and Eric J Munson. Solid-state NMR studies of pharmaceutical solids in polymer matrices. *Anal Bioanal Chem*, 378(6):1504–1510, March 2004.

[176] Robin K Harris, Paul Hodgkinson, Tomas Larsson, and Amsaveni Muruganantham. Quantification of bambuterol hydrochloride in a

formulated product using solid-state NMR. *J Pharm Biomed Anal*, 38(5):858–864, August 2005.

[177] Michael Tobyn, Jonathan Brown, Andrew B Dennis, Michael Fakes, Qi Gao, John Gamble, Yaroslav Z Khimyak, Gary McGeorge, Chhaya Patel, Wayne Sinclair, Peter Timmins, and Shawn Yin. Amorphous drug-PVP dispersions: application of theoretical, thermal and spectroscopic analytical techniques to the study of a molecule with intermolecular bonds in both the crystalline and pure amorphous state. *J Pharm Sci*, 98(9):3456–3468, September 2009.

[178] Kevin M N Burgess, Frederic A Perras, Aurore Lebrun, Elisabeth Messner-Henning, Ilia Korobkov, and David L Bryce. Sodium-23 solid-state nuclear magnetic resonance of commercial sodium naproxen and its solvates. *J Pharm Sci*, 101(8):2930–2940, August 2012.

[179] Makoto Umino, Kenjirou Higashi, Hyuma Masu, Waree Limwikrant, Keiji Yamamoto, and Kunikazu Moribe. Characterization of cromolyn sodium hydrates and its formulation by 23Na-multiquantum and magic-angle spinning nuclear magnetic resonance spectroscopy. *J Pharm Sci*, 102(8):2738–2747, August 2013.

[180] Robert M Wenslow. 19F solid-state NMR spectroscopic investigation of crystalline and amorphous forms of a selective muscarinic M3 receptor antagonist, in both bulk and pharmaceutical dosage form samples. *Drug Dev Ind Pharm*, 28(5):555–561, May 2002.

[181] Lee M Katrincic, Yan T Sun, Robert A Carlton, Ann M Diederich, Ronald L Mueller, and Frederick G Vogt. Characterization, selection, and development of an orally dosed drug polymorph from an enantiotropically related system. *Int J Pharm*, 366(1-2):1–13, January 2009.

[182] Yusuke Nishiyama, Michael H Frey, Sseziwa Mukasa, and Hiroaki Utsumi. (13)C Solid-state NMR chromatography by magic angle spinning (1)H T(1) relaxation ordered spectroscopy. *J. Magn. Reson.*, 202(2):135–139, February 2010.

[183] Frederick G Vogt and Glenn R Williams. Analysis of a nanocrystalline polymer dispersion of ebselen using solid-state NMR, Raman microscopy, and powder X-ray diffraction. *Pharm Res*, 29(7):1866–1881, July 2012.

[184] Frederick G Vogt and Mark Strohmeier. 2D Solid-State NMR Analysis of Inclusion in Drug–Cyclodextrin Complexes. *Mol. Pharmaceutics*, 9(11):3357–3374, November 2012.

[185] Aaron J Rossini, Cory M Widdifield, Alexandre Zagdoun, Moreno Lelli, Martin Schwarzwälder, Christophe Copéret, Anne Lesage, and Lyndon Emsley. Dynamic Nuclear Polarization Enhanced NMR Spectroscopy for Pharmaceutical Formulations. *J. Am. Chem. Soc.*, 136(6):2324–2334, February 2014.

[186] B Elena, G De Paëpe, and L Emsley. Direct spectral optimisation of proton-proton homonuclear dipolar decoupling in solid-state NMR. *Chemical Physics Letters*, 398(4-6):532–538, November 2004.

[187] P Hodgkinson and L Emsley. Numerical simulation of solid-state NMR experiments. *Progress in Nuclear Magnetic Resonance Spectroscopy*, 36(3):201–239.

[188] Mikhail Veshtort and Robert G Griffin. SPINEVOLUTION: A powerful tool for the simulation of solid and liquid state NMR experiments. *Journal of Magnetic Resonance*, 178(2):248–282, February 2006.

[189] Mads Bak, Jimmy T Rasmussen, and Niels Chr Nielsen. SIMPSON: A General Simulation Program for Solid-State NMR Spectroscopy. *Journal of Magnetic Resonance*, 147(2):296–330, December 2000.

[190] Shanmin Zhang, B H Meier, and R R Ernst. Polarization echoes in NMR. *Phys. Rev. Lett.*, 69(14):2149–2151, October 1992.

[191] Mark C Butler, Jean-Nicolas Dumez, and Lyndon Emsley. Dynamics of large nuclear-spin systems from low-order correlations in Liouville space. *Chemical Physics Letters*, 477(4–6):377–381.

[192] Jean-Nicolas Dumez, Mark C Butler, Elodie Salager, Bénédicte Elena-Herrmann, and Lyndon Emsley. Ab initio simulation of proton spin diffusion. *Phys. Chem. Chem. Phys.*, 12(32):9172, 2010.

[193] Jean-Nicolas Dumez, Mark C Butler, and Lyndon Emsley. Numerical simulation of free evolution in solid-state nuclear magnetic resonance using low-order correlations in Liouville space. *J. Chem. Phys.*, 133(22):–, 2010.

[194] Meghan E Halse, Jean-Nicolas Dumez, and Lyndon Emsley. Quasi-equilibria in reduced Liouville spaces. *J. Chem. Phys.*, 136(22):224511, June 2012.

[195] J Clauss, K Schmidt-Rohr, and H W Spiess. Determination of domain sizes in heterogeneous polymers by solid-state NMR. *Acta Polym.*, 44(1):1–17, February 1993.

Appendix I: Debye Temperature and phonon-induced relaxation

In order to understand a bit more what the Debye temperature represents, and where the Raman relaxation comes from, we will derive here the theoretical expression of relaxation induced by coupling of the nuclear spins with the thermal vibration of the lattice. This derivation is strongly inspired by that of Abragam[118] but I hope it will help the reader understand a bit more about this processes. In this Appendix, we will see how phonons can induce relaxation in a system by modulating the interspin distance, and therefore spin-spin interactions. In order to do so, we first need a little theoretical background about phonons and their behavior in a system.

Debye's Model: Lattice vibrations and phonons.

Let's consider a cubic lattice with one nucleus per unit cell containing N atoms, spaced by a distance a and therefore of length L=Na. The position of an atom i in the lattice can be described as:

$$\overrightarrow{r_i} = \overrightarrow{R}_i + \overrightarrow{u_i} \tag{7.1}$$

with $\overrightarrow{R}_i$ the equilibrium position of the atom and $\overrightarrow{u}$ the departure from equilibrium of each atom (and therefore u_x, u_y and u_z « R). To describe the motion of the system, one would need 3N equations of motion corresponding to the 3 degrees of freedom of each of the N atoms. With N $\sim 10^{26}$, the resolution of the coupled equations becomes impossible. To circumvent this difficulty, Peter Debye used in 1912 the notion of phonons to describe the atomic motions in a crystal. Phonons are a collective excitation of atoms in a condensed arrangement of atoms, i.e an elementary vibrational motion in which a lattice of atoms uniformly oscillates at a single frequency. Any displacement of a *single atom* $\overrightarrow{u_p}$ can be seen as a superposition of these elementary vibrations (inverse discrete Fourier transform) and therefore:

$$\overrightarrow{u} = \sum_{k} \sum_{p=1}^{3} q(\overrightarrow{k}) exp(i\overrightarrow{r}.\overrightarrow{k})\overrightarrow{e}(\overrightarrow{k}, p) \tag{7.2}$$

where $\overrightarrow{k}$ represents the N wave vectors of the system, and the index p represents the three direction of the wave polarization, describe by the $\overrightarrow{e}(\overrightarrow{k}, p)$ vectors. $q(\overrightarrow{k}, p)$ are the normal coordinates of the normal modes.

Since the edges of the cubic lattice cannot vibrates, the wavelength of the phonons are quantified and:

$$k = \frac{n\pi}{L} \tag{7.3}$$

With n a positive integer.
Debye makes the approximation that frequency is inversely proportional to the wavelength, i.e that the propagation of the wave is independent of the direction of propagation and of the polarization

$$\omega(\overrightarrow{k}, p) = c_s || \overrightarrow{k} || \tag{7.4}$$

with c_s the velocity of sound in the medium. Note that this approximation is only valid for low frequency phonons (acoustic vibrations) and not high-frequency phonons (optical vibrations) but is sufficient in our case.

Furthermore, the volume of an individual mode in the reciprocal space is given by:

$$V_k = \frac{\pi^3}{(L)^3} \tag{7.5}$$

Thus the number of modes g(k)dk comprised between k and k + dk is given by:

$$g(k)dk = \frac{3Vk^2}{2\pi^2}dk \tag{7.6}$$

i.e, in term of pulsation,

$$g(\omega)d\omega = \frac{3V\omega^2}{2\pi^2 c_s^3}d\omega \tag{7.7}$$

Since the medium is not infinite, only a certain number of modes can exist in the solid. For a solid with N atoms having 3 degrees of freedom, the total number of phonons is 3N. There is therefore a maximum pulsation at which atoms can oscillate, called the Debye pulsation ω_D, and given by:

$$3N = \int_0^{\omega_D} g(\omega)d\omega \tag{7.8}$$

$$3N = \frac{V\omega_D^3}{2\pi^2 c_s^3} \tag{7.9}$$

therefore

$$\omega_D = c_s(\frac{6\pi^2 N}{V})^{1/3} \tag{7.10}$$

We now introduce the Debye temperature θ_D given by:

$$\hbar\omega_D = k_B\theta_D \tag{7.11}$$

with k_B the Boltzmann constant. Using $\rho = N/V$ the density of atoms in the lattice we get:

$$\theta_D = \frac{\hbar c_s}{k_B}(6\pi^2\rho)^{1/3} \tag{7.12}$$

For a given solid, low, high and medium temperature are as compared to the debye temperature. The higher the debye temperature, the more rigid the system is. For instance diamond has a Debye temperature of 2220 K whereas it is 96 K for lead. One can now easily calculate thermodynamic constants of the crystal, such as the energy of the thermal capacity, which is not our concern here.

A more accurate description of phonons is obtained using quantum mechanic. In this approach, the oscillations of the atoms can be described using the phonon creation ($q^\dagger_{k,s}$) and annihilation ($q_{k,s}$) operators respectively:

$$\overrightarrow{u} = \sum_k \sum_{p=1}^{3} \overrightarrow{e}(\overrightarrow{k}, p)[q(\overrightarrow{k})exp(i\overrightarrow{r}.\overrightarrow{k}) + q(\overrightarrow{k})^\dagger exp(-i\overrightarrow{r}.\overrightarrow{k})] \tag{7.13}$$

The only non null matrix elements of q and $q^\dagger$ are the ones coupling adjacent phonons (quantified by the integer n and described by the ket |n>):

$$< n|q|n+1 >=< n+1|q^\dagger|n >= (\frac{\hbar}{2M})^{1/2}\omega^{1/2}e^{-i\omega t}(n+1)^{1/2} \tag{7.14}$$

with M the mass of the crystal. Finally since phonons are bosons, the density of phonon is given by a Bose-Einstein distribution and the number $n(\omega)$ of phonons of frequency ω is:

$$n(\omega) = \frac{1}{exp(\hbar\omega/k_BT) - 1} \tag{7.15}$$

Now that the basic theoretical background for the vibration of the lattice has been laid, we can see how the phonon-spin interaction can lead to longitudinal relaxation.

Spin-Lattice coupling, Direct and Raman processes

The Hamiltonian describing the n spin systems in the phonon bath is:

$$H_{tot} = H_0 + H_{ph} + H_{int} \tag{7.16}$$

where H_0 is the sum of the n single spin Hamiltonian in the absence of interaction, H_{ph} is the Hamiltonian that describes the phonons in the medium. In the approximation of an harmonic crystal field we get:

$$H_{ph} = \sum_{k} \sum_{p=1}^{3} \hbar\omega_{k,s}(q^{\dagger}_{k,s} q_{k,s} + 1/2)] \tag{7.17}$$

In our approach, the coupling between the lattice and the spins will be expressed as:

$$H_{int} = F \cdot A \tag{7.18}$$

where F and A are the lattice and spin operators respectively. F is an operator that is function of the relative positions of of neighboring atoms:

$$\overrightarrow{R_{ij}} = \overrightarrow{r_i} - \overrightarrow{r_j} \tag{7.19}$$

$$\overrightarrow{R_{ij}} = \overrightarrow{R_i} - \overrightarrow{R_j} + \overrightarrow{u_i} - \overrightarrow{u_j} \tag{7.20}$$

Long-wavelength acoustic phonons time modulate the interspin distance and induce spin transitions. Only phonons whose wave vector is parallel to the interspin vector $\overrightarrow{R_{ij}}$ will be considered here, since phonons transversely polarized will have a small impact on the interspin distance. Furthermore, since the displacements are small, we can replace the $\overrightarrow{u_i} - \overrightarrow{u_j}$ term by its first order expansion along the interspin axis (with $x_{||}$ the coordinate parallel to $\overrightarrow{R_{ij}}$) :

$$\overrightarrow{u_i} - \overrightarrow{u_j} = R_{ij} \frac{\partial u}{\partial x_{||}} \tag{7.21}$$

Since the displacements are small, we can therefore expend F as a function of the strain tensor defined by ε:

$$\varepsilon_{ij} = \frac{1}{2}(\frac{\partial u_i}{\partial x_j} + \frac{\partial u_j}{\partial x_i}) \tag{7.22}$$

$$F = F_0 + F_1\varepsilon + F_2\varepsilon^2 + F_3\varepsilon^3 + ... \tag{7.23}$$

With the approximations made that the transverse phonons do not participate to the relaxation, we get:

$$F = F_0 + F_1 \frac{\partial u}{\partial x_{||}} + F_2(\frac{\partial u}{\partial x_{||}})^2 + F_3(\frac{\partial u}{\partial x_{||}})^3 + ... \tag{7.24}$$

In our approach, $\frac{\partial u}{\partial x_{||}}$ corresponds to a sum of phonon creation and annihilation operators given by:

$$\frac{\partial u}{\partial x_{||}} = icos^2(\phi_{ij})k[q(\overrightarrow{k})exp(i\overrightarrow{r}.\overrightarrow{k}) + q(\overrightarrow{k})^{\dagger}exp(-i\overrightarrow{r}.\overrightarrow{k})] \tag{7.25}$$

the $\frac{\partial u}{\partial x_{||}}$ term will therefore correspond to a one phonon process; $(\frac{\partial u}{\partial x_{||}})^2$ to a two phonon process and so on... In the following, the intensity of the transitions is calculated according given by Fermi's golden rule:

$$P = \frac{2\pi}{\hbar}| < \Psi_f|H_c|\Psi_i > |^2\rho(E) \tag{7.26}$$

where $|\Psi_i >$ and $|\Psi_f >$ are the initial and final wave function describing the system, H_c is the coupling Hamiltonian and $\rho(E)$ is the density of states, summed over the states accessible to the system.

One Phonon Process: the Direct Process

With this process, the energy of the phonon emitted or absorbed corresponds to the energy difference between two spin states m and m', hence the name. Therefore we have:

$$< \Psi_f|H_c|\Psi_i >=< m, n|F_1\frac{\partial u}{\partial x_{||}}A|m', n+1 > \tag{7.27}$$

$$< \Psi_f|H_c|\Psi_i >= F_1 < m|A|m' >< n|\frac{\partial u}{\partial x_{||}}|n+1 > \tag{7.28}$$

averaged over the whole phonon spectrum, and using the results above we get:

$$| < n|\frac{\partial u}{\partial x_{||}}|n+1 > |^2 = \frac{(n(\omega+1)\hbar^3\omega}{2Mc^2} \tag{7.29}$$

Meaning that P_d the probability for a spin-flip induced by absorption or emission of a photon is :

$$P_d = 9N\pi F_1^2\frac{\omega_0^3\hbar}{Mc^2\omega_D^3}(n(\omega_0)+1)| < m|A|m' > |^2 \tag{7.30}$$

If we now use the number of phonon at ω_0 given by the Bose-Einstein distribution, in the approximation that $\hbar\omega_0 << kT$ we get:

$$P_d = \frac{1}{T_{1d}} = \frac{9\pi F_1^2\omega_0^2\hbar^4}{Mc^2k^3\theta_D^4}| < m|A|m' > |^2T \tag{7.31}$$

yielding a rate proportional to the temperature.

Two Phonons Process: the Raman Process

In this case we consider a process with absorption of one phonon and emission of another, whose frequencies ω and ω' differ by the Larmor frequency ω_0:

$$\omega - \omega' = \omega_0 \tag{7.32}$$

Here we neglect the two phonon emission and two phonon absorption which only concern a very small portion of the phonon spectrum.
The matrix element for the transition where there are n phonons like the one emitted and n' like the one absorbed is:

$$< n|(\frac{\partial u}{\partial x_{||}})^2|n' >= F_2 \frac{\hbar}{2Mc^2}\sqrt{n'(n+1)\omega\omega'} \tag{7.33}$$

We can now apply Fermi's golden rule to find and integrate over the phonon spectrum to find the probability P_r of spin transition induced by a two-phonon process. We make the assumption that since $\omega_0 << \omega, \omega'$, we can take $\omega = \omega'$:

$$P_r = \frac{81\pi}{2}(\frac{F_2\hbar}{Mc})^2| < m|A|m' > |^2 \int_0^{\Omega_D} \frac{e^{\hbar\omega/kT}}{(e^{\hbar\omega/kT}-1)^2}\frac{\omega^6}{\omega_D^6}d\omega \tag{7.34}$$

$$P_r = \frac{81\pi}{2}(\frac{F_2\hbar}{Mc})^2| < m|A|m' > |^2 \frac{\omega^7}{\omega_D^7}\int_0^{\theta_D/T} \frac{x^6 e^x}{(e^x-1)^2}dx \tag{7.35}$$